MINISTRY OF SCIENCE AND HIGHER EDUCATION OF THE RUSSIAN FEDERATION

Federal State Budgetary Educational Institution of Higher Education
«RUSSIAN STATE HYDROMETEOROLOGICAL UNIVERSITY»

Department of meteorology, climatology and atmosphere protection

GRADUATE QUALIFICATION WORK

(Bachelor's thesis)

On «Study of the atmospheric boundary layer regimes over land and water surfaces with online integrated meteorology-aerosols interactions Enviro-HIRLAM model»

Done by Mikhaylenko Nikita Olegovich

Scientific supervisor: PhD in Physics and Mathematics, Associate Professor
of MCAP departament
Dr. Mkhanna Aaed Ismail Nazir

Scientific consultant: PhD in Physics and Mathematics, Senior researcher,
University of Helsinki, Faculty of Science/ Physics, Finland,
Dr. Mahura Alexander Gregorievich

«Allow presentation»
Acting head of the Departament

Signature

PhD in Geography, Associate Professor
Dr. Abannikov Victor Nikolaevich

«31» мая 2021г.

Saint-Petersburg
2021

Content

Introduction

The planetary boundary layer of the atmosphere (PBL) is the lower layer of the Earth's gas envelope. Research and forecasting of the distribution of meteorological parameters in PBL take a very important role. This is necessary for the safe and efficient functioning of various industries, agricultural activities, transport, and much more. Such meteorological parameters as temperature, humidity, wind speed, and direction are fundamental and depend on many factors related to the pressure field, radiation balance, etc. One of these factors is aerosol pollution, the source of which can be both anthropogenic and non-anthropogenic (natural). Anthropogenic sources include transport, various industries, some types of power plants, and others. Natural sources include volcanic activity, forest fires, weathering of mineral rocks, and pollution by dust storms. The effect of aerosol pollution on the temperature - wind - humidity regime depends mainly on the degree of pollution and on the type of pollutant. At the moment, there are various studies of the influence of air pollution on PBL. For example, Zhang, together with colleagues, has investigated the two-way feedback effect between aerosol pollution and PBL structure on the explosive rise of $PM_{2.5}$ [1].

The Environment High Resolution Limited Area Model (Enviro-HIRLAM) allows to forecast and investigate values of the meteorological parameters in the PBL with the effects of aerosol and gas pollution. This allows for unique research and forecasting taking into account anthropogenic and natural emissions. The purpose of this work is to evaluate temperature – wind - humidity regimes of the PBL over land and water surfaces for selected geographical regions of North-West Russia and Nordic countries taking into account aerosols effects on meteorology with the employment of online-integrated Environment-High Resolution Limited Area Model (Enviro-HIRLAM).

1. Planetary Boundary Layer

In the PBL Earth's surface has a large affection on the wind field. Molecular viscosity influences this effect, but it is only significant within a few millimeters of the Earth's surface - there, due to strong vertical shears, it occupies the same place in the momentum equation as other variables. Despite the fact that above these few millimeters, the viscosity is not important in the PBL equations for the mean wind (although important for small-scale turbulent eddies), it has a rather serious indirect effect. The consequence is that the wind speed at the surface tends to zero. As a result, even a weak wind will cause high-speed shear near the surface, which leads to the development of turbulent eddies. The spatial and temporal changes in these turbulent movements occur on a much smaller scale than those that fall under the meteorological observation network. These shear-induced vortices, as well as convective vortices that result from surface heating, provide efficient transfer of momentum to the surface, and transfer of latent and perceptible heat, at a rate much greater than molecular processes. This turbulent transport creates a planetary layer depth that varies from 30 meters with very large static stability to 3 km if strong co nvection occurs. Viscosity is not the fundamental one in the dynamic structure of PBL; it is rather the formation of atmospheric flow turbulence. In the region above the PBL - free atmosphere, turbulence can be neglected except in some cases associated with atmospheric currents, convective clouds, and atmospheric fronts [2]. The areas where the Earth’s oceans influence the atmosphere and have direct contact with it, are called Marine Boundary Layer (MBL). In the MBL, there is a significant exchange of momentum, moisture, and heat between the ocean surface and the atmosphere. It mostly happens via turbulent transport. These turbulent fluxes are organized by the couplets of the roll-like downdrafts and updrafts, and couplets of the cellular downdrafts and updrafts – rolls and cells. Conditions for the cells forming in the MBL are usually light wind over the areas of the ocean with a negative air-sea difference of the temperature – i.e. where the air temperature above the ocean is lower than sea surface temperature.). This unstable stratification causes updrafts and downdrafts. Longitudinal rolls vortices are quasi-helical circulations. The most commonly mentioned condition of the rolls development is the thermodynamic instability in the environment in subject to sufficient wind shear. The rolls might develop into cellular convention in a case when the ratio of the buoyancy to shear (approximated by the ratio of the differences between air and sea temperature to the average wind speed) increases higher than a certain threshold value [3].

It is important to note that the atmosphere and the water surface have a significant impact on each other. The boundary conditions for the atmospheric flow in the MBL are formed by the surface waves. The structure of the MBL is influenced by the wave field characteristics. This influence is observed, for example, on the wind field and atmospheric stability. The so-called Wave Boundary Layer (WBL) – is an area where the atmospheric flow is directly influenced by the wave field [4].

1.1. Surface Layer

The Surface Layer (SL) of the atmosphere is the first several tens of meters above the Earth's surface. The majority of the meteorological data requests from the industrial and agricultural branches of the economy are usually associated with the SL – because it is the place of the majority of human activity products [5]. The research on processes that are taking place in SL is quite a popular topic nowadays. For example, Weiguo Wang studied SL CO_2 budget and advective contributions to measurements of the net ecosystem–atmosphere exchange of CO_2 [6].

The influence of the Earth's surface in SL contributes to the pronounced diurnal variation of the various meteorological parameters such as – air temperature, wind characteristics, and humidity. The gradients of the main meteorological parameters in this SL have different values in comparison with the free atmosphere. It is especially observed for vertical gradients - at the height of SL, they usually have much higher values. In the free atmosphere, vertical temperature gradients have the order 1°C / 100 m. At a height of 1 m, the usual values are 100 times. The same applies to the gradients of density, humidity, and wind. The reason for this is the heterogeneity of the underlying surface. The only exception is pressure. For the dynamics of the free atmosphere (especially for its thermodynamics), the fact that the vertical temperature gradient differs from zero (This corresponds to the neutral equilibrium) is very important. In the SL, it is not relevant. Inside it, we can identify the vertical gradients of the absolute and potential temperatures. Moreover, we can identify the concepts of isotherm and conditions of indifferent equilibrium. In the SL, the turbulent friction stress, vertical turbulent heat flux, and vertical turbulent water vapor flux are constant with height. Sometimes it is said that in the SL the vertical turbulent flows do not change with height. This is the main property of the SL. The range of applicability of the above-mentioned basic property of the SL is limited from below (especially for heat and moisture fluxes) by a level of the order of 1 mm, below which, along with turbulent flows, molecular ones must be taken into account [5].

1.2. Atmospheric Turbulence

The atmosphere is in continuous motion. The peculiarity of the atmospheric movement is that the movement of individual air particles is disordered. The mode of the motion in which the individual particles of a liquid or gas have chaotic trajectories of motion (in relation to the general motion) is called turbulent. The speed of movement and the direction of movement of particles in this mode sharply change their value over short periods of time. Turbulence has a very strong effect on the state of the atmosphere, where various physical processes are taking place. In addition, there is a laminar mode of motion. Particles of liquid or gas move parallel to each other in such motion. The trajectories of their motion are smooth, slightly changing curves in time. In turn, the nature of the movement of liquid or gas depends on the dimensionless Reynolds number (1) [7]:

$$Re = \rho c l / \eta \tag{1}$$

Where: ρ - density; c - motion speed; l - characteristic scale of movement; η - dynamic coefficient of molecular viscosity. At small values of R, the movement is considered as laminar. When the number reaches a certain critical value Re, the movement changes to a turbulent one [8]. The Reynolds number studies are still used in various scientific fields. For example, a study of the relationship between the critical Reynolds number and aperture for flow through single fractures, carried out by Quinn and colleagues [9]. At constant density and dynamic coefficient of the molecular viscosity, an increase in the speed of movement and its scale contribute to the transition of the laminar regime to the turbulent one. An increase in viscosity, on the contrary, leads to the preservation of the laminar mode of motion up to high-speed values. An estimate of the Reynolds number for motions in the atmosphere shows that most of these are turbulent. An exception is a motion in a very thin layer of air (a few millimeters of thickness) adjacent to the Earth's surface. Such a layer is called the viscosity layer. The development of turbulent exchange can be very different. As an illustrative example to describe this diversity, we can consider the propagation of smoke coming out of a chimney. At low wind speeds, especially during inversion stratification in the lower atmosphere, the smoke spreads in a thin trickle over long distances. At high wind speeds, the stream becomes tortuous. In turn, with strong thermal instability, the jet breaks up into separate parts. At high wind speeds, meteorological quantities are rapidly changing, and chaotic fluctuations are observed. Despite this, all air particles have an average transfer rate. Due to this, the instantaneous speed of movement of an air particle (2):

$$\mathrm{c}^* = \mathrm{c} + \mathrm{c}' \tag{2}$$

Where c - average movement speed; $\mathrm{c}' -$deviation of instantaneous speed from average. For those layers of the atmosphere where temperature, wind speed, and density change with height (i.e., in layers with vertical stratification), the Reynolds number is not the only characteristic of the turbulent state of the environment. In addition, there is a general theory of turbulence, which makes it possible to establish that the development of turbulence in the atmosphere can be judged by another dimensionless parameter - the Richardson number. For more on Richardson's number, see J.C.R. Hunt work [10].

The atmospheric air contains various particles - water vapor, carbon dioxide, and ozone, as well as various atmospheric impurities - the smallest solid and liquid particles. There is a term for specific impurity content "S". This is its mass of impurity per unit mass of air. For example, in the case of water vapor, "S" is the mass fraction of water vapor. The specific content of an impurity in the atmosphere varies both in time and in space. With height, it usually decreases. In the horizontal direction, changes are also taking place. For example, in a city the value of the "S", more than in a rural area. In the process of turbulent mixing, individual air particles move from one point to another, both vertically and horizontally. Air particles usually detach from the general airflow at one point in space, move a certain distance, and mix with the flow at another point in space. In real conditions, this process occurs continuously. Separated from the flow, the air particle begins to mix with the surrounding air. During movement, air particles carry atmospheric impurities, water vapor, as well as other physical properties of the air, such as heat content and momentum. Turbulent mixing leads to equalization of the impurity content. There is a term Turbulent Impurity Flux. It is a value that shows what mass of impurity or water vapor (in kilograms) passes through a volume of air equal to 1 m^2 in one second.

$$Q = -A(\Delta s/\Delta z) \tag{3}$$

Where A - aspect ratio; Δs - the difference in specific impurity between the levels; Δz - distance between levels [8].

1.3. Temperature-wind-humidity regime of boundary layer

1.3.1. Temperature regime

The PBL is characterized by a well-pronounced diurnal temperature variation, which is caused by a change in the heat flux to the Earth's surface and atmosphere during the day. At night, under the influence of longwave radiation, the Earth's surface cools. During the day, under the influence of solar shortwave radiation, it heats up. It should be noted that the absorption by the air of its own long-wave radiation at nighttime, and short-wave solar radiation during the daytime, do not greatly affect the air temperature. The main reason for the diurnal variation of the air temperature is a heat exchange between the Earth's surface and the atmospheric layers, including PBL. The minimum temperature of the land surface is usually observed during a short period before sunrise. As the sun rises, the temperature of the surface rises rapidly. The heat from the Earth's surface is transferred to the air. This mostly happens through turbulent and solar radiation processes. A small thin layer of air that adjoins the Earth’s surface absorbs some of the heat. The rest of the heat spreads to the overlying troposphere, where partial absorption occurs, and so on. Unlike the temperature of the Earth's surface, the air temperature after sunrise begins to increase with a slight delay, depending on the height at which a particular layer of air is located. The air temperature rises quite quickly during the morning hours. This happens until about 9-10 am hours (in summer, in middle latitudes). Further, the temperature rise begins to slow down. Its maximum, at 2 meters above the surface, is observed at 13-14 pm. Then, the temperature begins a slow decrease, which lasts until 16-17 pm (i.e. approximately before sunset). After that, the temperature begins to drop much faster. Since the main source of daily fluctuations is solar radiation absorbed by the Earth's surface, it is important that in winter the influx of solar radiation at around noon is much less than in summer. Because of this, the amplitude of the daily variation of air temperature near the Earth's surface in winter is almost two times less than in summer. In summer, the turbulent exchange is much more intense than in other seasons. Because of this, the decrease in amplitude with height in spring and summer is slower than in autumn and winter: At an altitude of 700 m in autumn and winter, an amplitude of the air temperature is 7 - 8 times less than near the ground, while in summer and spring - 5 times. However, the diurnal fluctuations are characteristic not only of the temperature but also of its vertical gradient. In summer, at an altitude of up to 200 m, it is negative at night, and in the daytime, it is positive, the amplitude of the diurnal variation decreases with height. In winter, the vertical gradient of temperature up to 200 meters changes its sign during a day, just as in summer, but the time interval when it is positive is much less. For some reason, such as the proximity of the inhomogeneous (in physical properties) terrestrial surface, large fluctuations (in space and time) of the various gases that absorb radiation, due to clouds, fogs, various solid examples, and other factors, a fairly wide variety of air temperature profiles is provided in the PBL. In this regard, there are studies of the daily temperature variation in different parts of Earth [8]. For example, Kenyon studied the diurnal variation of air temperature across the north pacific [11].

At the same time, there is a close interdependence and interaction between different fields of meteorological quantities in the atmosphere. For example, the temperature distribution has a major influence on the distribution of the characteristics of humidity and turbulent exchange. The temperature field, in turn, is strongly influenced by the water vapor - in particular, clouds, and fogs as condensation products. The turbulent exchange has a serious impact on the wind speed and temperature profiles, and at the same time, itself depends on them [8].

1.3.2. Wind regime

There is a pattern of atmospheric movements, the scale of which is comparable to the size of continents and oceans. The system of such movements is called the General Circulation of the Atmosphere (GCA) [5]. The GCA was described in detail by J.M. Wallace and his colleagues [12].

As we know, there is a temperature difference between the low and high latitudes, which is the cause of the pressure gradient along the meridian - from the equator to the poles. If it were not for the rotation of the Earth, the wind would blow along the baric gradient. However, the Coriolis force does its part; in the southern hemisphere, movement changes to the left, and in the north, to the right. In the equilibrium between the Coriolis force and the baric gradient, a westerly wind would be observed in both hemispheres. Thus, the atmosphere not only takes part in the rotational motion of the Earth, it also moves from the west to the east in relation to the Earth's surface. In the troposphere, the horizontal temperature gradient is on average directed from the low to high latitudes. The speed of the westerly wind increases with a height there, reaching a maximum near the tropopause. In the stratosphere, the horizontal temperature gradients in the warm season are directed from the high to low latitudes. In this regard, the thermal component of the wind is directed from east to west, and increases with height. Under the influence of this phenomenon, the speed of the westerly wind in the stratosphere decreases; at a certain height (15-27 km) it reaches a minimum. This level is called the windbreak. Above this level, the east wind prevails in the warm season. In winter, the horizontal temperature gradient is directed towards the pole. This is typical not only for the troposphere but also for the stratosphere. In this regard, in all three layers (Troposphere, Stratosphere, Mesosphere), the westerly wind persists and increases with height.

Large-scale vertical movements are formed primarily under the influence of turbulent and surface friction forces (horizontal scales - hundreds and thousands of kilometers). The vertical velocity is equal to zero at the Earth's surface. With increasing altitude, it increases and reaches a maximum in the middle troposphere (3 - 5 km). Then it decreases and becomes equal to zero near the tropopause. The change in the pressure gradient with height occurs due to the presence of horizontal temperature gradients. It is described by the so-called thermal wind. The influence of the thermal wind is very significant in a free atmosphere. Usually, it is just as significant in the main layer of the PBL

The wind speed vanishes on rough surfaces for simple reasons: Air molecules collide with irregularities and lose their forward speed. Making chaotic movements, these molecules collide with others, reducing their speed of translation, etc.

This is how the force of the molecular friction arises, which is the reason that the wind speed is zero at the minimum altitude. In the PBL, the direction of the wind speed deviates from the isobars towards low pressure. To prove this statement, we can consider the volume of air near the Earth's surface. The forces of the baric gradient and the deflecting force influence it. In addition, the friction forces from the higher and underlying air layers. The friction force «*R*» at the ground is directed almost opposite to the direction of the wind. The pressure gradient «*G2*» does not depend on the wind speed; it is directed along the normal to the isobars [8].

1.3.3. Humidity regime

The first few tens of meters above the Earth's surface are of great importance in the transfer of water vapor between the underlying surface, this domain and boundary layer, free troposphere, and other layers of the atmosphere. In SL, those flows of water vapor are formed, which ultimately lead to cloudiness. Humidity in SL changes very rapidly with height. Above SL, turbulent exchange and vertical flows also participate in the transport of water vapor. In general, the flow of water vapor in the PBL does not remain constant with a height. Obviously, the proportion of water vapor should not change under the influence of turbulent mixing, because it remains constant when the air particles move. When $s = s_2 = constant$ the water vapor pressure should drop with height in the same way as the atmospheric pressure:

$$\frac{e}{e_0} = \frac{p}{p_0} = exp\left(-\frac{gz}{R_C T_M}\right) \tag{4}$$

Where: e - partial pressure of water vapor at height z; e_0- partial pressure of water vapor at height z_0; p - atmospheric pressure at height z; p_0- atmospheric pressure at height z_0; R_C- gas constant; T_M- average temperature of the air layer between z and z_0; g - gravity acceleration. However, at low altitudes, the values of water vapor pressure calculated using this formula turns out to be greater than those values that correspond to the air temperature at these altitudes. This is explained by the fact that in most of the troposphere, the water vapor must condense. Accordingly, with height, the water vapor pressure decreases faster than the air pressure. On cloudy days, the relative humidity either does not change with altitude or falls rather slowly. The vertical profiles of atmospheric humidity characteristics are as varied as the temperature profiles. Changes in temperature and turbulent exchange in PBL are determined by a well-pronounced course of humidity characteristics [8].

The influence of air humidity on other meteorological quantities is a frequent topic of research nowadays. For example, Salamalikis and colleagues investigated atmospheric water vapor radiative effects on shortwave radiation under clear skies [13]. The greatest pronounced changes in the diurnal variation of humidity characteristics are noticeable during the warm half of the year over continents. In daily fluctuations in the mass fraction of water vapor, the pressure of water vapor, and specific humidity, two maxima are noted (i.e. during 7 - 10 am and 19 - 22 pm of local time) and two minima (i.e. before sunrise and during 15-17 pm). After sunrise, during morning hours, the air temperature of the Earth's surface begins to increase. The rate of evaporation increases. Then, the humidity of the air also increases. This growth continues until 9-10 am. At noon hours, the intensity of turbulent exchange increases greatly, and under its influence, the water vapor rises to the overlying layers of the atmosphere. In the event that the soil is not highly moistened, this outflow of water vapor through a turbulent exchange is not compensated. Accordingly, the air humidity drops significantly in the midday hours. In the evening hours, the turbulent exchange is weakened - and the air humidity begins to increase again. At night, the specific humidity decreases due to condensation of water vapor in the form of dew and fog. In winter, as well as above water and a highly humidified surface, the daily variation of air humidity looks different. In this case, at least one - at the end of the night. This is due to the fact that in winter, and above a highly moistened surface/water, the intensity of turbulent exchange does not increase so much at midday, compared to dry soil. In addition, the increase in this intensity is compensated by the increasing evaporation [8].

2. Methodology

2.1. Area of interest

The NWFD area (Figure 1) is characterized as a territory with the location of many different industrial complexes. For example, in the Arkhangelsk region, there are pulp-paper mills (PPM), public corporation «Northern Machine-Building Enterprise». In the Murmansk region, there are several industrial sites of «Kola mining and metallurgical company». In the Karelia region - the «Pitkyaranta» PPM. In the Leningrad region - the Kirishi State District Power Plant, «Kirishi» oil refinery and «Syassky» PPM. In the Pskov region – «NORDIX-BALT», the machine-building plant «SpiKo». In the Novgorod region - the «Uglovsky» lime plant, «Borovichi» refractories plant. In the Komi republic - the Syktyvkar PPM and industrial sites of «LUKOIL-Komi». In the Vologda region - Cherepovets factory «Severstal-metiz», Cherepovets nitrogen fertilizer plant. In the Nenetsky Autonomous Okrug - Oil company «Northern Lights», «RN Northern Oil». It is important to note, that these are not all industrial sites of the NWFD area where emissions of pollutants may occur. These are only the largest / known ones.

Figure 1. - Northwestern Federal District of Russia & surrounding territories.

2.2 Selection of episodes with elevated pollution

The industrial sites and factories are one of the main sources of anthropogenic aerosol and gaseous air pollution on the Earth. The values of the maximum allowable concentrations (MAC) in Russia for gases and aerosols are presented in Table 1. These numbers are given according to the Resolution of the Chief State Sanitary Doctor of the Russian Federation N165, dated by December 22, 2017 [14]. A significant excess of MAC is usually observed in cases of malfunctions or accidents occurring in the operation of an industrial complex. These lead to large-scale emissions of certain pollutants. Such cases may occur several times during the year. Pollution has both a direct (often negative) effect on human activity in the affected zone and an indirect effect on meteorological parameters. It is important to note that not only the emission area but also the surrounding areas are affected by emissions. It is due to the atmospheric transport of pollutants by the wind as well as their diffusion and deposition.

Table 1. - Maximum allowable concentration (MAC) of pollutants

№	Pollutants	Hazard class	MAC one-time, mg/m^3	MAC daily average, mg/m^3
1	Carbon monoxide	4	5	3
2	Nitrogen dioxide	3	0,2	0,04
3	Nitrogen oxide	3	0,4	0,06
4	Gasoline	4	5	1,5
5	Xylene	3	0,2	-
6	Sulfur dioxide	3	0,5	0,05
7	Ammonia	4	0,2	0,04
8	Hydrogen sulfide	2	0,008	-
9	Ozone	1	0,16	0,03
10	Formaldehyde	2	0,05	0,01
11	Phenol	2	0,01	0,006
12	Benzene	2	0,3	0,1
13	Toluene	3	0,6	-
14	Chlorine	2	0,1	0, 03
15	Styrene	2	0,04	0,002
16	Ethylbenzene	3	0,02	-

17	Naphthalene	4	0,007	-
18	Aerosol particles 10< μm	-	0,3	0,06
19	Aerosol particles 2,5< μm	-	0,16	0,035

In the process of searching for cases of the pollution of the boundary layer of the atmosphere in NWFD, the data (from issues of the scientific journal «Meteorology and Hydrology» from 2011 to 2019, as well as selected individual works, were analyzed (Table 1).

Table 2. - Summary of elevated air pollution episodes

Location	Month and Year	Pollutants
Kola peninsula, Murmansk region, Nikel city.	August 2013	Sulfur dioxide $SO_2$5 cases, up to 12 MAC (one time)
Kola peninsula, Murmansk region, Nikel city.	January 2019	Sulfur dioxide SO_2, 10 MAC (one time)
Kola peninsula, Murmansk region, Nikel city.	May 2019	Sulfur dioxide SO_2, 10 MAC (one time)
Arkhangelsk region, Arkhangelsk city	November 2015	Benzopyrene $C_{20}H_{12}$, 10 MAC (one time)
Arkhangelsk region, Novodvinsk city	September 2019	Benzopyrene $C_{20}H_{12}$, 53 MAC (one time)
Leningrad region, Saint-Petersburg	2020	$PM_{2.5}$ Up to 2.5 MAC, (one time) $C_{20}H_{12}$ Up to 20 MAC (daily average)
Karelian Republic.	1994	Sulfur compounds
Karelian Republic.	1995	Sulfur compounds
Arctic and subarctic regions of Russia	1995	Different pollutants

For the study, it was decided to select two time periods - August 2013 (Warm weather conditions) and January 2013 (Cold weather conditions). During August, in the city of Nickel (Murmansk region, Kola Peninsula), the 5 cases of exceeding the allowable concentration of the sulfur dioxide SO_2 were observed, up to 12 MAC (see Table 2). To analyze the effect of the pollution on the temperature-wind-humidity regime, the synoptic and meteorological conditions for both August and January were investigated (see Chapter 2.3).

Sulfur dioxide is one of the most common atmospheric pollutants on the Earth. It can be emitted into the atmosphere from both anthropogenic and natural sources. The main anthropogenic sources include various industrial enterprises, power plants. A significant natural source might be a volcanic eruption. The research on the pollution of the atmosphere with sulfur dioxide is actively carried out nowadays. For example, Nyashina et al. (2019) investigated the effects of the plant additives on the concentration of sulfur and nitrogen oxides in the combustion products of coal-water slurries containing petrochemicals [15]. The study of environmental pollution with sulfur dioxide in Poland was carried out, based on the concentration of sulfur on pine needles [16]. The sulfur dioxide contamination of the PBL has a detrimental effect on human health and quality of life. Kan et al. (2010) examined the short-term relationship between air pollution with sulfur dioxide and daily mortality in Asia, in particular, in China [17].

2.3. Meteorological situation

To analyze the synoptic situation in the Northwestern Federal District (NWFD) of Russia in August and January 2013, the surface synoptic maps based on the United Kingdom Met Office (UKMO) model were used. To analyze the air temperature and precipitation regimes for the same months, the surface air temperature (at 2m) maps based on the Climate Forecast System Reanalysis (CFSR) model output were used.

During the first decade of August, the nature of the weather in the NWFD area can be described as cyclonic, with some exceptions. In the first days of the decade, the area was influenced by cyclones (Figure 2a). However, by the middle of the decade, an anticyclone came from the east. It changed the nature of the weather to anticyclonic (Figure 2b). This continued until the end of the first decade (i.e. during the last days of it), the nature of the weather was characterized as cyclonic again. During the first half of the second decade of August, in the NWFD area, there was a pronounced cyclonic nature of the weather (Figure 2d). Only by the second half of the decade, an anticyclone began to approach from the southwest, and the weather in the south of the region relatively improved. During the third decade, anticyclonic weather prevailed in the NWFD (Figure 2c). The exception was the first two days of the decade. Also, in some days, the northern part of the region was under cyclonic impact from the north.

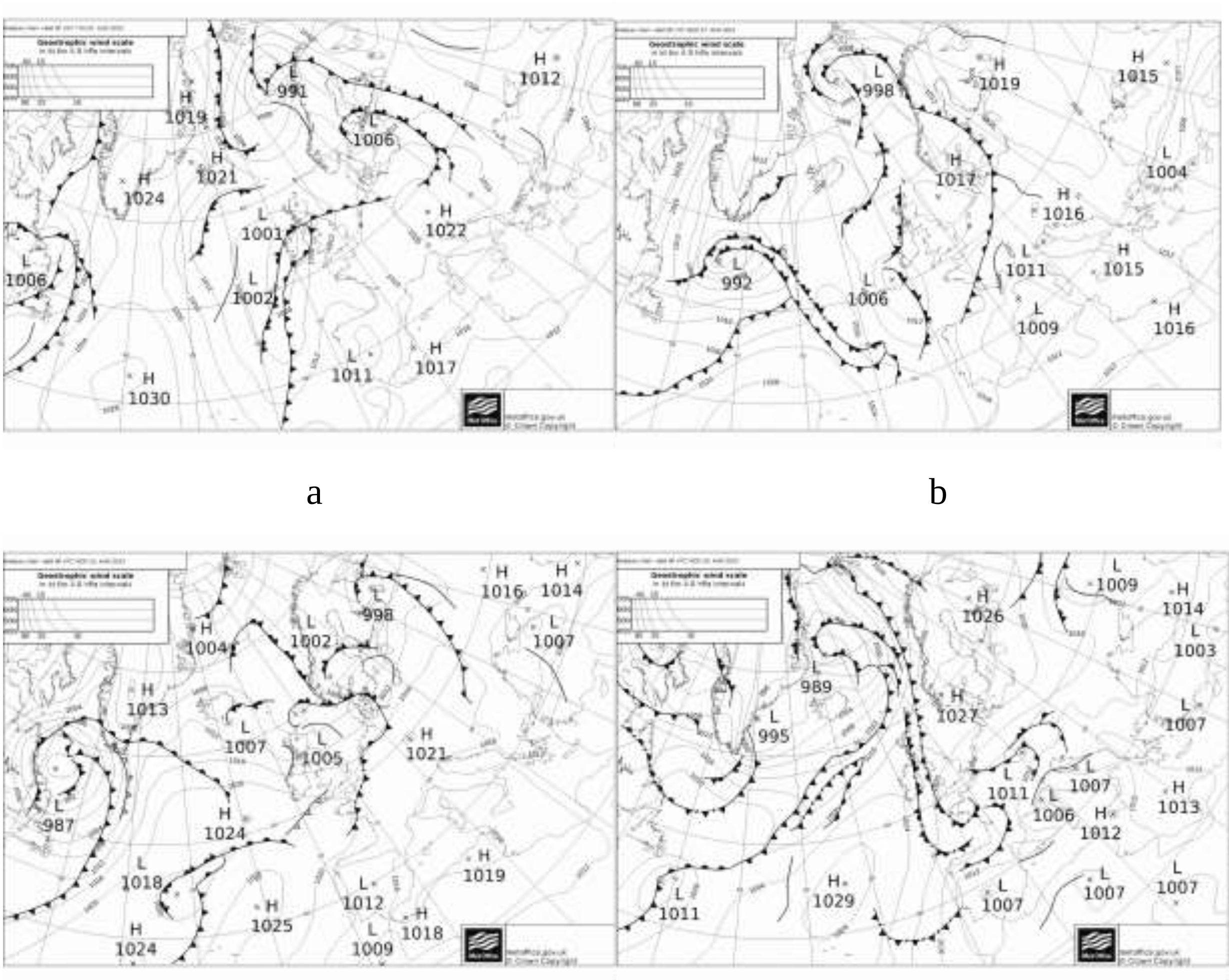

a b

c d

Figure 2. - Surface Analysis maps at 00 UTC for: (a) 01.08.2013, (b) 07.08.2013, (c) 12.08.2013, (d) 26.08.2013. [18]

During the first decade of August, the nighttime air temperature in the NWFD was from 18...21°C (in the southern part of the NWFD area) to 6...9 °C (in the northern part). Daytime temperatures during the first ten days of August ranged from 24...27 °C to 9…12 °C. The second decade of August was characterized by a cooling in the northern parts of the NWFD (Figure 3a). Nighttime temperatures ranged from 3...6°C (in the northern parts - 0...3°C) to 15...18°C. This was due to a pronounced cyclonic effect. Daytime temperatures ranged from 6...9 °C to 21...24 °C. During the third decade, the night temperature was from 3...6 °C to 15...18 °C. Daytime temperatures ranged from 6...9 °C to 18...21 °C. However, the temperature decreased below +10 °C very rarely. Mainly it was observed within small areas of the northern parts of the NWFD (Figure 3b).

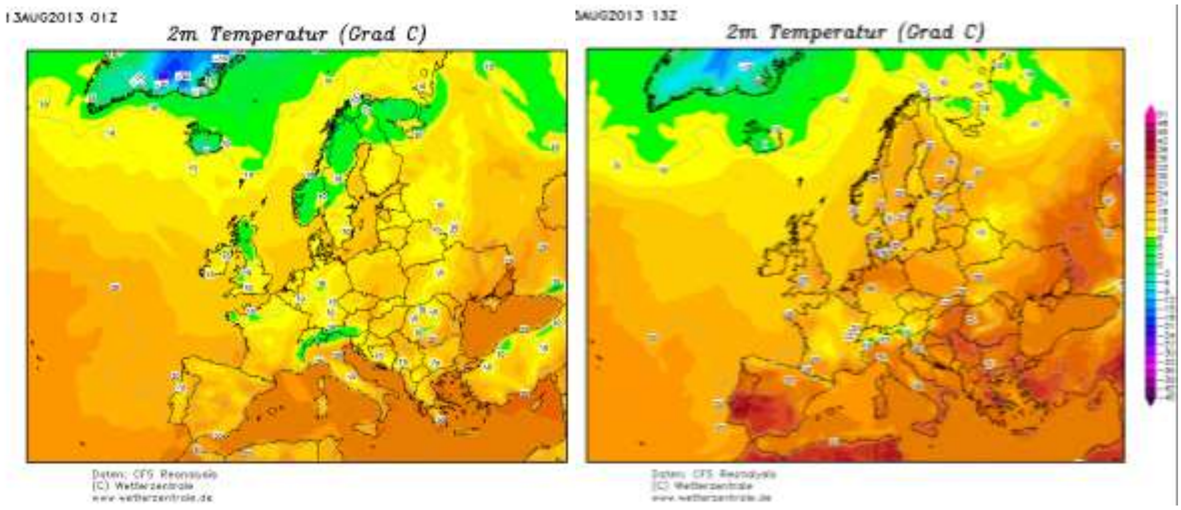

a b

Figure 3. - Air temperature (2m) for: (a) 13.08.2013 00 UTC, (b) 25.08.2013 12:00 UTC. [19]

During the first decade of August, in the NWFD, precipitation was observed mainly at the beginning (Figure 4a) and at the end of the decade (Figure 4b). This is due to the fact that in the middle of the decade it was characterized by the influence of an anticyclone. During the first half of the second decade, intensive precipitation was observed in most of the regions of the NWFD. It was mostly due to the strong cyclonic influence (Figure 4d). In the second half of the decade, precipitation was also observed in different parts of the NWFD, but it was more moderate in comparison with the first half of the decade. During the third decade, the amount of precipitation was very moderate. It was mainly observed in the northern parts of the NWFD (Figure 4c).

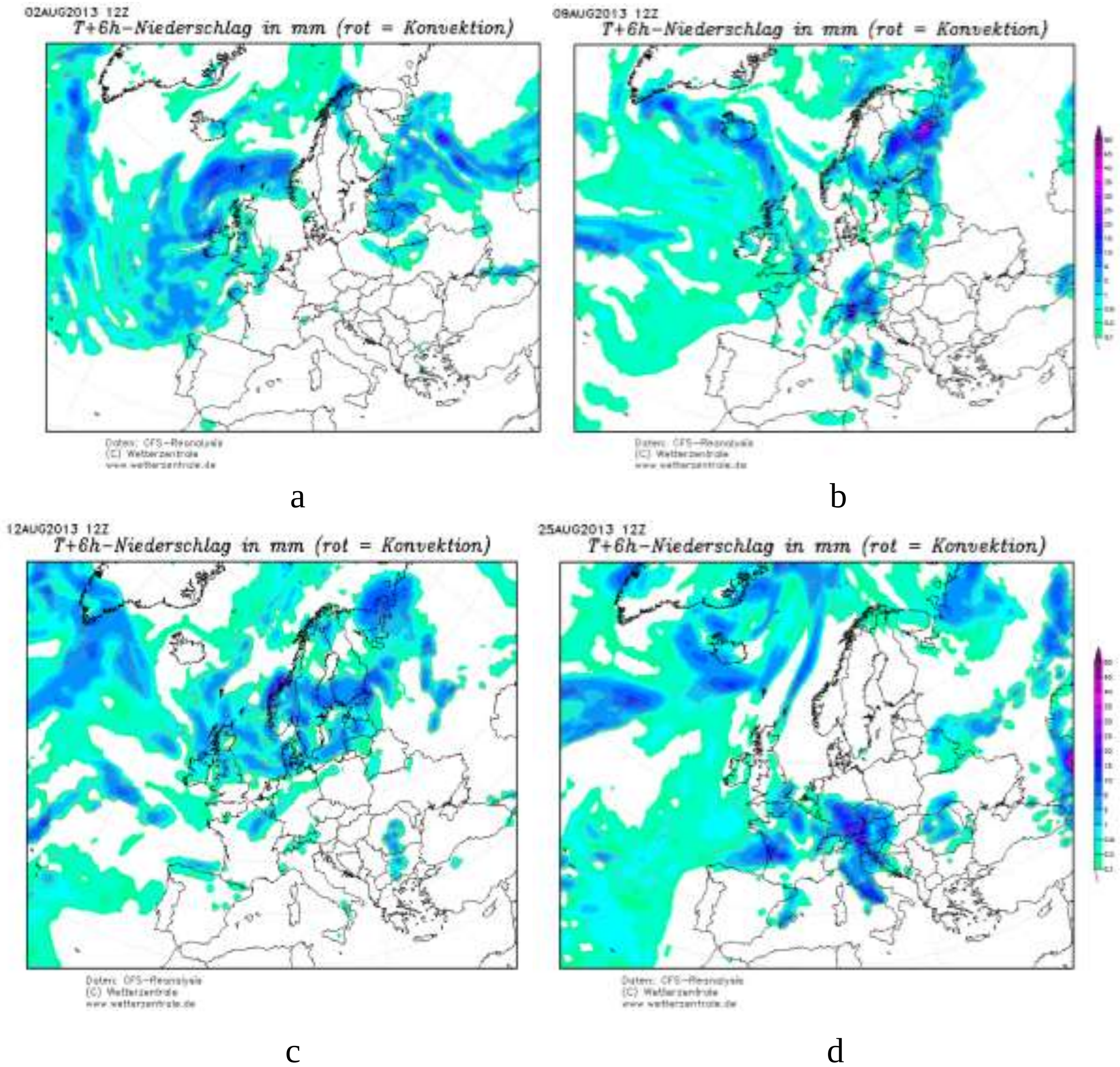

Figure 4. - Precipitation at 12:00 UTC for: (a) 02.08.2013, (b) 09.08.2013, (c) 12.08.2013, (d) 25.08.2013. [19]

During the first decade of January, the cyclonic type of weather dominated in the NWFD. By the middle of the first decade, for a short time, the NWFD area was under the influence of an anticyclone (Figure 5a). By the end of the decade, the nature of the weather again changed to cyclonic. The second decade was rather unstable. In the northern part of the NWFD, the cyclonic influence was mainly noted. In the southern part, the anticyclonic influence dominated (Figure 5b). Generally, the beginning of the third decade was also quite unstable. During the first days, the

NWFD area was mainly under the influence of a cyclone. By the middle of the decade, it was under the anticyclonic influence (Figure 5d). However, by January 27-28, the cyclonic influence increased, and the area again became under the influence of a cyclone (Figure 5c).

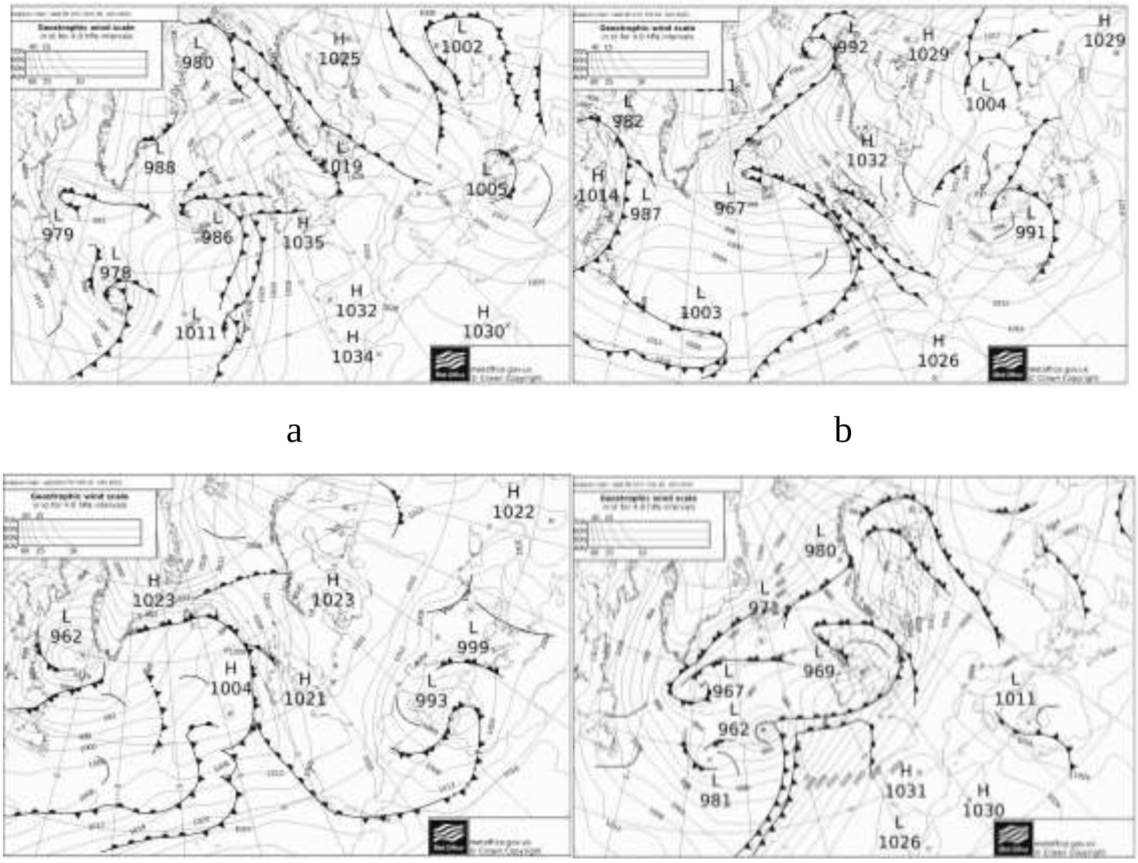

a b c d

Figure 5. - Surface Analysis maps at 00 UTC for: (a) 06.01.2013, (b) 18.01.2013, (c) 25.01.2013, (d) 29.01.2013. [18]

Nighttime air temperatures during the first decade of January in the NWFD ranged from 0...3 °C up to -33...- 36 °C. Daytime temperatures did not differ much from nighttime ones. These ranged from 0...3 °C to -30...- 33 °C. By the end of the decade, a cold snap was observed (Figure 6a). The second decade was colder than the first. Nighttime temperatures ranged from -3...- 6 °C to -39...- 42 °C in some areas in the northeast of the NWFD. Daytime temperatures ranged from 0...3 °C to

-36... -39 °C (in rare cases, in the northeast of NWFD, the temperature dropped below -40 °C). Nighttime temperatures in the third decade ranged from 0...3 °C (in the western regions by the end of the decade) to -39...- 42 °C (in the northeastern regions at the middle of the decade). Daytime temperatures were similar: -39...- 42 °C. By the end of the decade, there was observed moderate warming (Figure 6b).

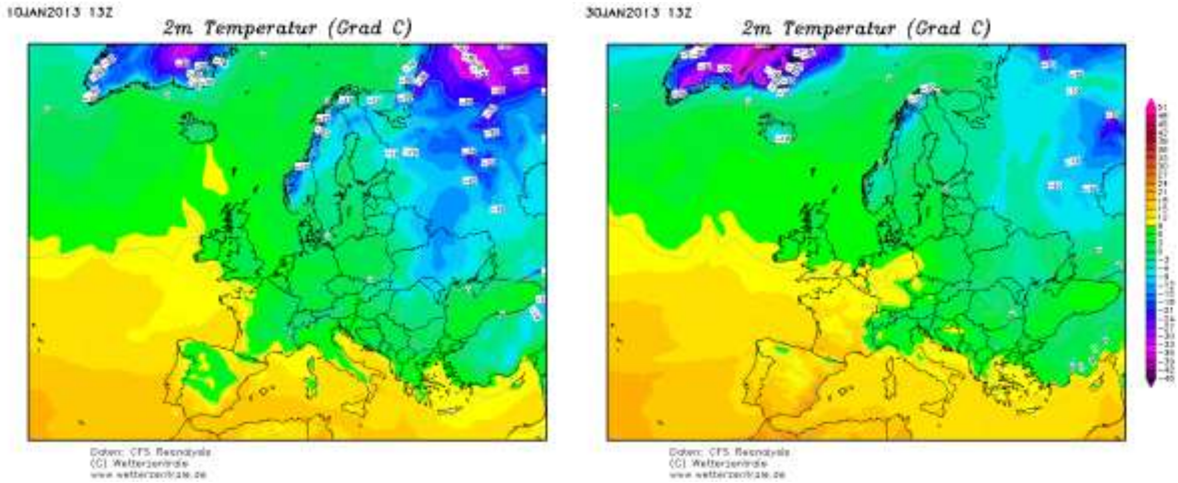

a b

Figure 6. - Air Temperature (2m) at 12:00 UTC for: (a) 10.01.2013, (b) 30.01.2013. [19]

During January, slight snow precipitation was observed throughout the entire area of the NWFD. Moderate snow precipitation was observed at the beginning of the first decade due to the cyclonic effect (Figure 7a). During the second decade, moderate precipitation was observed in the northeastern parts of NWFD at the beginning of the decade (Figure 7b), and in the west at the end of the decade (Figure 7c). It was due to the cyclonic effect. During the third decade, moderate precipitation was also observed at the beginning of the decade (Figure 7d) due to the cyclonic impact.

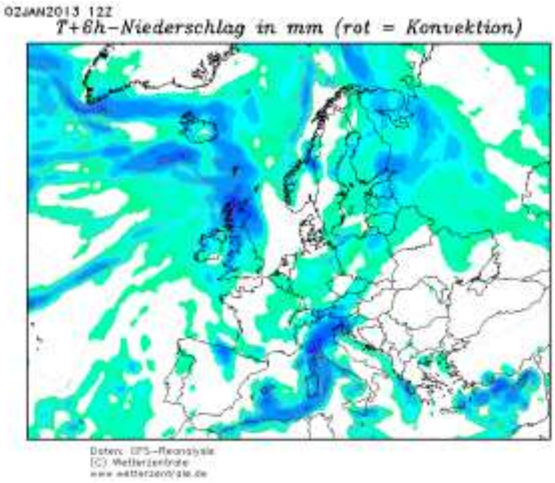

a

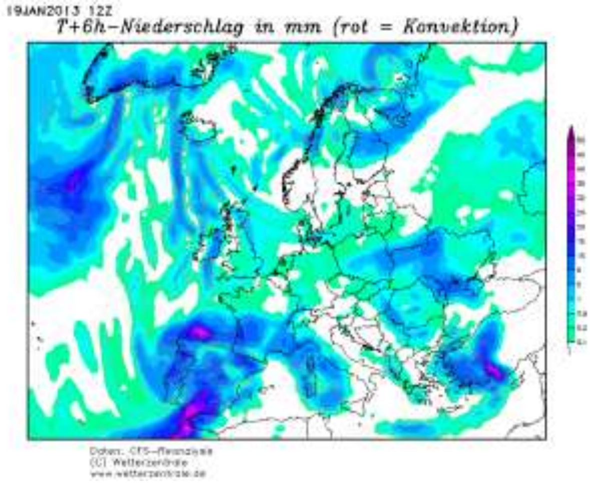

b

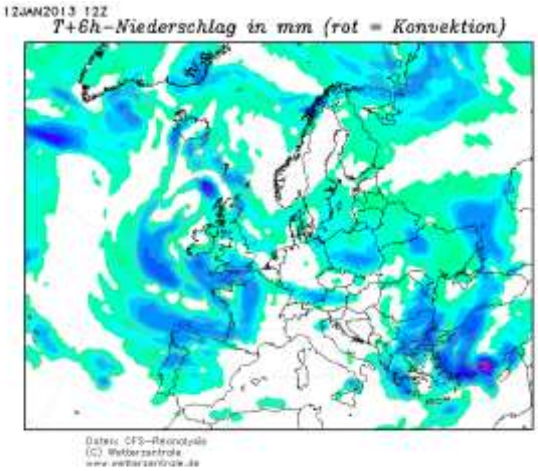

c

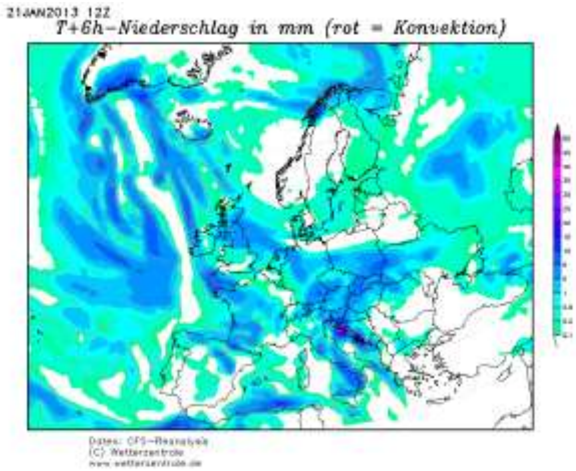

d

Figure 7. - Precipitation at 12:00 UTC for: (a) 02.01.2013, (b) 19.01.2013, (c) 12.08.2013, (d) 21.01.2013. [19]

2.4. Research tool: online integrated meteorological chemical-aerosol model Enviro-HIRLAM

2.4.1. Model history

Chemical weather forecasting (CWF), as a field of atmospheric modeling, has emerged in the last decades. This field is usually considered as a simplified concept of the autonomous launch of atmospheric chemical transport (ACT) models with operational numerical weather prediction (NWP) data as the driving force [20]. In the 1980s, were the first attempts to create online models for air pollution and meteorology [21], [22], [23]. These were intended for environmental applications. In the 1990s, the first chemical climate models were used for climate applications [24], [25], [26], [27]. The process of the online integration of the ACT models and mesoscale meteorological models gives an opportunity to transfer meteorological 3-D data fields to the ACT model at each time step. It allows to analyze the non-linear feedbacks of air pollution on the meteorological processes, climate forcing, and atmospheric chemical composition. This is a very important advancing for the future of the atmospheric modeling system, as well as for Earth System Modelling (ESM) in common. It leads to a new modern generation of seamless coupled models for the forecasting of chemical, meteorological, and biochemical weather. The way to realize this concept was suggested on European Example. The Environment - High Resolution Limited Area Model (Enviro-HIRLAM), is an entirely online integrated Numerical Weather Prediction (NWP) and Atmospheric Chemical Transport (ACT) modeling system. The development of the Enviro-HIRLAM was started in the 2000s, at the initiative of the DMI. It is now used in several countries. This modeling system is used for various research projects. It has also been used to study the atmospheric composition in China [28], [29] - since 2016, and for the operational forecasts of pollen in Denmark - since 2009 [30], [31].

2.4.2. Model structure

The Enviro-HIRLAM model is used for the research and forecasting of meteorological, chemical, and biological weather. The schematic of the model is shown in Figure 8. Initially, the modeling system was developed by the Danish Meteorological Institute (DMI, Copenhagen, Denmark), and then further with other collaborators from different countries. Nowadays, the European HIRLAM-ALADIN joint consortium includes the Enviro-HIRLAM as a baseline system in the HIRLAM Chemical Branch [32]. In Europe, it was the first mesoscale online coupled model that allowed to consider two-way feedbacks between meteorology and chemistry [33]. The main stages of the model development included the following. At first, the model was nested with high resolution. Secondly, the model parameterizations were improved through resolving PBL and SL structures. The urbanization schemes were implemented in the NWP part of this model. The improvement of the advection schemes as well as emission inventories is also a part of the model development. The mechanisms of gas-phase chemistry were implemented as well as the aerosol dynamics. The aerosol feedback mechanism was also realized in the model. The first version of the model was based on the DMI-HIRLAM version of the NWP model. It contained online integrated pollutant transport and dispersion [34], deposition, chemistry, and indirect effects [35], [36], and later aerosol dynamics for sulfur particles [37], [38]. The meteorological part of the model was upgraded by implementing the urban sublayer parametrizations. It makes the model suitable for the forecasting of chemical weather. Dynamic core has also been improved by adding a locally mass conserving semi-Lagrangian numerical advection scheme [39, 40, 41]. It increases forecast accuracy and enables implementation of the longer runs performing.

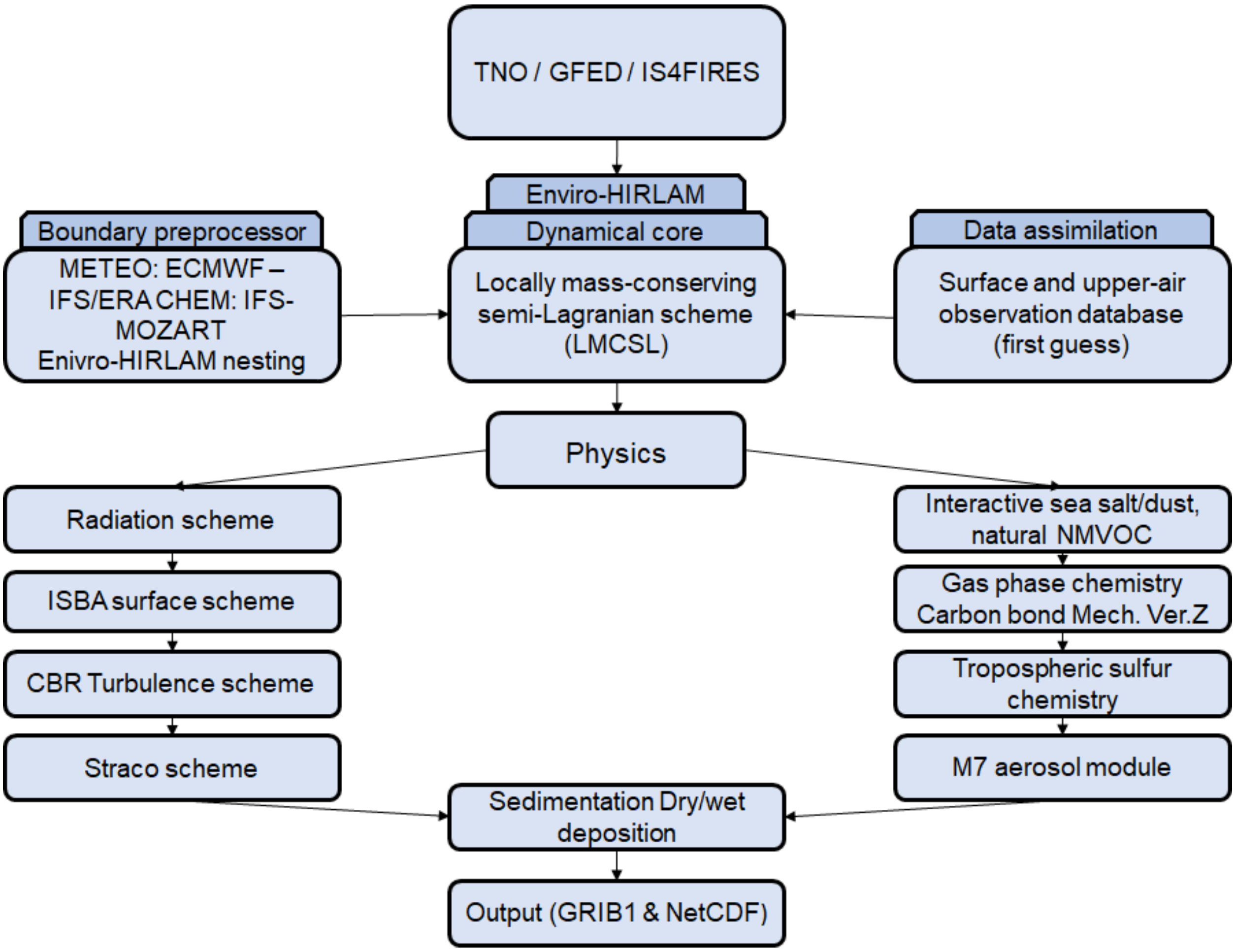

Figure 8. - The Enviro-HIRLAM structure schematic.

Due to the fact that in this work the case of atmospheric pollution with sulfur dioxide is investigated, the tropospheric sulfur chemistry cycle module (TSCCM) is of particular interest. TSCCM in Enviro-HIRLAM is used for long-term runs (up to one year). It is based on the sulfur cycle mechanism [42]. Three prognostic species are treated. The first one is dimethyl sulfide (DMS). The second one is sulfur dioxide (SO_2). And the third one is sulfate. The mechanism includes SO_2 and DMS oxidation. This process is due to the hydroxyl (OH) and DMS reactions with nitrate radicals (NO_3) in the gas-phase part. The chemistry of the heterogeneous aqueous phase is presented by the oxidation reactions of SO_2 , H_2O_2 , and O_3 . The accounting of the SO_2 dissolution effect (in the aqueous phase) is described by Henry's law. To prescribe the three-dimensional oxidant fields of OH, H_2O , NO_2 , and O_3 , the global chemistry transport model for

OZone And Related chemical Tracers MOZART [43] is used. The sulfate formed in the gas phase is counted as gas. It can be condensed on the pre-existing aerosols. In addition, it might be nucleated by the aerosol microphysics module, so-called the M7 module [44]. It is important to note that the in-cloud produced sulfate is accumulated on the coarse-mode aerosols and on already existing accumulations. The M7 and TSCCM modules are used together. It allows to decrease in computational cost, and it is relatively simple. The Carbon Bond Mechanism version (CBM-Z) gas-phase chemistry and M7 module are not used together due to several reasons. The first reason is that the secondary organic aerosols are not included in the M7. The second reason is due to quite expensive computational cost for joint using CBM-Z and M7 modules for both atmospheric composition and weather forecasting [45].

2.4.3. Extracting and preprocessing of meteorological and atmospheric composition input data

Before starting the model simulation process, it is necessary to pass the preprocessing phase. It includes the extraction and preparation of the required data for the simulation. To extract required input data files from the data repository (data archive system at ECMWF) source, it is required to write a python script, following a series of technical steps. First of all, it is important to create a temporary directory in which to extract a data file, and specify the exact name of such file (the file name consists: year, month, day, hour, forecast length in UTC time, and parameter of the retrieving data). In addition, it is important to indicate the required terms of retrieving data. The next step is the correct selection of the options for the Meteorological Archival and Retrieval System (MARS) request. There are several reanalysis data options. For the Enviro-HIRLAM simulations, the fifth generation ECMWF atmospheric reanalysis (ERA-5), and the Copernicus Atmosphere Monitoring Service (CAMS) Reanalysis are both required as input for the model run. ERA-5 provides a large number of oceanic, atmospheric, and climatic variables.

It covers the Earth by a 30x30 km horizontal resolution grid and resolves the atmosphere with 137 vertical levels. The height is from the surface up to 80 km. The required meteorology related input data include: the sea surface temperature (SST) and meteorological initial and boundary conditions (ICs/BCs). The following parameters are extracted: *stl1* (soil temperature at level 1, [K]), *ci* (sea ice area fraction, [0 - 1]), *lsm* (land-sea mask, [0 - 1]), *sst* (sea surface temperature, [K]). Meteorological ICs/BCs include the following extracted parameters: *q* (specific humidity, [kg/kg]), *lnsp* (logarithm of the surface pressure, dimensionless), *z* (geopotential, [m2/s2]), *t* (air temperature, [K]), *u* (component of wind speed, [m/s]), *v* (component of wind speed, [m/s]). The CAMS provides 3-dimensional time-consistent fields, which include chemical species (aerosol and greenhouse gases, GHG). In this case, it is divided on AER (aerosols) and GRG (gases) datasheets. AER includes the following parameters: *aermr04* (dust aerosol 0.03 - 0.55 um mixing ratio [kg/kg]), *aermr05* (dust aerosol 0.55 - 0.9 um mixing ratio [kg/kg]), *aermr06* (dust aerosol 0.9 - 20 um mixing ratio [kg/kg]), *aermr07* (hydrophilic organic matter aerosol mixing ratio [kg/kg]), *aermr08* (hydrophobic organic matter aerosol mixing ratio [kg/kg]), *aermr09* (hydrophilic black carbon aerosol mixing ratio [kg/kg]), *aermr10* (hydrophobic black carbon aerosol mixing ratio [kg/kg]), *aermr11* (sulphate aerosol mixing ratio [kg/kg]). GRG includes following parameters: *o3* (ozone O_3 [kg/kg]), *so2* (sulphur dioxide SO_2 [kg/kg]), *no2* (nitrogen dioxide NO_2 [kg/kg]), *no* (nitrogen monoxide NO [kg/kg]), *h2o2* (hydrogen peroxide H_2O_2 [kg/kg]), *oh* (hydroxyl radical OH [kg/kg]), *no3* (nitrate radical NO_3 [kg/kg]), *ho2* (hydroperoxyl radical HO_2 [kg/kg]), *dms* (dimethyl sulfide [kg/kg]).

The next option for extraction is «*class*». It is the ECMWF classification for data. Class for ERA-5 data is defined as «*ea*». For the CAMS, it is defined as «*cm*». The option "dataset" is dataset type. In this case, it is defined as ERA-5. The option «*date*» is represented by the year, month, and day of the extracted data. It is defined in the following format: YYYY-MM-DD. The option: «*expver*» is a unique code (version). It is assigned for each ECMWF model run. The option «*grid*» defines a target grid. The option «*level list*» includes a list of the vertical levels on which data will be extracted. The option «*level type*» describes a type of the vertical modeling levels. The option «*param*» is the ID definition of the retrieved parameters. The option «a*rea*» describes the required sub-area of the data to be retrieved. The option «*rotation*» is defining the position of the South Pole of the rotated grid as latitude/longitude in degrees. The option «*step*» is a time step for the forecast. The option "stream" identifies the forecasting system. The option «*time*» specifies the time of the data in the following format: HH-MM. The option «*type*» selects between images, observations, or fields, and defines some of the valid remaining keywords of the request. The option «*target*» defines a file into which data is to be written after retrieval or manipulation.

Now, let's consider the observation data type. Observation data is presented as a Binary Universal Form for the Representation of meteorological data (BUFR) format, with conventional observation type. BUFR data file contains the following options extracting necessary data through the MARS request. The first option is «*type*» has the same meaning, like for the reanalysis data (see above in this section) The option «*OBSTYPE*» describes the subtype for an observation (BUFR code) or, for images, the satellite channel. In this case «*OBSTYPE*» is equal to «*CONVENTIONAL*». The options «*Area*», «*Date*», «*Time*» and «*Target*» have the same meaning, as for the reanalysis data (see above in this section). Data extraction for the Enviro-HIRLAM model runs is based on the table system. To enable the unpacking of the required elements from the observations, the tables provide a list of keys. All observation data are presented in the BUFR format [46].
In this work, to prepare the Enviro-HIRLAM model for simulations, it was necessary to extract and download the described above input data for the following time periods - 1-31 August 2013 and 1-31 January 2013. The ECMWF archives were the main source for this required data. The data extraction and downloading process passed through the ECMWF server. The following data were extracted: 1) ERA-5 meteorological ICs/BCs for the 3-hour terms 00:00 - 21:00 UTC for each day for the selected months; 2) AER (aerosols) data for the 3-hour terms during 00:00 - 21:00 UTC for each day for the same months; 3) identically, as for AER, it was done for

the GRG (gases) data; 4) SST data for the two terms - 00:00 and 12:00 UTC on each day for the same months; 5) BUFR conventional observation data, for the 3 hours terms 00:00 - 21:00 UTC on each day for the same months.

2.4.4. Preprocessing emission inventories

The Enviro-HIRLAM model runs include also the following emission inventories (EIs): anthropogenic, biomass burning (wildfires), and natural ones. Some of these EIs are based on collected and analyzed information from various sectors of the economy, satellite, and ground-based observations, etc. EIs also depend on changes in land-cover (forests, low vegetation, urban areas, water surfaces, etc.), land use (transportation, agriculture, industry, etc.), meteorological/ climatic conditions, and these differ for each simulation time step. Therefore, they are processed in different ways. The shipping emissions include (given in geographical latitude/longitude domain) the following data: sulphur dioxide (SO_2, in kg m-2 s-1), *BC* (kg m-2 s-1), organic carbon (*OC*, kg m-2 s-1). These are taken from the Intergovernmental Panel on Climate Change (IPCC) report on emissions. In particular, the inventory for anthropogenic emissions was developed by the Netherlands Organization for Applied Scientific Research (TNO) [47]. It is a dataset of yearly accumulated emission fluxes for different gases (such CO, CH_4, NOx, SO_2, NH_3) particulate matter (PM), and non-methane volatile organic compounds (NMVOCs). The horizontal resolution is about 0.06 x 0.12 deg. It covers entire Europe and adjacent geographical areas including the European part of Russia. The emissions for NMVOCs are divided into 25 VOC compound groups by source sectors of the country [48]. The emissions for PM2.5 and PM10 are divided into 6 aerosol species (*OC, Na,* SO_4, *BC,* other coarse primary and fine primary particles). Due to the fact that the datasheet includes accumulated surface fluxes, it is important to redistribute them in order to present monthly, weekly, and diurnal emissions variability. The emissions may occur at various heights. Thus, the emission

preprocessor includes both vertical and temporal profiles, following TNO's SNAP codes vs. different aerosols and gaseous species.
The aerosols and gaseous natural emissions are fully interactive, and calculated online. There are emissions of dimethyl sulfide (DMS; Nightingale et al., 2000) from oceans/seas, soluble sea salt [49], and insoluble mineral dust aerosols. Both dust and sea salt aerosols emissions take place in two modes - course and accumulation ones. The Enviro-HIRLAM model utilizes the inventory for the global biomass burning (wildfires) emissions [50], [51] developed by the Finnish Meteorological Institute (FMI). It has a similar structure with anthropogenic EI, except a horizontal resolution as well as numbers and types of available gaseous and aerosol species. For this work, the emission inventory Evaluating the Climate and Air Quality Impacts of Short-Lived Pollutants (ECLIPSE, 5th version) [52] was used. It includes anthropogenic emissions such as SO_2, NOx, NH_3, $NMVOC$, BC, OC, $PM_{2.5}$, PM_{10}, CH_4, $and\ CO.$

2.4.5 Setting up the model - gridded domain

For this modeling domain (Figure 9), the following parameters were selected: Number of grid points along longitude (NLON) = 442; Number of grid points along latitude (NLAT) = 340; Number of model vertical levels (NLEV) = 40; Coordinates of South pole - latitude (POLAT)= -10.0 [deg]; Coordinates of South pole – longitude (POLON) = 40.0; Dynamics time step (NDTIME) = 120 [sec]; Horizontal resolution ($\Delta LAT = \Delta LON$) = 0.05 [deg].

Figure 9. - Selected model domain (N05).

Following Mahura et al. (2005), to calculate and check parameters for the modeling domain, the following procedure was utilized. At the first step, a horizontal resolution $\Delta LAT = \Delta LON$ in degrees for a new modeling domain (NMD) was selected. Then, the number of the passive boundary points (NPBP) was chosen, and the total number of the passive boundary points (NBNDRY) was calculated (5):

$$NBNDRY = 2 * (NPBP + 1) \quad (5)$$

In this work, a resolution equal to 0.05 degrees, and an NMD value equal to 4 were selected. Hence (6):

$$NBNDRY = 2 * (NPBP + 1) = 2 * (4 + 1) = 10 \quad (6)$$

In the next step, it's important to check that a number of the grid points along the longitude $NLON_{NWP}$ satisfies a set of predefined special conditions (*n, m, p*). I.e. the selected $NLON_{NWP}$ value should exist [53]. This value corresponds to certain conditions. For the selected domain, the conditions are the following: *n = 4, m = 3, p = 0.* Then, $NLON_{NWP}$ value should satisfy the following expression (6, 7):

$$2^n * 3^m * 5^p = NLON_{NWP} \quad (7)$$

$$2^4 * 3^3 * 5^0 = 432 \quad (8)$$

The next step is to calculate the total number of grid points in NMD $NLON_{NWP}$ and $NLAT_{NWP}$ along the longitude and latitude direction following these formulas (9, 10):

$$NLON_{NMD} = NLON_{NWP} + NBNDRY \tag{9}$$

$$NLAT_{NMD} = NLAT_{NWP} + NBNDRY \tag{10}$$

In this work it will be (11, 12):

$$NLON_{NMD} = NLON_{NWP} + NBNDRY = 432 + 10 = 442 \tag{11}$$

$$NLAT_{NMD} = NLAT_{NWP} + NBNDRY = 330 + 10 = 340 \tag{12}$$

The next step - selection of a value for the south-east and north-west corners of NMD in the rotated system of coordinates. In this case it will be (13, 14):

$$EAST = \ 6.025;\ SOUTH = -23.527; \tag{13}$$

$$NORTH \ = -6.577;\ WEST \ = -16.025. \tag{14}$$

Then, it's important to define values for the WEST-EAST boundaries of NMD in the rotated system of coordinates. It should cover the selected area of interests, and satisfy the following conditions:

$$\frac{|WEST - EAST|}{\Delta LON} = NLON_{NMD} - 1 \tag{15}$$

The next step, similarly to the previous one, is a selection of the values for the NORTH-SOUTH boundaries of NMD:

$$\frac{|NORTH - SOTH|}{\Delta LAT} = NLAT_{NMD} - 1 \tag{16}$$

2.4.6. Simulation process

Before the model launching, it’s important to set up several pre-launching options. First of all, it’s necessary to specify the model domain with a specific set of parameters (see also section 3.4.5). Secondly, it's important to activate (i.e. included/ not included) settings for the chemistry or/and aerosol schemes. Thirdly, to activate setup for the anthropogenic and biogenic emissions presence (Included / Not included). At fourth, to activate setup for the presence of the dry and wet deposition (Included/Not included). At fifth, to activate setup for the Aerosol-Cloud-Radiation direct and indirect feedbacks (Included/Not included). At sixth, activate the setup for the locally mass conserving semi-Lagrangian (LMCSL) scheme for advection, for both the meteorological variables and chemical species. At seventh, to activate setup for the meteorological data assimilation. After these options are selected, the Enviro-HIRLAM model system can be launched with the following command: «Hirlam start DTG=YYYYMMDDHH DTGEND=YYYYMMDDHH LL=XX». Here, «DTG» and «DTGEND» are starting and ending dates for the model run. It is possible to check the simulation process progress at the supercomputer utilizing the following command – «squeue -u username». Technically, the simulation process is divided into several phases. First, «Init run»: this is the beginning of the model submission to the HPC system and initiating a simulation process. The next phase – «Preparing». It includes: checking of the configured model domain and numerical options, building climate generation files, preparing boundary condition files, and other preparations. The next is: date/time definition, running the model, making a cycle for directories creation, linking boundaries, merging with climate information, saving the intermediate output to logs-files, and other actions. The last phase of the model run on each cycle is post-processing. It includes archivation, process logs collecting, verification, and other «after-action» steps. Note, that these described above phases are repeated for every other subsequent term of the model run. The modeling output data are saved every 3 hours in the GRIdded Binary (GRIB) format files in the corresponding folders (YYYY/MM/DD/HH; where HH = 00, 06, 12, 18 UTCs).

2.4.7 Postprocessing and visualization of model output

For visualization convenience, the Enviro-HIRLAM output files were post-processed through converting to network Common Data Form (NetCDF) format files utilizing converter software - National Center for Atmospheric Research (NCAR) Command Language (NCL). To convert required files from GRIB to NetCDF format, the following command was used - "ncl_convert2nc file_name.grb" command. Thereafter, all converted files were prepared, these were used for visualization. For this purpose, the Panoply software was used. The Panoply is the application that allows plotting geo-referenced and other arrays from netCDF, HDF, GRIB, and other datasets. At first, it is important to upload the required output NetCDF file to the Panoply environment and to select a parameter for visualization and a type of plotting in geographical coordinates (in this case - lon/lat georeferenced). Next, it is necessary to choose the following options: map projection (in this work it is common for all plotted parameters - "Equirectangular Regional", model’s vertical level at which parameter will be plotted, horizontal grid spacing, grid style of plotting, scale range or interval of parameter’s changes, measurement unit for plotting of the selected parameter, useful tick format, scale caption, and colorbar, overlays settings (color, style, and weight). An example of such visualization is shown in Figure 10.

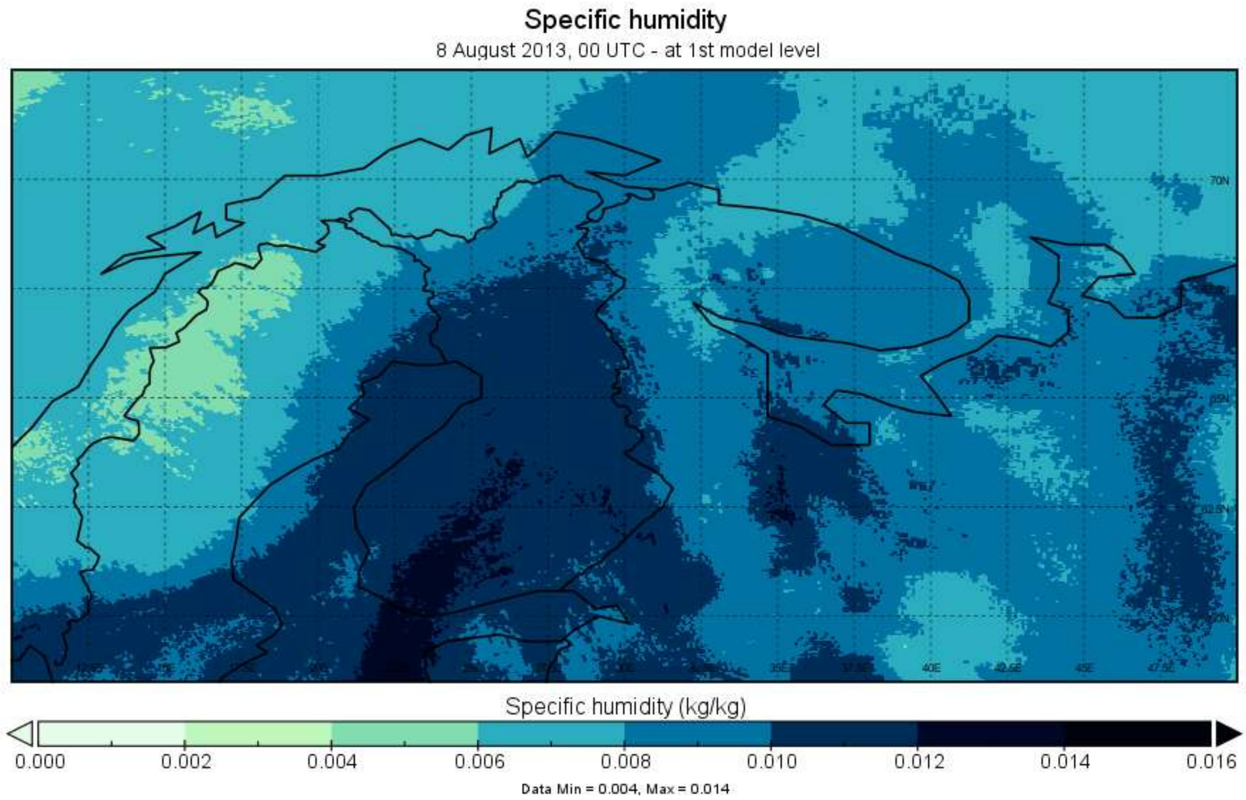

Figure 10. - Spatial variability of the specific humidity field on 08.08.2013, 00 UTC at 1 model level.

As we can see on Figure 10, in this case the measurement unit is [kg/kg], horizontal grid spacing along both latitude and longitude - 2.5 deg, gridded lines style - dots, scale range for selected meteorological parameter is from 0 to 0.016 [kg/kg] with accuracy of 3 digits, scale caption – «Specific humidity (kg/kg)», subtitle – «8 August, 00 UTC - at 1st model level», selected colorbar palette – «GMT_ocean_08.act».

3. Results and discussion

This section includes the results of visualization of the Enviro-HIRLAM model output for selected meteorological parameters to be used in the analysis of 3 regimes (temperature, wind, and humidity) of the planetary boundary layer (PBL) for the months of January and August 2013. Several parameters were chosen to investigate each regime. To analyze the temperature regime of PBL, it was decided to select the following parameters: air temperature at the 1st model level (~ 32m), at about 500, 1000, and 1500 meters. These heights were chosen due to the fact that the PBL height is approximately up to 1.5 km (although can vary depending on the specific meteorological situation and geographical/latitudinal location), and in this study, these regimes in the free troposphere are not in focus. To study the humidity regime of the PBL, it was decided to select the following parameters: cloudiness or total cloud cover [%], specific humidity at 4 model levels [kg/kg], large scale, and convective precipitation [kg/m^2]. It is important to note that only large scale precipitation was selected for January, while the large scale and convective precipitation were selected for August. It is due to the fact that convective clouds in most cases are observed in a warmer period, especially during the summer months. To analyze the wind regime of PBL, the following parameters were selected: wind speed [m/s] and direction [deg] at 10 meters, as well as at about 500, 1000, and 1500 meters. The highest attention in the analysis was paid to geographical regions of Karelia, the Kola Peninsula, the Leningrad region, the Scandinavian countries, as well as to the White, Barents, and Baltic seas.

3.1. Data analysis for temperature regime - August 2013

Analysis of the Enviro-HIRLAM model output showed that throughout August 2013, the Scandinavian peninsula and NWFD of Russia were exposed to warm air masses from the south (mostly in NWFD) and west (mostly in Scandinavian countries). The highest temperatures were observed in the first decade of August when almost the entire territory of the NWFD and the Scandinavian peninsula was under the influence of warm air mass (an example is shown in Figure 11). The air daytime temperature in the region of the Kola Peninsula, Karelia, and the Leningrad region reached 24...28 °C, in the Scandinavian countries 20...24 °C. Over the Baltic and White seas - 16...20 °C, and over the Barents Sea 12...16 °C.

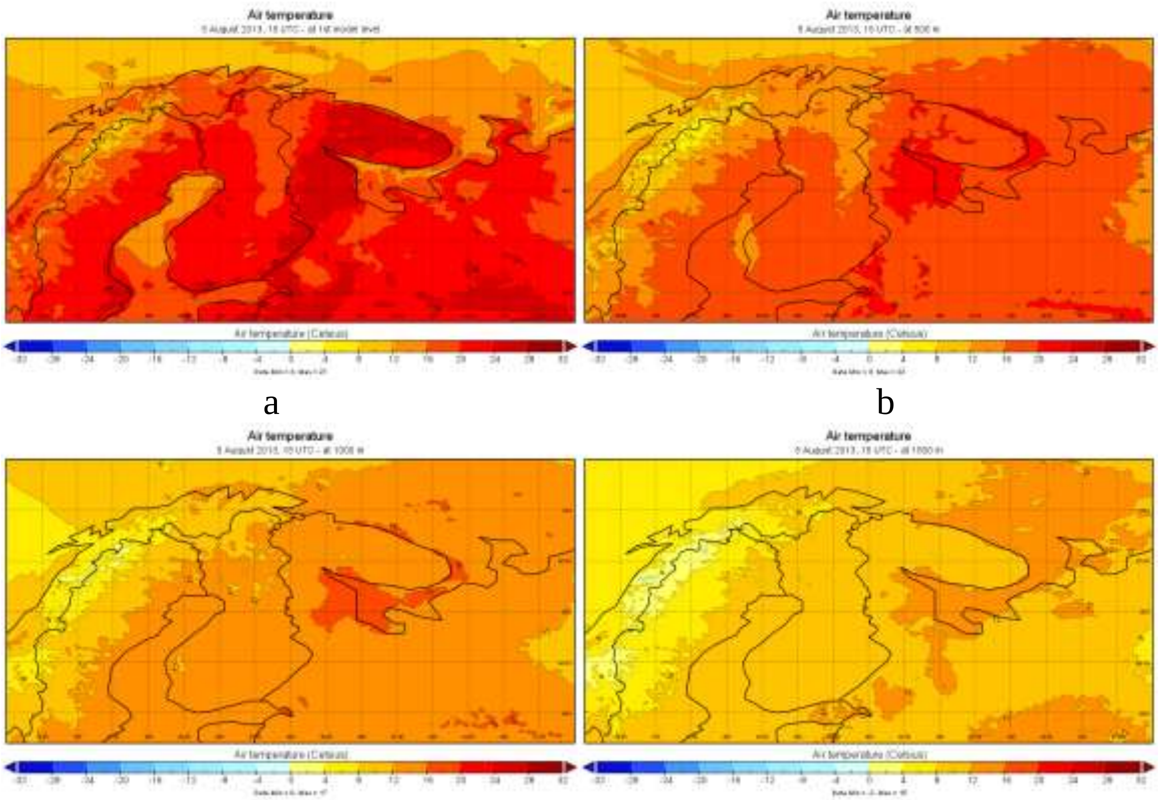

a b c d

Figure 11. - Spatial variability for the air temperature on 30.08.2013, 03 UTC at: (a) 1st model level (~32 m), (b) 500 m, (c) 1000 m, and (d) 1500 m.

In particular, the lowest daytime air temperatures in the studied areas were observed at the end of the month (Figure 12). The temperature on the Kola Peninsula was about 4...8 °C, in Karelia and the Leningrad region 12...16 °C. In the northern regions of the Scandinavian Peninsula 4...8 °C (similarly to the Kola Peninsula) and in the southern 8...12 °C. The air temperature at heights 1000 - 1500 m was negative in the northern regions of the Scandinavian peninsula. The temperature decreased with height (As expected).

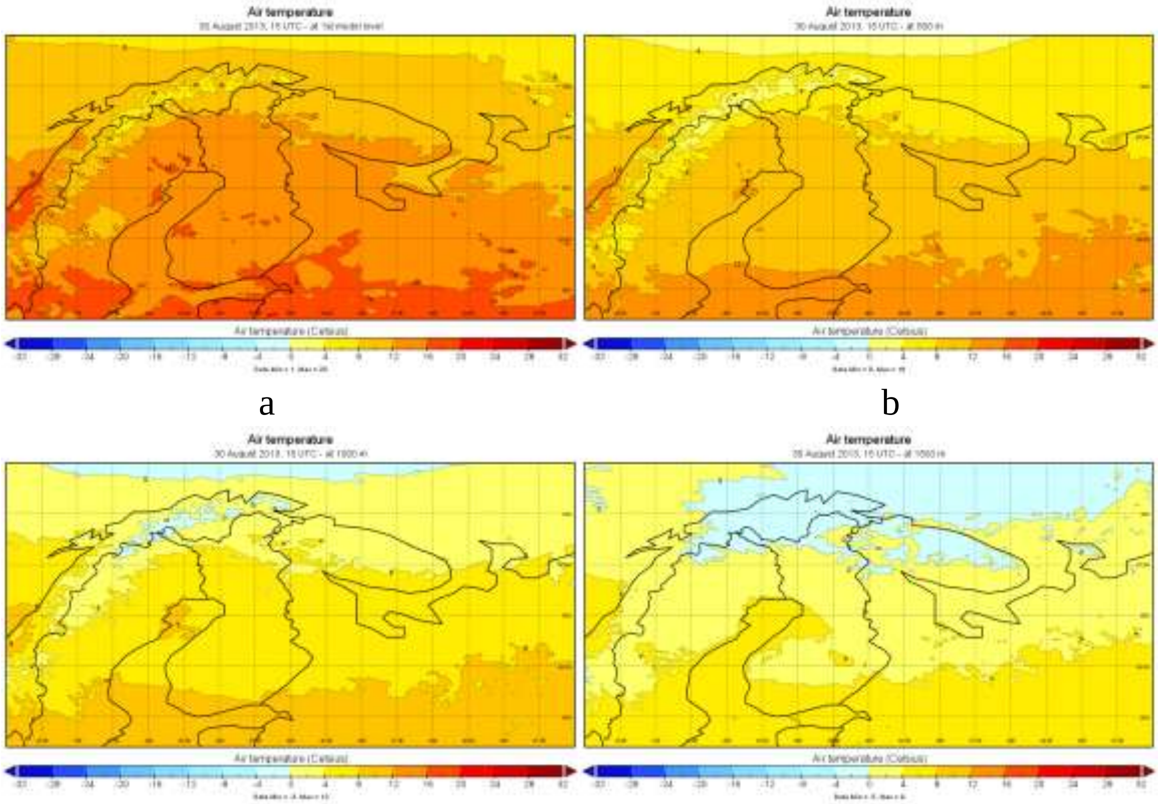

a b

c d

Figure 12. - Spatial variability for the air temperature on 30.08.2013, 15 UTC at: (a) 1st model level (~32 m), (b) 500 m, (c) 1000 m, and (d) 1500 m.

Analyzing the daily variation of air temperatures during August 2013, it is important to say that the minimum temperatures in most cases were observed at night - 03 UTC. The maximum temperatures were observed during the daytime - usually at 15 UTC. It is important to note that nighttime temperature drops were especially pronounced in the region of the Kola Peninsula, North Karelia, and the northern regions of the Scandinavian countries. At altitudes 500 - 1000 - 1500 m, the air temperature had a smoother diurnal variation - the difference between daytime and nighttime temperatures was less. The examples of air temperature daily cycle in August 2013 are presented in Appendix A1 - A4.

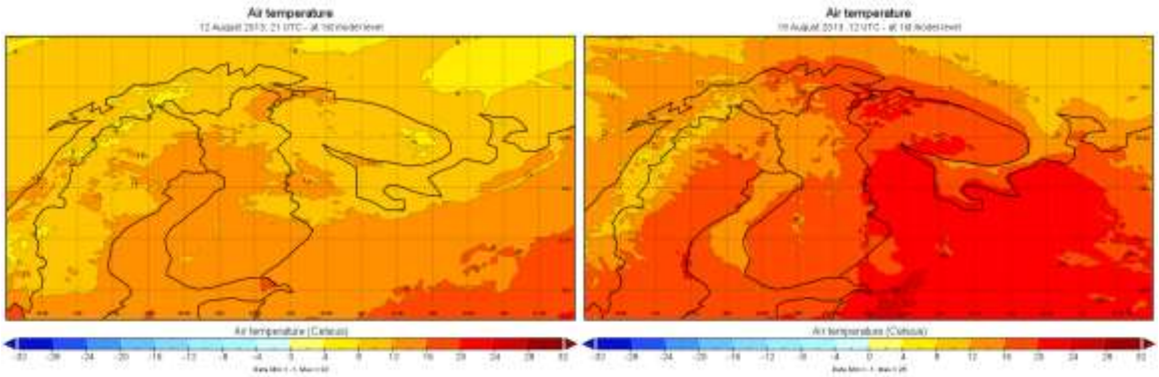

a b

Figure 13. - Spatio-temporal variability of the air temperature at the 1st model level: (a) 12.08.2013, 21 UTC, (b) 19.08.2013, 12 UTC.

Also, it is important to note that there is a possible influence of air pollution on changes in the temperature regime. An increase in temperature is noticeable in the northwestern part of the Kola Peninsula, where the city of Nikel is located (Figure 13). According to an analysis of the air pollution situation (see Chapter 2.2), in August there were 5 cases of sulfur dioxide elevated concentrations, up to 12 MAC. Accordingly, as both the direct and indirect aerosols effects were included in the model simulations, an added value to an increase in temperature can be linked to air pollution.

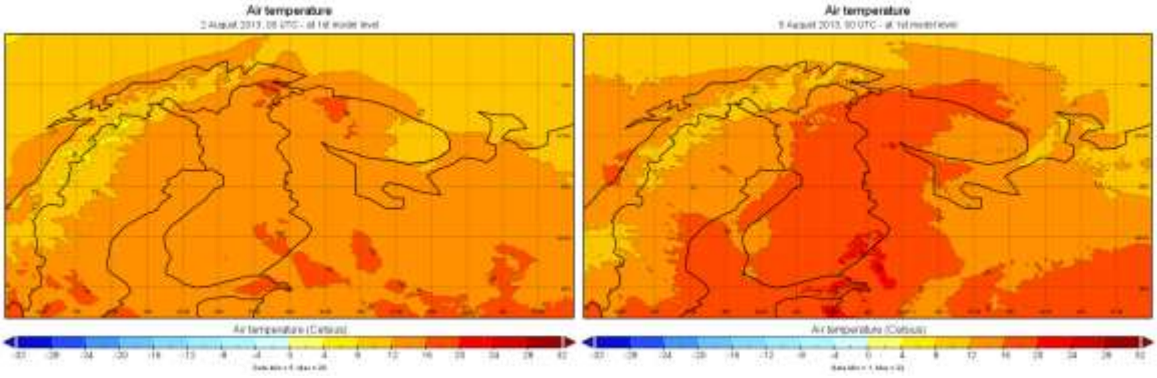

a b

Figure 14. - Spatio-temporal variability of the air temperature field at the 1st model level: (a) 02.08.2013, 00 UTC, (b) 05.08.2013, 00 UTC.

Also, Figure 14 shows a local increase in air temperature in the area of cities Svetogorsk (small size city) and St. Petersburg large metropolitan area, which might be associated with the influence of anthropogenic aerosol pollution. For the model simulations, the emission inventory data include anthropogenic emissions in these urban areas. And it is known that there are sources of emissions: pulp and paper mill in Svetogorsk, and in St. Petersburg - many different industrial enterprises.

3.2. Data analysis for humidity regime - August 2013

Analysis of the Enviro-HIRLAM model output showed that the most significant cloudiness over all studied territories was observed at the end of the first decade (Figure 14a) as well as in the second decade of August (Figure 15b, c, d). At the end of the first decade, it was caused by the passage of the atmospheric cyclone front west of the Norwegian coast on the 8th of August. In the second decade, on the 15th, heavy cloudiness was caused by a cyclone centered over eastern Finland. During 17-19 August, two cyclone fronts passed over the study areas west of the coast of Norway, and also caused intensive cloudiness.

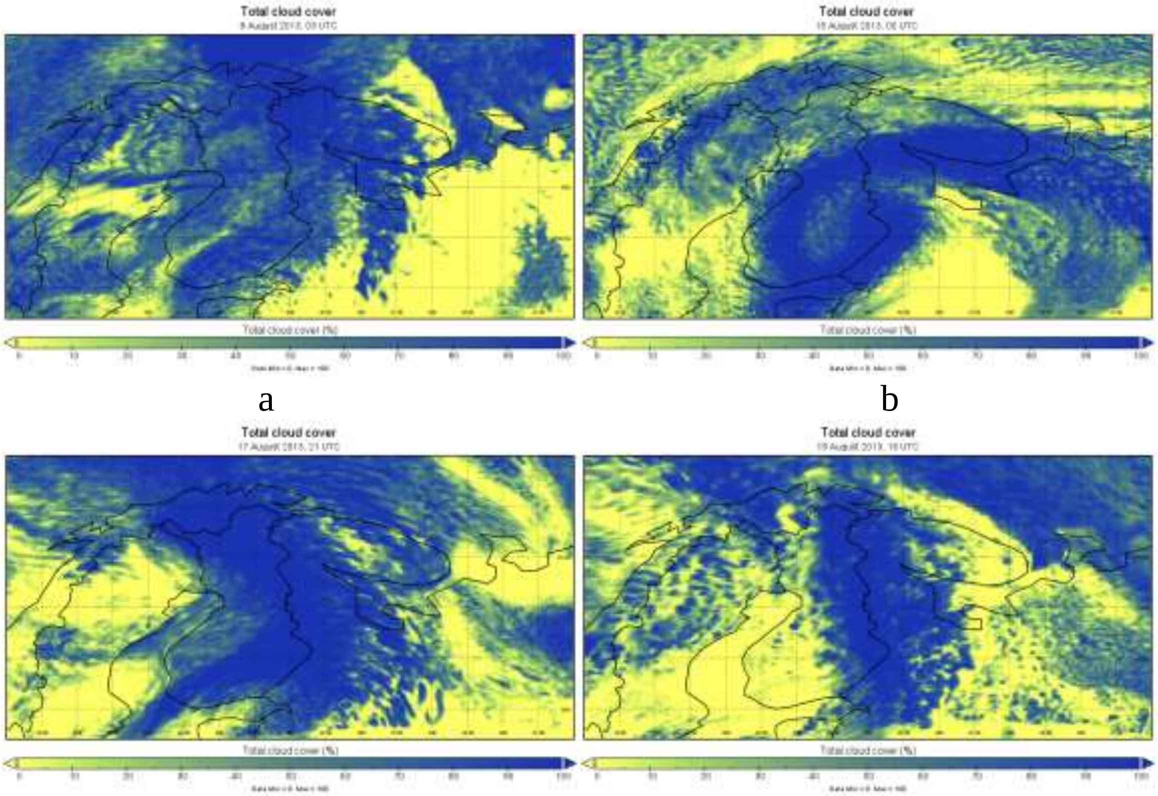

a b

c d

Figure 15. - Spatio-temporal variability of the total cloud cover field: (a) 08.08.2013, 03 UTC, (b) 15.08.2013, 00 UTC, (c) 17.08.2013, 21 UTC, and (d) 19.08.2013 15 UTC.

Accordingly, the passage of atmospheric fronts also caused quite intense convective precipitation in these periods of time. This is clearly seen in Figure 16.

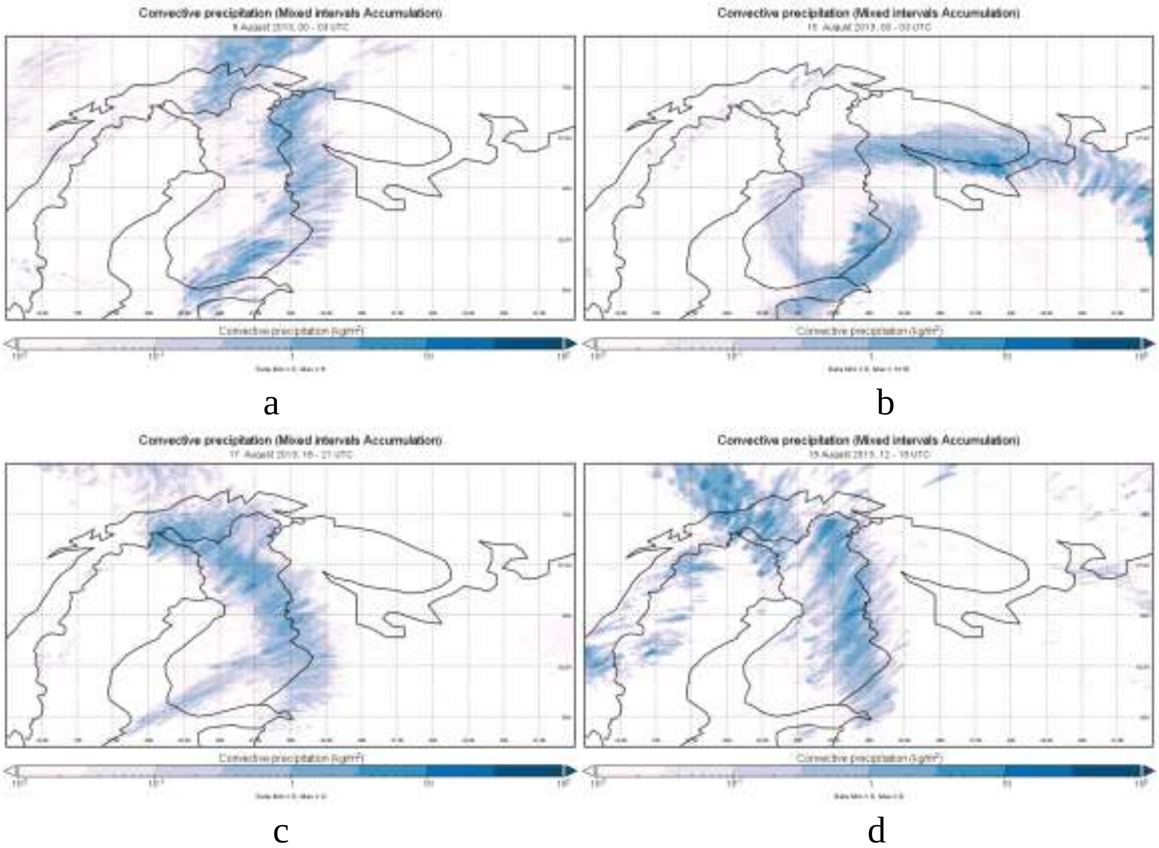

Figure 16. - Spatio-temporal variability of the convective precipitation field (accumulated for 3-hour interval): (a) 08.08.2013, 00-03 UTC, (b) 15.08.2013, 00-03 UTC, (c) 17.08.2013, 18-21 UTC, and (d) 19.08.2013, 12-15 UTC.

In August, the most noticeable was the transfer of moist air masses from the Atlantic Ocean to the continental part of Europe. Moist air masses, moving from the west to the east, affected both the Scandinavian countries and the NWFD of Russia.

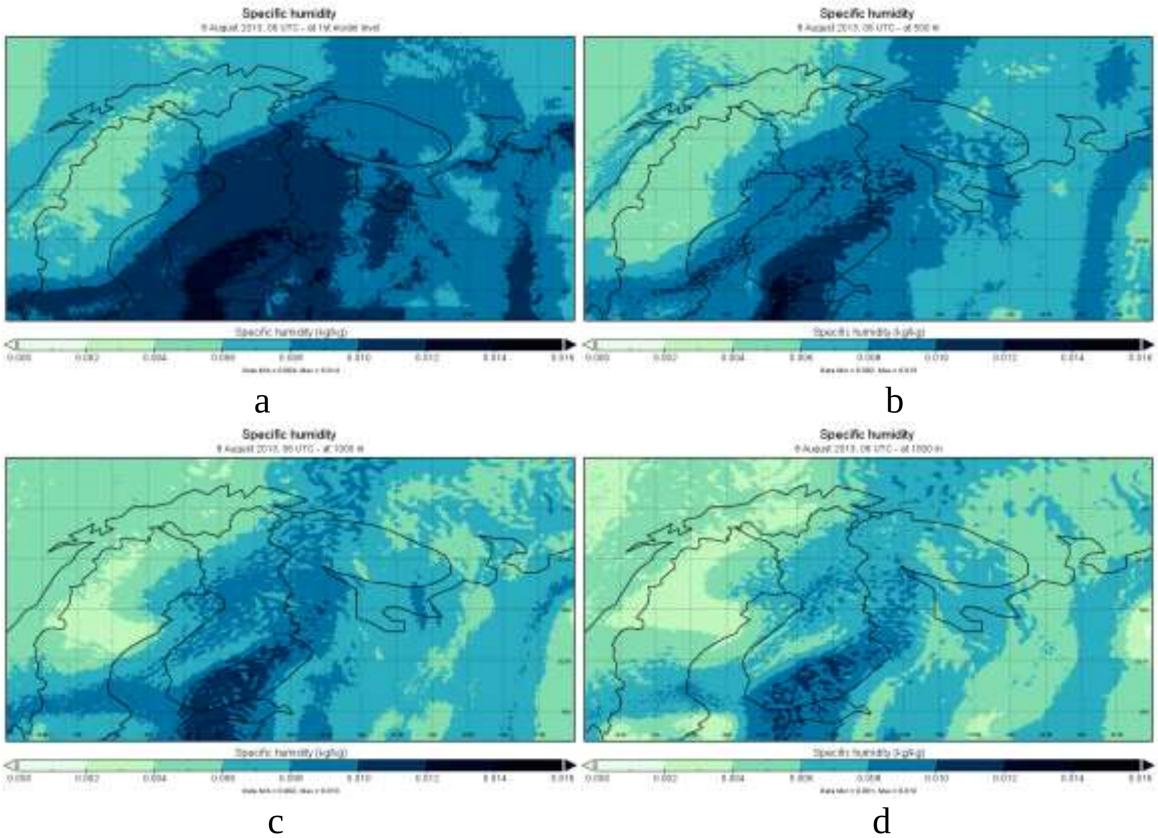

Figure 17 - Spatial variability of the specific humidity field on 08.08.2013, 06 UTC at: (a) 1st model level (~32 m), (b) 500 m, (c) 1000 m, and (d) 1500 m.

The most massive moist air masses were observed in the first (Figure 17) and second (Figure 18) decades of the month. The atmospheric transport of moist air masses was clearly visible at all model levels. Specific humidity with height changed in an expected way (i.e. decreased). The parameters of the PBL humidity regime in August 2013 did not have a pronounced diurnal variation; however, in some cases, it was noticeable that the absolute humidity reached its minimum by 12-15 UTC and its maximum at 00-03 UTC. The difference was small and amounted to 0.002 kg/kg~. The examples for specific humidity daily cycle in August 2013 are presented in Appendix D1 - D4; for total cloud cover - in Appendix B1; for large scale and convective precipitation and - in Appendix C1.

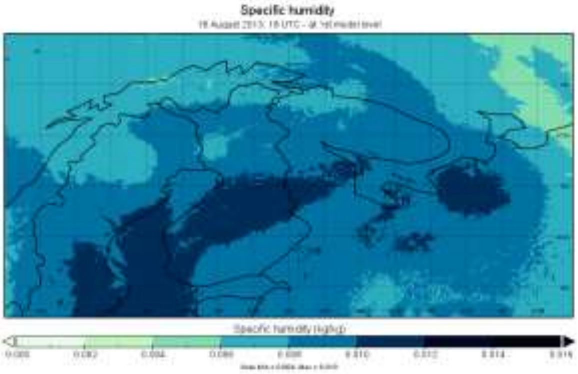

a

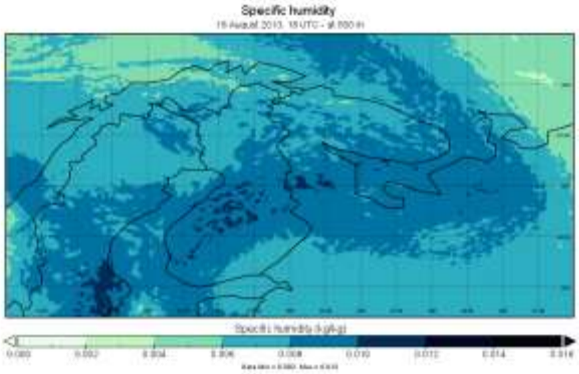

b

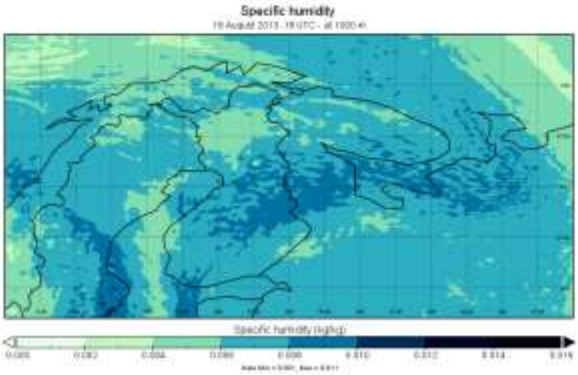

c

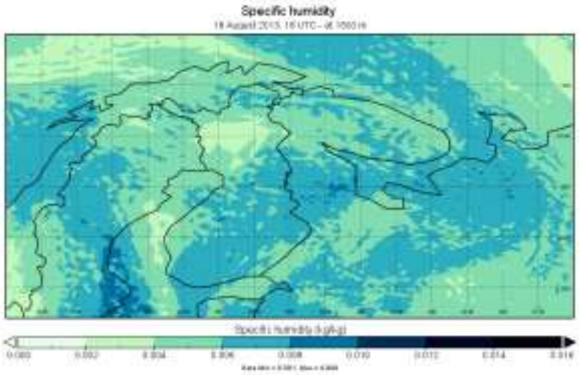

d

Figure 18 - Spatial variability of the specific humidity field on 18.08.2013, 18 UTC at: (a) 1st model level (~32 m), (b) 500 m, (c) 1000 m, and (d) 1500 m.

3.3. Data analysis for wind regime - August 2013

Analysis of the Enviro-HIRLAM model output showed that the PBL wind regime in August was characterized by dominated southerly and westerly winds for most of the month (an example is seen in Figure 19). On average, the wind speed at 10 meters above the ground was up to 8 m/s. And as expected, it increased with the height over the area of interest. The highest wind speed was usually observed over water surfaces

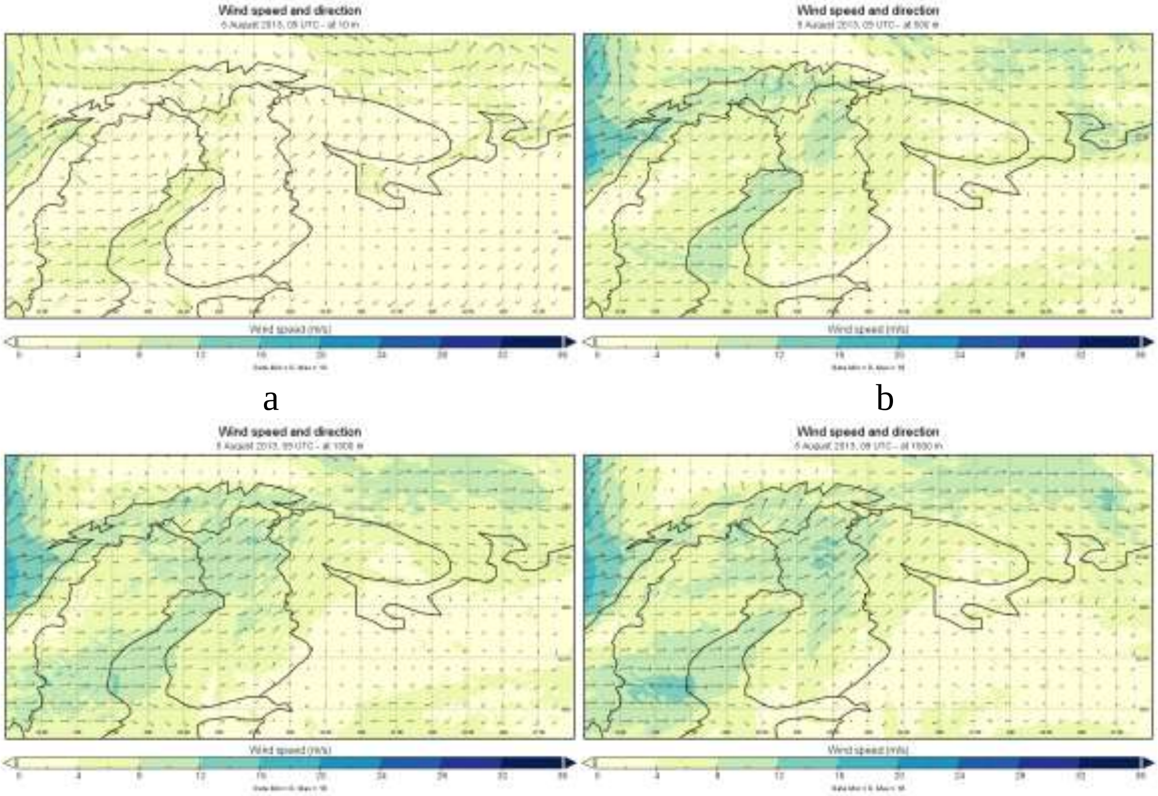

Figure 19 - Spatial variability of the wind speed and direction fields on 05.08.2013, 09 UTC at: (a) 10 m, (b) 500 m, (c) 1000 m, and (d) 1500 m.

The sharpest and most intense changes in both the wind speed and direction were observed at the moments of the impact on the region of baric formations. Such an example is shown in Figure 20 when the entire study area was under the influence of the cyclone centered over the region of Finland. The wind speed in such cases reached up to 12-16 m/s.

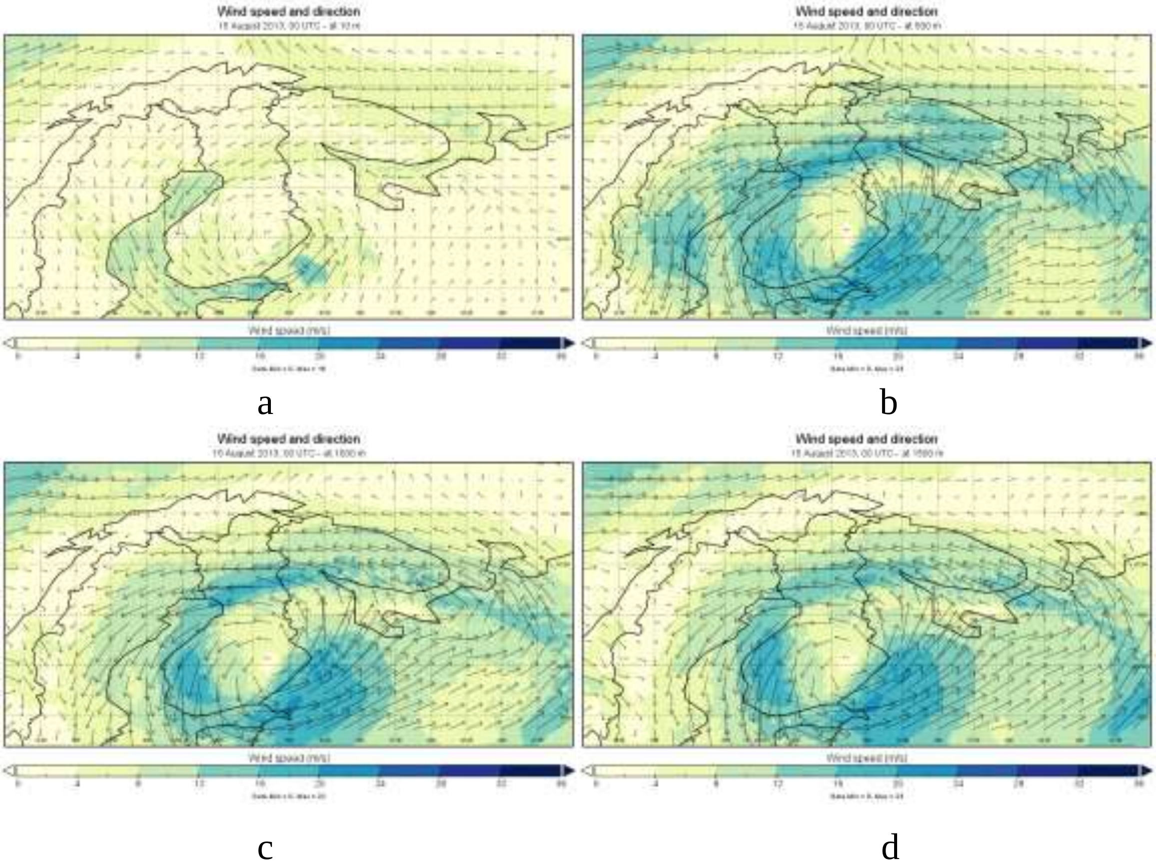

Figure 20 - Spatial variability of the wind speed and direction fields on 15.08.2013, 00 UTC at: (a) 10 m, (b) 500 m, (c) 1000 m, and (d) 1500 m

The diurnal variation of wind speed in the regions of interest in August 2013 was characterized by a bit higher wind speed during the daytime (usually during the day the wind speed exceeded the night values by 4 m/s). The maximum speed is usually observed at 15 UTC and the minimum at 00 UTC. However, these findings on diurnal variation do not apply to situations where regions of interest were exposed to baric formations. The examples for the wind speed and direction daily cycle in August 2013 are presented in Appendix E1 - E4.

3.4 Data analysis for temperature regime - January 2013

Analysis of the Enviro-HIRLAM model output showed that during January 2013, the NWFD of the Russian Federation and the Scandinavian countries were exposed to warm air masses transported from the west. The warmest days were observed during the first part of January (an example is shown in Figure 21), and in the last days of the month. The air temperature at the 1st model level on the Kola Peninsula ranged from -4 up to -12 °C. In the region of Karelia in the southern parts, the temperature was -4...- 8 °C, and in the northern parts -8...-12 °C. For the Leningrad region, it ranged within 0...-4 °C. In the Scandinavian region, a pronounced temperature inversion was noticeable. The temperature over the Barents Sea was 0...4 °C. This is due to the presence of the warm current of the Gulf Stream, and the atmospheric transport of warm air masses from the Atlantic Ocean region. The air temperature over the aquatoria of the White Sea varied from 0 to -8 °C, and the Baltic Sea: -4...4 °C. An inversion was observed in the north of the Scandinavian Peninsula.

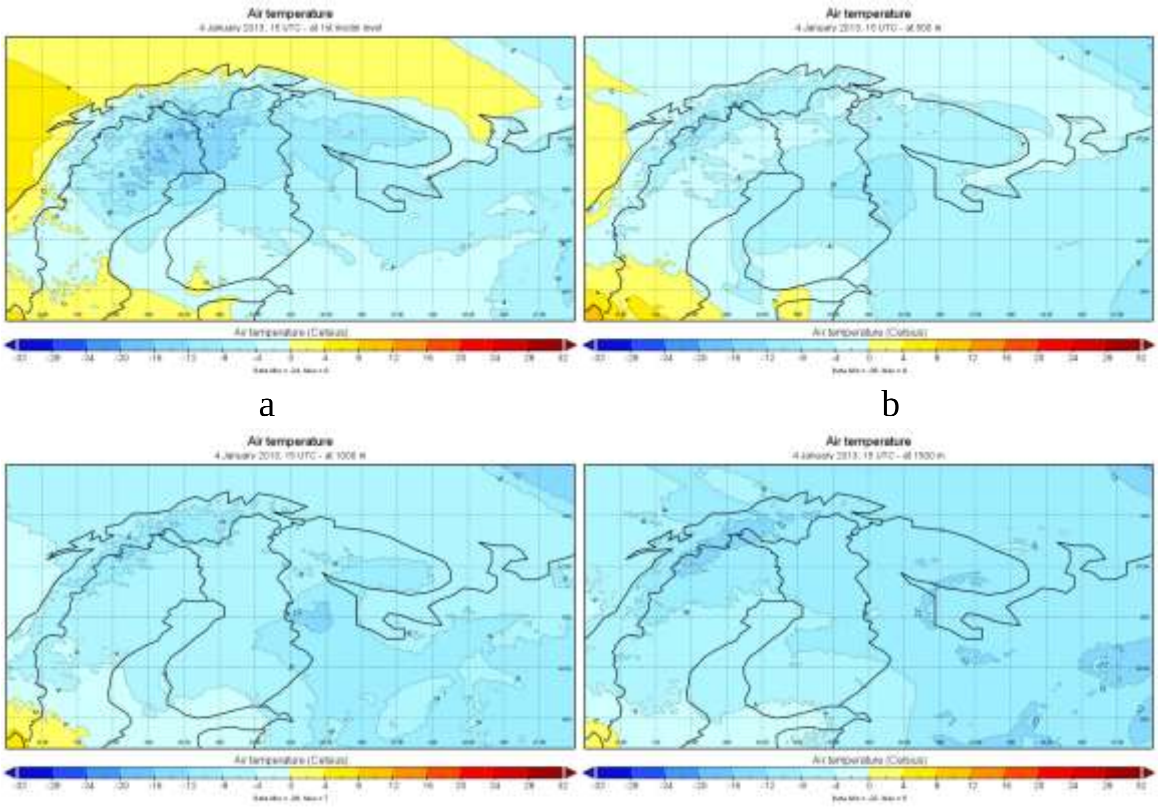

a b

c d

Figure 21. - Spatial variability of the air temperature field on 04.01.2013, 15 UTC at: (a) 1st model level (~32 m), (b) 500 m, (c) 1000 m, (d) 1500 m.

The coldest days were observed in the 3rd decade of January (except for the last days of the decade). An example is shown in Figure 22. The air temperature on the Kola Peninsula varied within -16 ...- 24 °C. In Karelia: -8 ...- 20 °C. In the Leningrad region: -4 ...- 8 °C. The air temperature over the Barents Sea was from -4 to -12 °C. Over the White Sea - from -8 to -16 °C, and over the Baltic Sea - from 0 to -8 °C. In the Scandinavian countries, temperatures ranged from 0 °C (in the southern regions) to -24 °C (in the northern regions).

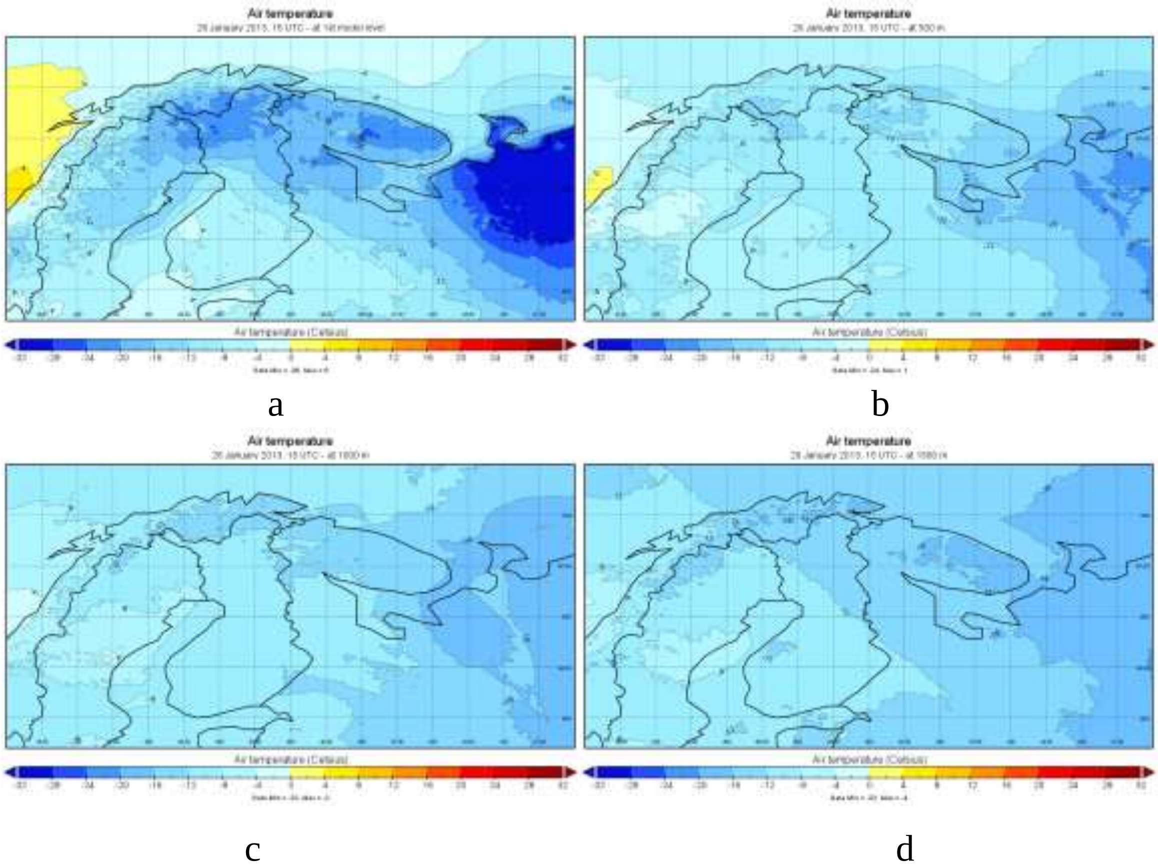

Figure 22. - Spatial variability of the air temperature field on 26.01.2013, 15 UTC at: (a) 1st model level (~32 m), (b) 500 m, (c) 1000 m, and (d) 1500 m.

Also, during these days, the inversion of air temperature was clearly noticeable in Karelia, on the Kola Peninsula, as well as in the northern regions of the Scandinavian countries (Figure 22). The air temperature inversion case for 26 January 2013 was compared with the radio sounding observations (e.g. aerological diagrams extracted from the data repository of the University of Wyoming, USA) at the Kandalaksha station located on the Kola Peninsula (Figure 23). The modeled inversion case was confirmed by the radio sounding data.

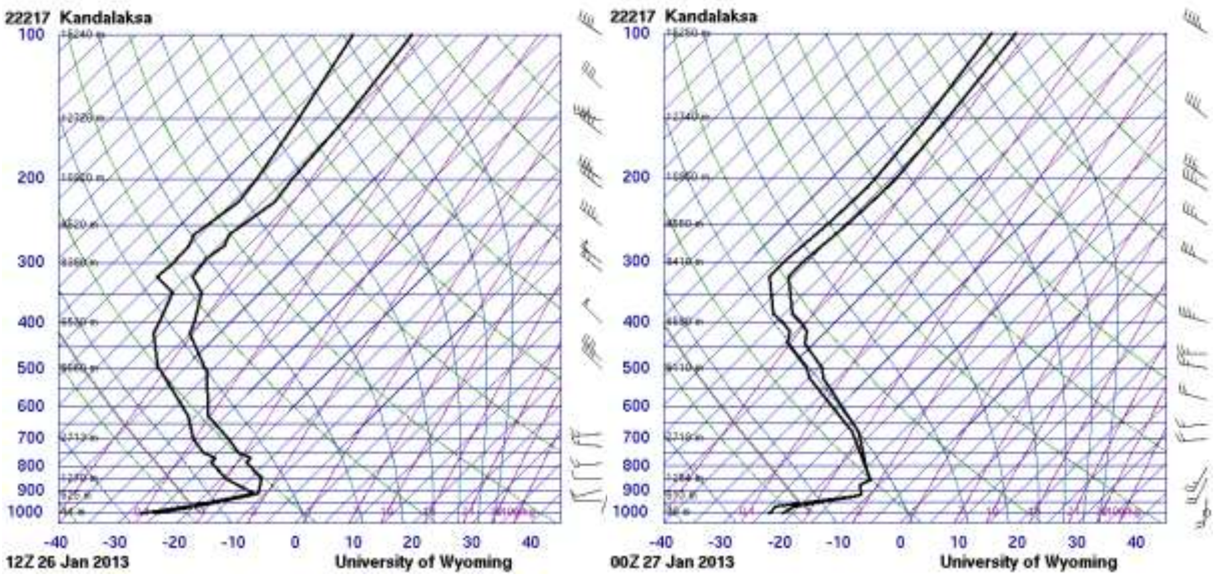

a b

Figure 23 - Aerological diagrams for (a) 26.01.2013, 12 UTC, and (b) 27.01.2013, 00 UTC. [54]

During January, the daily variation of air temperature was not as pronounced as during August. The difference in daytime and nighttime temperatures was insignificant. Surface temperature inversions were observed in all zones of interest both during the day and at night. The example of the air temperature daily cycle for January 2013 is presented in Appendix A5 - A8.

3.5 Data analysis for humidity regime - January 2013

Analysis of the Enviro-HIRLAM model output showed that in the studied area, including certain regions of interest, very intense cloudiness was observed in January throughout the whole month. One of the highest total amounts of the cloudiness was observed in the first decade of the month (Figure 24a), which was associated with the passage of the Icelandic cyclone front. The second time intense cloudiness was observed during the passage of a cyclone front centered on the northwestern coast of Norway (Figure 24b). The third time intense cloudiness was observed during the passage of a cyclone front centered on the western coast of Norway during the second decade of the month. Intense cloudiness was also observed in the third decade of the month and was caused by the influence of a cyclone with a center north of the Kola Peninsula (Figure 24c), and in the 3rd decade - by the passage of a cyclone front with a center west of the coast of Norway (Figure 24d).

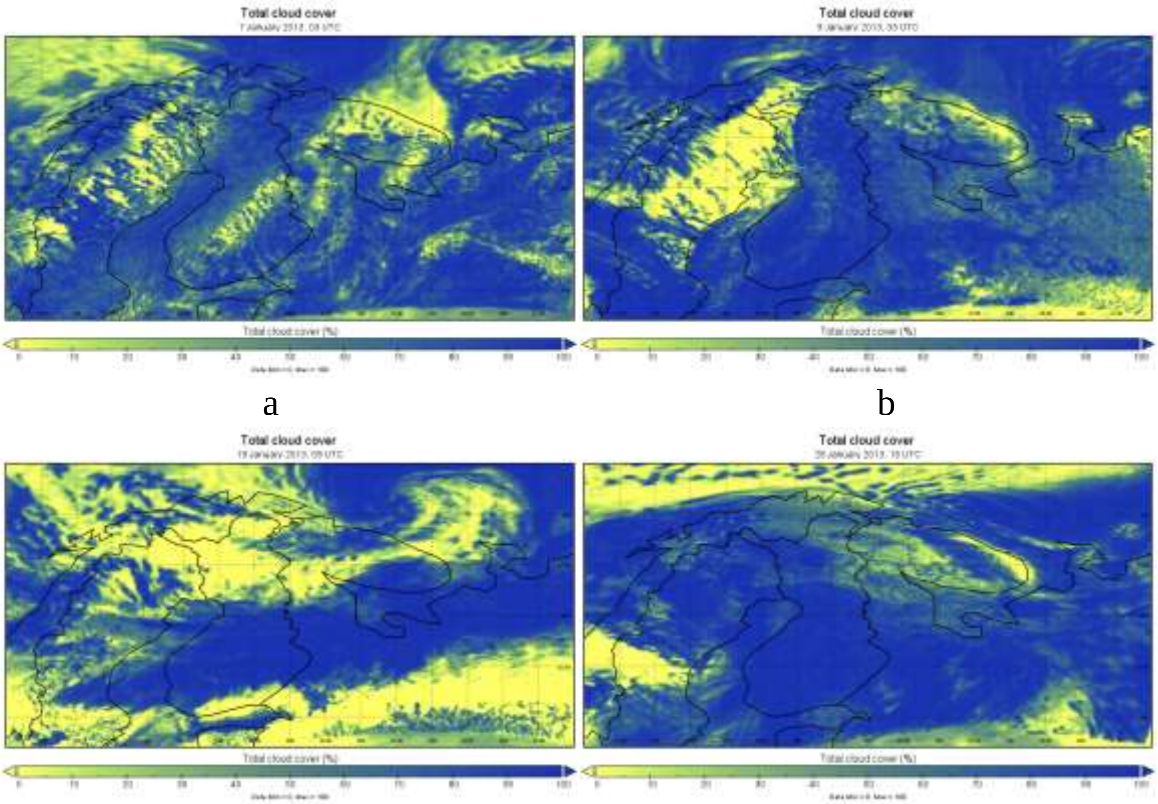

a b

c d

Figure 24. - Spatio-temporal variability of the total cloud cover field: (a) - 07.01.2013, 03 UTC, (b) - 09.0.2013, 03 UTC, (c) - 19.01.2013, 09 UTC, (d) - 28.01.2013, 15 UTC.

Accordingly, such intense cloudiness was accompanied by intensive convective precipitation. Figure 25 shows the most intense precipitation (the dates of precipitation are roughly comparable to the dates of the most intense cloud cover).

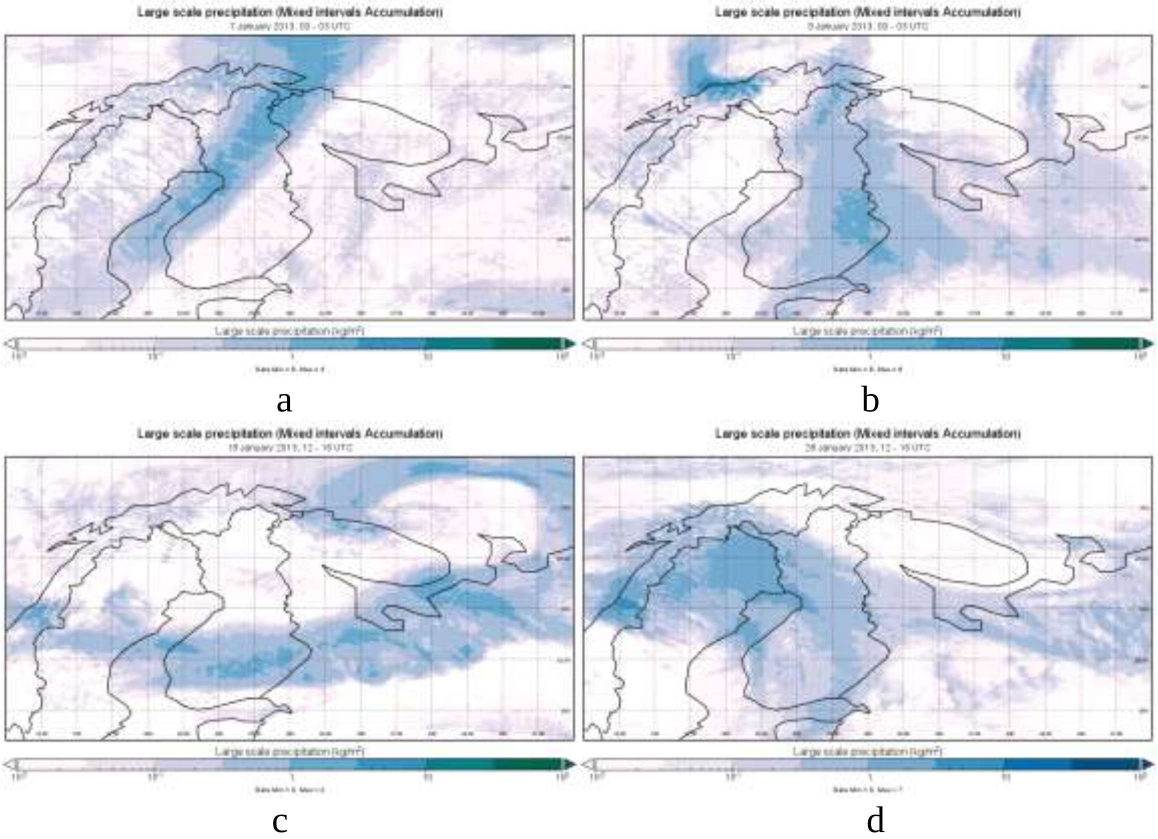

Figure 25. - Spatio-temporal variability of the large - scale precipitation field (accumulated other 3-hour interval) for: (a) 07.01.2013, 00 - 03 UTC, (b) 09.01.2013, 00 - 03 UTC, (c) 19.01.2013, 12 - 15 UTC, and (d) 28.01.2013, 12 - 15 UTC.

In January, the specific humidity was not high. The values did not exceed 0.004 - 0.006 kg / kg. Moist air masses usually arrived from the west and the north (i.e. from the Atlantic Ocean and the Barents Sea areas).

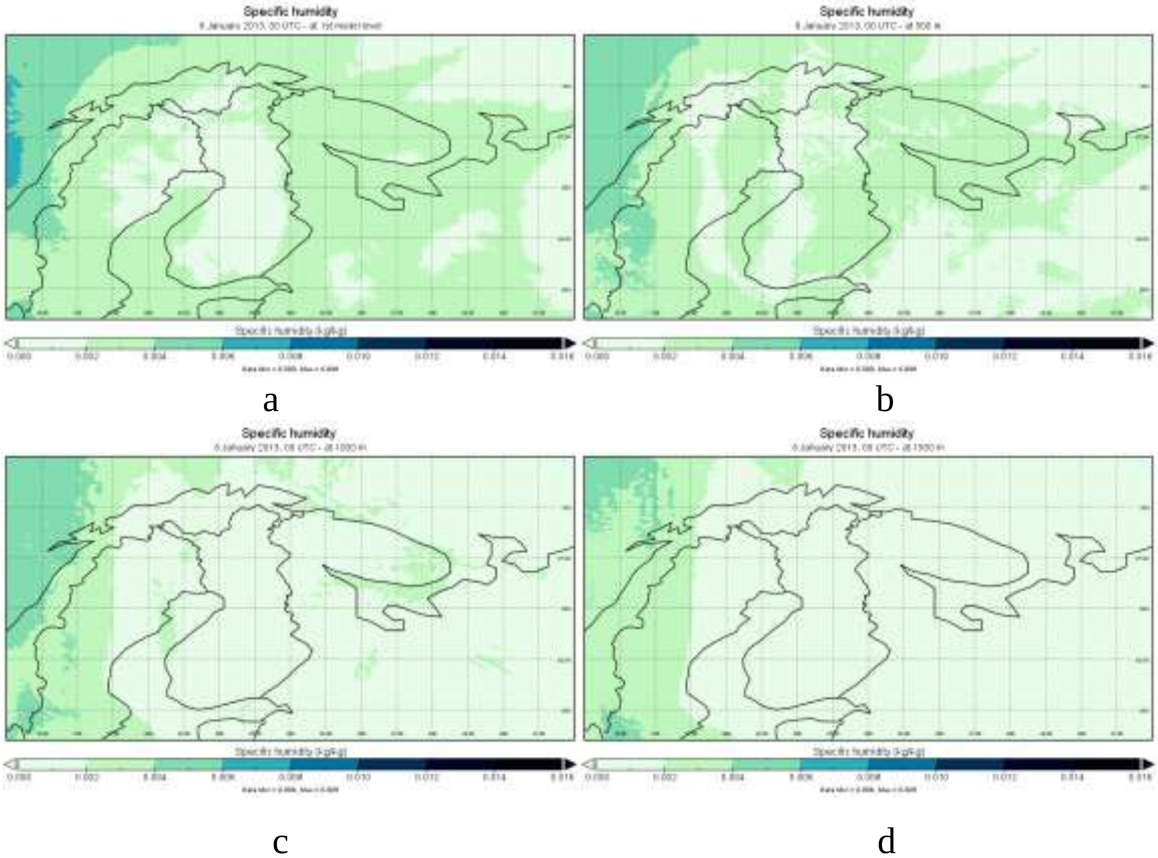

Figure 26. - Spatial variability of the specific humidity field on 18.08.2013, 06 UTC at: (a) 1st model level (~32 m), (b) 500 m, (c) 1000 m, and (d) 1500 m.

The most noticeable intrusions of moist air masses were noted at the beginning (an example is shown in Figure 26) and at the end of the month (Figure 27). Specific humidity with height changed in an expected way (i.e. decreased). Also, at all heights, the spatial boundaries of moist air masses are clearly visible. In January 2013, the parameters of the PBL humidity regime practically did not have a pronounced diurnal variation, and depended on other factors, mainly on the synoptic situation. The examples for specific humidity daily cycle in January 2013 are presented in Appendix D5 - D8; for total cloud cover - in Appendix B2; for large scale precipitation - in Appendix C2.

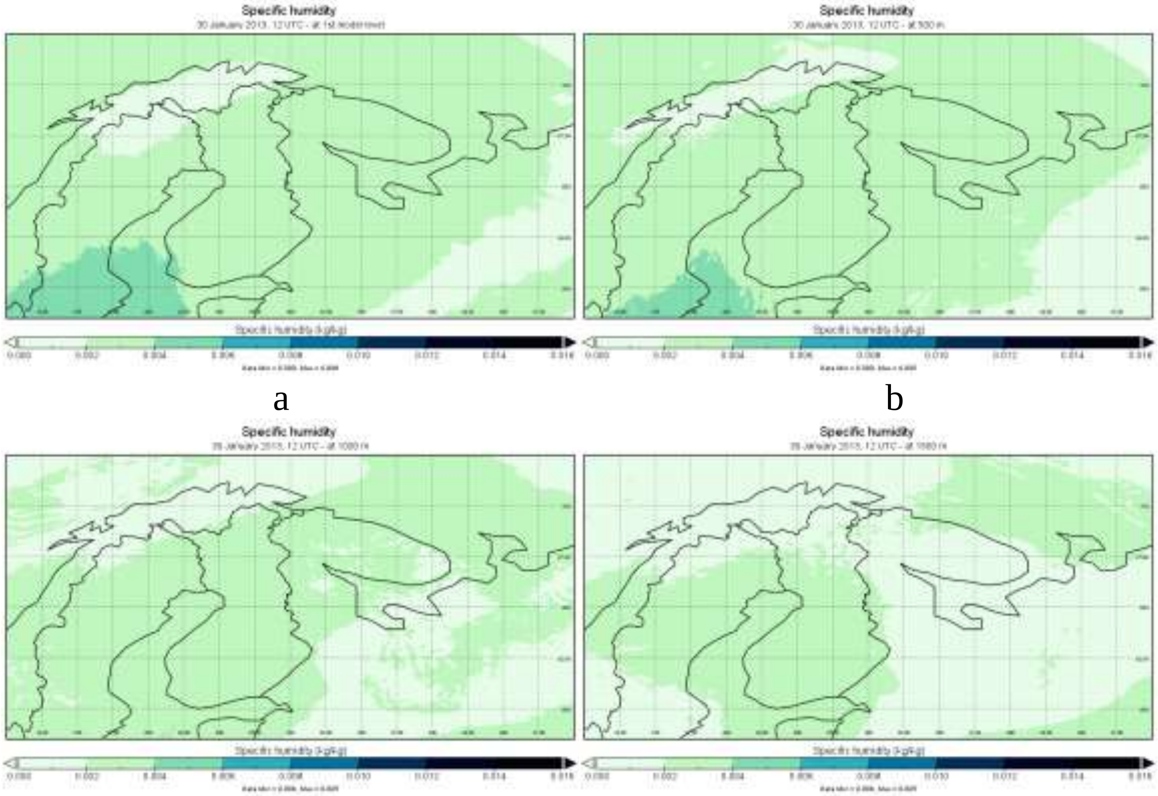

a b

c d

Figure 27. - Spatial variability of specific humidity on 30.01.2013, 06 UTC at: (a) 1st model level (~32 m), (b) 500 m, (c) 1000 m, (d) and 1500 m.

3.6. Data analysis for wind regime - January 2013

Analysis of the Enviro-HIRLAM model output showed that during January the winds from the west and north-west directions prevailed over the study area (an example is shown in Figure 28). The wind speed was quite high, and at a height of 10 meters, it reached 20-24 m/s.

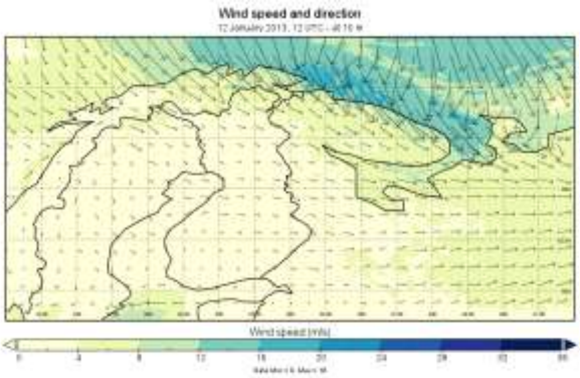

a

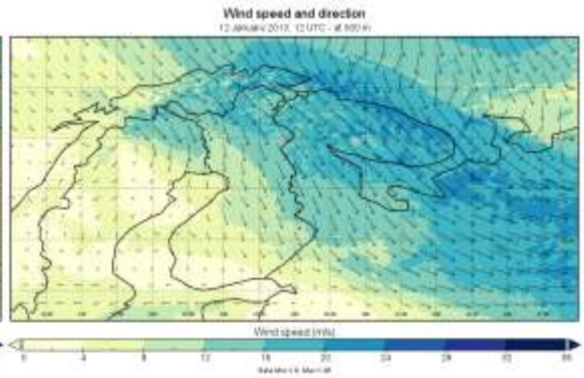

b

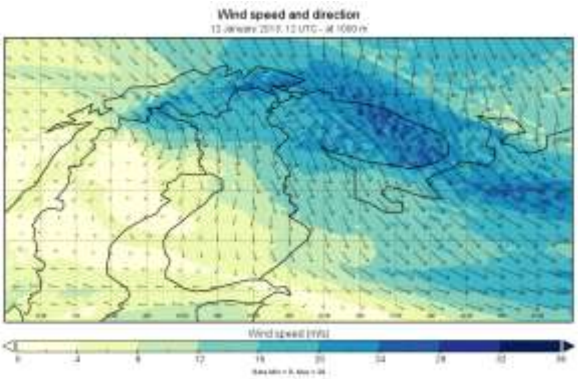

c

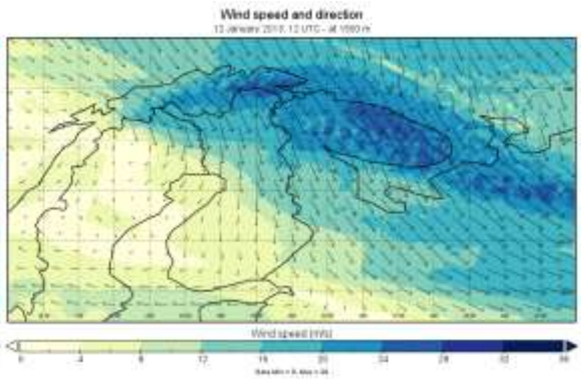

d

Figure 28. - Spatial variability of the wind speed and direction fields on 12.01.2013, 12 UTC at: (a) 10 m, (b) 500 m, (c) 1000 m, and (d) 1500 m

At the end of the month, the wind direction changed to the southwest (Figure 29), bringing warm air masses (See Chapter 3.1). The wind speed at a height of 10 meters was up to 12-16 m/s (over the Barents Sea), and 8-12 m/s (in other areas of interest). With the height, the wind speed changed as expected (i.e. increased). The diurnal variation of wind speed was not well pronounced. Perhaps this is due to the fact that the zones of interest in January were exposed to a very active influence of baric formations (in particular, cyclones), because of which the wind speed often changed sharply regardless of the time of day. The examples for the wind speed and direction daily cycle in January 2013 are presented in Appendix E5 - E8.

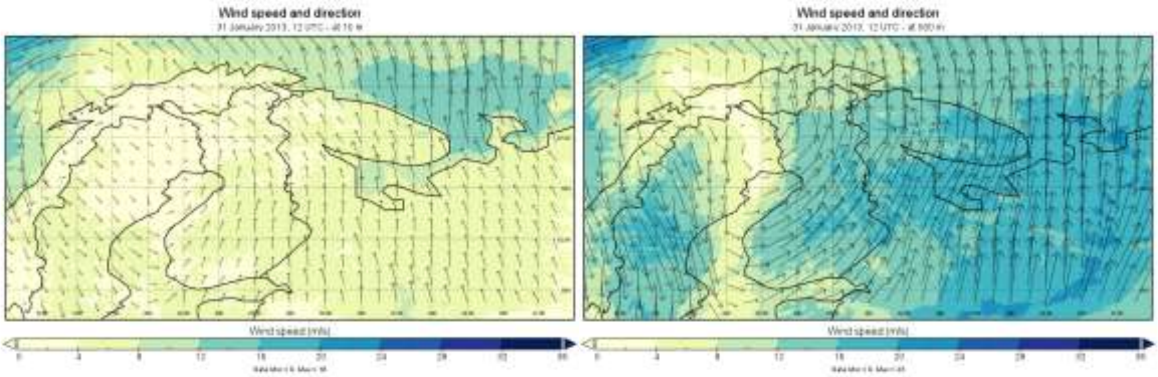

a b

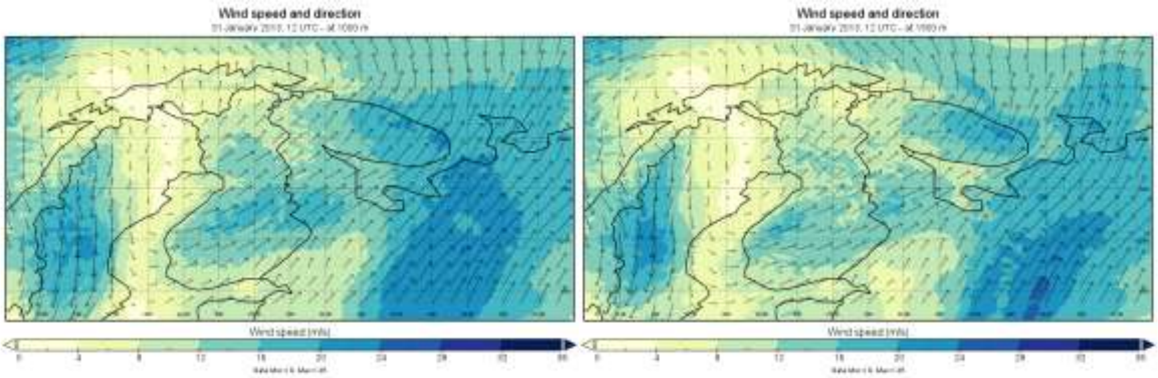

a b

Figure 29. - Spatial variability of the wind speed and direction on 31.01.2013, 12 UTC at: (a) 10 m, (b) 500 m, (c) 1000 m, and (d) 1500 m

4. Conclusions

This diploma work main objective was to evaluate temperature – wind - humidity regimes of the Planetary Boundary Layer (PBL) over land and water surfaces for selected geographical regions of North-West Russia and Nordic countries. To achieve this objective, the following tasks were solved. First of all, the online integrated meteorology-chemistry-aerosols Enviro-HIRLAM modeling system was adapted for the purposes of this work. For that necessary model domain settings and computational technical parameters were set up. All necessary input data (initial and boundary conditions for meteorology and aerosols/chemistry) and emission inventories were extracted and pre-processed. Secondly, unfavorable weather episodes (for warm and cold conditions) in 2021 with evaluated air pollution were selected. In particular, two episodes - (i) August (with increased concentration of sulfur dioxide observed), and (ii) January (with well-pronounced cyclonic influence) - were selected. Thirdly, the model simulations (with direct and indirect aerosols effects included) were performed with selected setup for both months. Finally, visualization (with Panoply software), analysis, and synthesis of the output modeling results were performed in this diploma work.

The findings obtained in this work are the following: The Temperature-Humidity-Wind regimes of PBL were analyzed based on Enviro-HIRLAM model output. Analysis of diurnal cycle (every 3-hour interval) and vertical (at the surface, 500-1000-1500 m above sea level) structure showed strong variability over studied regions during both months – January and August 2013. First of all, the analysis of the temperature regime of the PBL in August 2013 showed that the area of interest was exposed to warm air masses from the south and west. The warmest days were observed at the beginning of the month, the coldest - at the end of the month. Analysis of the diurnal variation of the air temperatures showed that the maximum air temperatures usually reached at 15 UTC, and the minimum - at 03 UTC. As expected, the air temperature decreased with height. The observed elevated air pollution episodes in the cities of Nickel, Svetogorsk, and St. Petersburg (having sources of emissions) may have led to increased air temperatures. In January 2013, the area of interest was exposed to warm air masses from the Atlantic Ocean. The diurnal cycle of the air temperature was not well pronounced. The air temperature inversions were observed up to 1000 m during the month (mainly over the northern regions of North-West Russia and the Scandinavian Peninsula). The majority of inversion events were well modeled and confirmed by radio-sounding data. Secondly, the analysis of the PBL humidity regime in August 2013 showed that the most intense cloudiness and precipitation were observed in the 1st and 2nd decade of the month. Monthly variations in specific humidity showed that the area of interest was influenced by moist air masses from the west and southwest. The diurnal cycle of the specific humidity showed that the maximum values were observed at nighttime (00-03 UTC) and the minimum at daytime (12-15 UTC). In January analysis showed that intense cloudiness and precipitation were observed throughout the month. The area of interest was exposed to moist air masses from the west. The diurnal variation of the specific humidity was practically not well pronounced. Thirdly, analysis of the PBL wind regime in August 2013 showed that the western and southern wind directions prevailed. The highest wind speed was observed when baric formations passed the area of interest. The wind speed decreased with height (as expected). The diurnal variation of the wind speed showed that during the daytime (usually 12-15 UTC) it reached its maximum. At midnight (00 UTC) the wind speed reached its minimum. In January analysis showed that north-west and west wind directions prevailed. At the end of the month, the wind direction changed to the southwest. The wind speed was higher over the water surfaces of the Barents and White seas than over the land surfaces.

5. Applicability of results

The applicability of results are the following: 1) the results obtained can be used for the improvement of numerical weather prediction and chemical weather forecasting, 2) for assessment of pollution impact on environment and population, 3) To assess and investigate the PBL in 2013. The further studies (MSc programme) include the following: 1) more detailed in depth analysis of boundary layer regimes and vertical structure over the regions of interests, 2) impact of aerosol effects on formation and development of cloudiness and precipitation patterns over land and water surfaces, 3) influence of urban areas (on the example of Saint-Petersburg metropolitan area) on formations and development of selected meteorological and atmospheric composition fields.

6. Acknowledgments

For methodological assistance and guidance throughout the entire period of doing this research and writing the presented work, I am very grateful to my scientific supervisor Dr. Aaed Mkhanna (Russian State Hydrometeorological University, RSHU) and scientific consultant Dr. Alexander Mahura (University of Helsinki, Finland). Their consultations, comments, advice, and constructive criticism of the presented work are greatly appreciated.

Also, I would like to especially thank Professor Sergey Smyshlyaev (RSHU) - for providing access to the ECMWF supercomputer and necessary calculation resources as a part of the Enviro-PEEX(Plus) project; Dr. Daniel Santos (HIRLAM-ALADIN Consortium) - for providing access to hirlam.org repository and databases; Dr. Irina Petrova (Ghent University) - for advice about thesis presentation; and Georgy Nerobelov (St. Petersburg State University) - for practical and technical advice. I am grateful to the teaching staff of the RSHU for the well-organized learning process.

Also, I would like to express my thankfulness to my parents for financial support and moral support for years of University education and during the writing of this thesis work.

7. References

1) Tian Zhang, Huizheng Che, Zhiqiang Gong, Yaqiang Wang, Jizhi Wang, Yuanqin Yang, Ke Gui, Bin Guo, The two-way feedback effect between aerosol pollution and planetary boundary layer structure on the explosive rise of PM2.5 after the “Ten Statements of Atmosphere” in Beijing, Science of The Total Environment, Volume 709, 2020, 136259, ISSN 0048-9697.
2) James R. Holton, Gregory J. Hakim, Chapter 8 - The Planetary Boundary Layer, Editor(s): James R. Holton, Gregory J. Hakim, An Introduction to Dynamic Meteorology (Fifth Edition), Academic Press, 2013, Pages 255-277, ISBN 9780123848666.
3) Sikora, T. & Ufermann, S. (2004). Marine Atmospheric Boundary Layer Cellular Convection and Longitudinal Roll Vortices, Pages 321 – 327.
4) Sjöblom, Anna. (2002). Turbulent Structure of the Marine Atmospheric Boundary Layer and its Implications for the Inertial Dissipation Method, Pages 5 – 7.
5) Л. С. Гандин, Д. Л. Лайхтман, Л. Т. Матвеев, М. И. Юдин. ОСНОВЫ ДИНАМИЧЕСКОЙ МЕТЕОРОЛОГИИ, Ленинград Гидрометеорологическое издательство, 1955, Pages 346 – 351, 569 – 571.
6) Weiguo Wang, Kenneth J. Davis, Bruce D. Cook, Peter S. Bakwin, Chuixiang Yi, Martha P. Butler, Daniel M. Ricciuto, Surface layer CO2 budget and advective contributions to measurements of net ecosystem–atmosphere exchange of CO2, Agricultural and Forest Meteorology, Volume 135, Issues 1–4, 2005, Pages 202-214, ISSN 0168-1923.
7) Sommerfeld, Arnold (1908). "Ein Beitrag zur hydrodynamischen Erkläerung der turbulenten Flüssigkeitsbewegüngen (A Contribution to Hydrodynamic Explanation of Turbulent Fluid Motions)”. International Congress of Mathematicians . 3: 116–124.

8) Л. Т. Матвеев. Курс общей метеорологии, Физика атмосферы, издание второе переработанное и дополненное, Ленинград, Гидрометиздат, 1984. Pages 212 – 127, 242 – 251, 331 – 335, 594 – 598, 560 – 565.
9) P.M. Quinn, J.A. Cherry, B.L. Parker, Relationship between the critical Reynolds number and aperture for flow through single fractures: Evidence from published laboratory studies, Journal of Hydrology, Volume 581, 2020, 124384, ISSN 0022-1694.
10) Hunt, J.C.R. (1998). "LEWIS FRY RICHARDSON AND HIS CONTRIBUTIONS TO MATHEMATICS, METEOROLOGY, AND MODELS OF CONFLICT". Annual Review of Fluid Mechanics. 30 (1): xiii–xxxvi. 30.1.0. ISSN 0066-4189.
11) Kern E. Kenyon, Diurnal variation of air temperature across the north pacific, Atmospheric Research, Volume 22, Issue 4, 1989, Pages 285-295, ISSN 0169-8095.
12) J.M. Wallace, D.W.J. Thompson, P. Beresford, GENERAL CIRCULATION OF THE ATMOSPHERE | Overview, Editor(s): Gerald R. North, John Pyle, Fuqing Zhang, Encyclopedia of Atmospheric Sciences (Second Edition), Academic Press, 2015, Pages 33-42, ISBN 9780123822253.
13) Vasileios Salamalikis, Ioannis Vamvakas, Christian A. Gueymard, Andreas Kazantzidis, Atmospheric water vapor radiative effects on shortwave radiation under clear skies: A global spatiotemporal analysis, Atmospheric Research, Volume 251, 2021, 105418, ISSN 0169-8095.
14) Resolution of the Chief State Sanitary Doctor of the Russian Federation of December 22, 2017 N 165 G.S.
15) Nyashina, G.V. Kuznetsov, P.A. Strizhak, Effects of plant additives on the concentration of sulfur and nitrogen oxides in the combustion products of coal-water slurries containing petrochemicals, Environmental Pollution, Volume 258, 2020, 113682, ISSN 0269-7491.
16) Justyna Likus-Cieślik, Jarosław Socha, Piotr Gruba, Marcin Pietrzykowski, The current state of environmental pollution with sulfur dioxide (SO2) in Poland based on sulfur concentration in Scots pine needles, Environmental Pollution, Volume 258, 2020, 113559, ISSN 0269-7491.

17) Kan, H., Wong, C. M., Vichit-Vadakan, N., Qian, Z., & PAPA Project Teams (2010). Short-term association between sulfur dioxide and daily mortality: the Public Health and Air Pollution in Asia (PAPA) study. Environmental research, 110(3), 258–264.

18) Internet source: https://www.metoffice.gov.uk/

19) Internet source: https://www.wetterzentrale.de/en/default.php

20) Lawrence, Thomas & Malhotra, Namrata & Morris, Tim. (2012). Episodic and Systemic Power in the Transformation of Professional Service Firms. Journal of Management Studies. 49. 10.1111/j.1467-6486.2011.01031.x.

21) Baklanov, A.: Numerical Modelling in Mine Aerodynamics, USSR Academy of Science, Apatity, 200 pp., 1988 (in Russian).

22) K. Heinke Schlünzen, Silke Pahl, Modification of dry deposition in a developing sea-breeze circulation—A numerical case study, Atmospheric Environment. Part A. General Topics, Volume 26, Issue 1, 1992, Pages 51-61, ISSN 0960-1686.

23) Jacobson, M. Z.: Developing, coupling, and applying a gas, aerosol, transport, and radiation model to study urban and regional air pollution, PhD Dissertation, Dept. of Atmospheric Sciences, UCLA, 436 pp., 1994.

24) Jacobson, M. Z.: Studying the effects of calcium and magnesium on size-distributed nitrate and ammonium with EQUISOLV II, Atmos. Environ., 33, 3635–3649.

25) Jacobson, M. Z.: Control of fossil-fuel particulate black carbon plus organic matter, possibly the most effective method of slowing global warming, J. Geophys. Res., 107, 4410.

26) de Grandpré, J., Beagley, S. R., Fomichev, V. I., Griffioen, E., McConnell, J. C., Medvedev, A. S., and Shepherd, T. G.: Ozone climatology using interactive chemistry: Results from the Canadian Middle Atmosphere Model, J. Geophys. Res.-Atmos., 105, 26475–26491.

27) Austin, J. and Butchart, N.: Coupled chemistry-climate model simulations for the period 1980 to 2020: Ozone depletion and the start of ozone recovery, Q. J. Roy. Meteor. Soc., 129, 3225–3249.

28) Mahura, Alexander & Nuterman, Roman & González-Aparicio, Iratxe & Amstrup, Bjarne & Yang, Xiaohua & Baklanov, Alexander. (2016). Meteorological and Chemical Urban Scale Modelling for Shanghai Metropolitan Area. 10.13140/RG.2.2.33930.88002.
29) Mahura A., Amstrup, B., Nuterman, R., Yang, X., and Baklanov, A.: Multi-Scale Enviro-HIRLAM Forecasting of Weather and Atmospheric Composition over China and its Megacities, Geophys. Res. Abstr., 19, EGU2017-9564, EGU General Assembly 2017.
30) Rasmussen, S. & Andersen, Katrine & Svensson, Anders & Steffensen, J. & Vinther, Bo & Clausen, H.B. & Siggaard-Andersen, M.-L & Johnsen, S.J. & Larsen, Louise Bjoern & Dahl-Jensen, Dorthe & Bigler, M. & Röthlisberger, Regine. (2006). A new Greenland ice core chronology for the Last Glacial termination. Journal of Geophysical Research. 111. 10.1029/2005JD006079.
31) Mahura, A., Baklanov, A., Rasmussen, A., Korsholm, U., and Petersen, C.: Birch pollen forecasting for Denmark, in: Abstracts of 6th Annual Meeting of European Meteorological Society (EMS), vol. 3, EMS2006-A-00495, 3–7 September, Ljubljana, Slovenia, 2006b.
32) Internet source http://hirlam.org/index.php/documentation/chemistry-branch
33) WMO-COST: Joint Report of COST Action 728 and GURME – Overview of Existing Integrated (off-line and on-line) Mesoscale Meteorological and Chemical Transport Modelling Systems in Europe (WMO TD No. 1427), GAW report 177, 106 pp., May 2008.
34) Chenevez, J., Baklanov, A., and Sørensen, J. H.: Pollutant transport schemes integrated in a numerical weather prediction model: model description and verification results, Meteorol. Appl., 11, 265–275.
35) Korsholm, U. S., Baklanov, A., Gross, A., Mahura, A., Sass, B. H., and Kaas, E.: Online coupled chemical weather forecasting based on HIRLAM – overview and prospective of Enviro-HIRLAM, HIRLAM Newsletter, 54, 151–168, 2008.

36) Korsholm, U. S.: Integrated modeling of aerosol indirect effects, Ph.D. thesis, University of Copenhagen, Niels Bohr Institute and Danish Meteorological Institute, Copenhagen, Denmark, 2009.
37) Baklanov, A.: Modelling of formation and dynamics of radioactive aerosols in the atmosphere, in: Research on a Theory of Elementary Particles and Solid State, 4, 135–148, 2003.
38) Gross, A. and Baklanov, A.: Modelling the influence of dimethyl sulfide on aerosol production in the marine boundary layer, Int. J. Environ. Pollut., 22, 51–71.
39) Kaas, E.: A simple and efficient locally mass conserving semiLagrangian transport scheme, Tellus A, 60, 305–320, 2008.
40) Sørensen, B.: New mass conserving multi-tracer efficient transport schemes focusing on semi-Lagrangian and Lagrangian methods for online integration with chemistry, PhD thesis, University of Copenhagen, Niels Bohr Institute and Danish Meteorological Institute, Copenhagen, Denmark, 2012.
41) Sørensen, B., Kaas, E., and Korsholm, U. S.: A mass-conserving and multi-tracer efficient transport scheme in the online integrated Enviro-HIRLAM model, Geosci. Model Dev., 6, 1029– 1042.
42) Feichter, J., Kjellström, E., Rodhe, H., Dentener, F., Lelieveldi, J., and Roelofs, G.-J.: Simulation of the tropospheric sulfur cycle in a global climate model, Atmos. Environ., 30, 1693–1707.
43) Horowitz, L. W., Walters, S., Mauzerall, D. L., Emmons, L. K., Rasch, P. J., Granier, C., Tie, X., Lamarque, J.-F., Schultz, M. G., Tyndall, G. S., Orlando, J. J., and Brasseur, G. P.: A global simulation of tropospheric ozone and related tracers: Description and evaluation of MOZART, version 2, J. Geophys. Res.-Atmos., 108, 4784.
44) Vignati, E., Wilson, J., and Stier, P. (2004), M7: An efficient size-resolved aerosol microphysics module for large-scale aerosol transport models, J. Geophys. Res., 109, D22202, doi:10.1029/2003JD004485.
45) Baklanov, A., Smith Korsholm, U., Nuterman, R., Mahura, A., Nielsen, K. P., Sass, B. H., Rasmussen, A., Zakey, A., Kaas, E., Kurganskiy, A., Sørensen, B., and

González-Aparicio, I.: Enviro-HIRLAM online integrated meteorology–chemistry modelling system: strategy, methodology, developments and applications (v7.2), Geosci. Model Dev., 10, 2971–2999.

46) Manual on Codes - International Codes, Volume I.2, Annex II to the WMO Technical Regulations: Part B – Binary Codes, Part C – Common Features to Binary and Alphanumeric Codes, 2020 (2019 edition).

47) Kuenen, J. J. P., Visschedijk, A. J. H., Jozwicka, M., and Denier van der Gon, H. A. C.: TNO-MACC_II emission inventory; a multi-year (2003–2009) consistent high-resolution European emission inventory for air quality modelling, Atmos. Chem. Phys., 14, 10963–10976.

48) Kuenen, J., Denier van der Gon, H., Visschedijk, A., van der Brugh, H., Finardi, S., Radice, P., d’Allura, A., Beevers, S., Theloke, J., Uzbasich, M., Honoré, C., and Perrussel, O.: MEGAPOLI European Gridded Emission Inventory (Final Version), MEGAPOLI Project Scientific Report, Tech. Rep. 10–17, TNO Built Environment and Geosciences, 2010.

49) Zakey, Sahar & Giorgi, F. & Bi, Xunqiang. (2008). Modeling of sea salt in a regional climate model: Fluxes and radiative forcing. Journal of Geophysical Research. 113. 10.1029/2007JD009209.

50) Internet source: https://is4fires.fmi.fi/

51) Sofiev, M., Ermakova, T., and Vankevich, R.: Evaluation of the smoke-injection height from wild-land fires using remote-sensing data, Atmos. Chem. Phys., 12, 1995–2006.

52) Internet source: http://www.iiasa.ac.at/web/home/research/researchPrograms/air/ECLIPSEv5a.htm

53) Mahura, Alexander & Sattler, K. & Petersen, Claus & Amstrup, Bjarne & Baklanov, Alexander. (2005). DMI-HIRLAM modelling with high resolution setup and simulations for areas of Denmark. DMI Technical Report.

54) Internet source: http://weather.uwyo.edu/upperair/sounding.html

Appendix A1

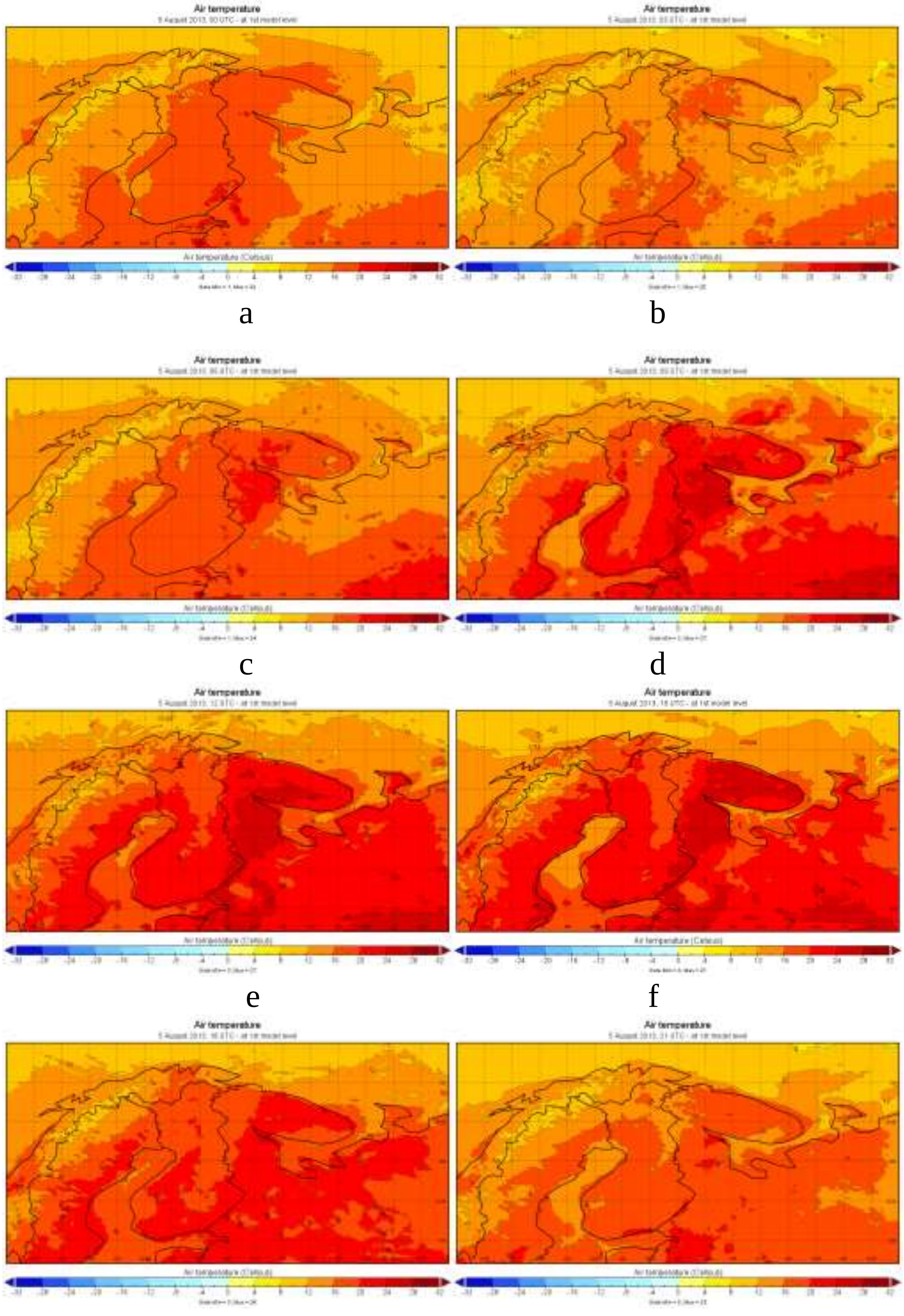

Diurnal cycle of air temperature 05.08.2013 at 1 model level (32 m~): (a) 00 UTC, (b) 03 UTC, (c) 06 UTC, (d) 09 UTC, (e) 12 UTC, (f) 15 UTC, (h) 18 UTC, and (g) 21 UTC.

Appendix A2

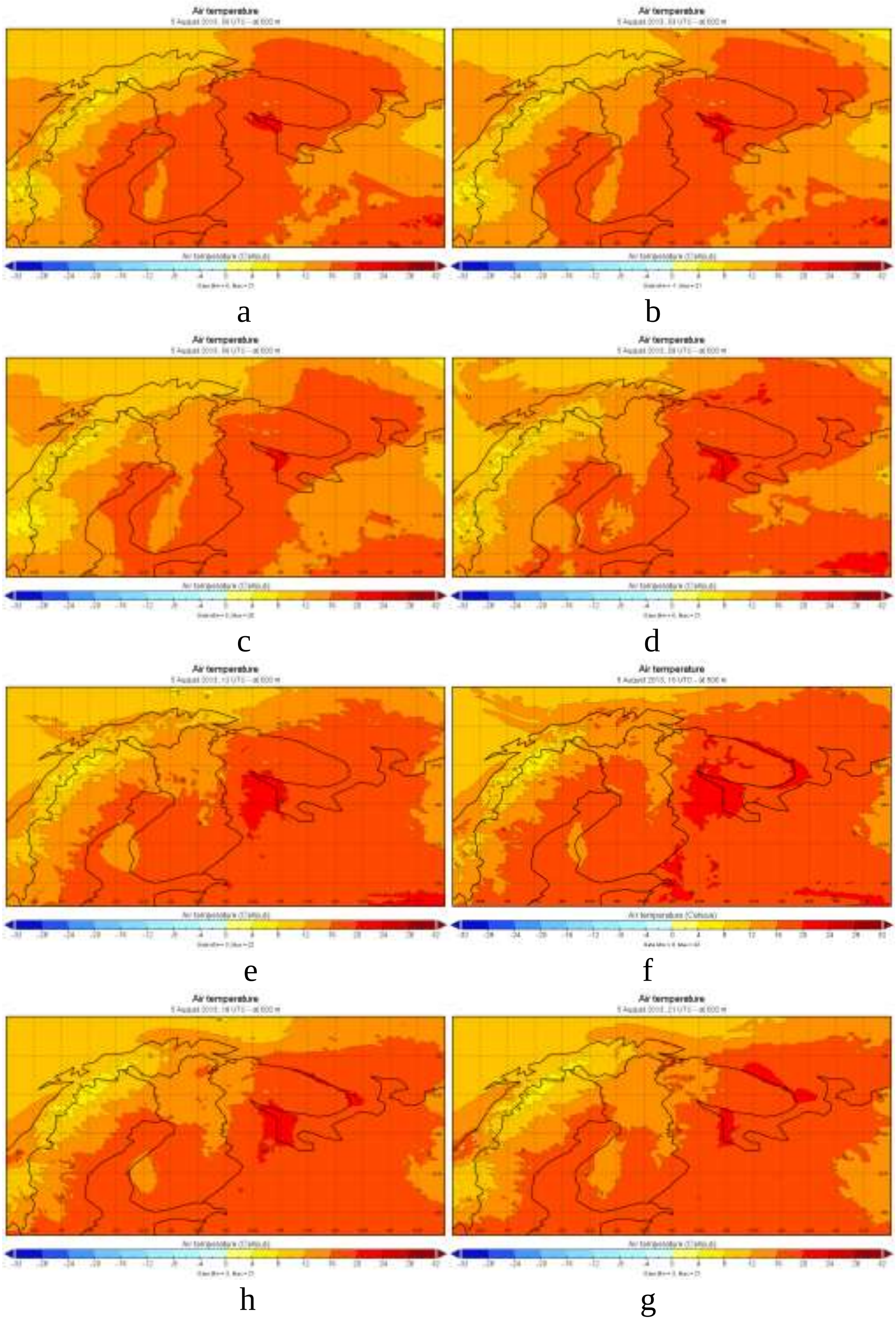

Diurnal cycle of air temperature 05.08.2013 at 500 m: (a) 00 UTC, (b) 03 UTC, (c) 06 UTC, (d) 09 UTC, (e) 12 UTC, (f) 15 UTC, (h) 18 UTC, and (g) 21 UTC.

Appendix A3

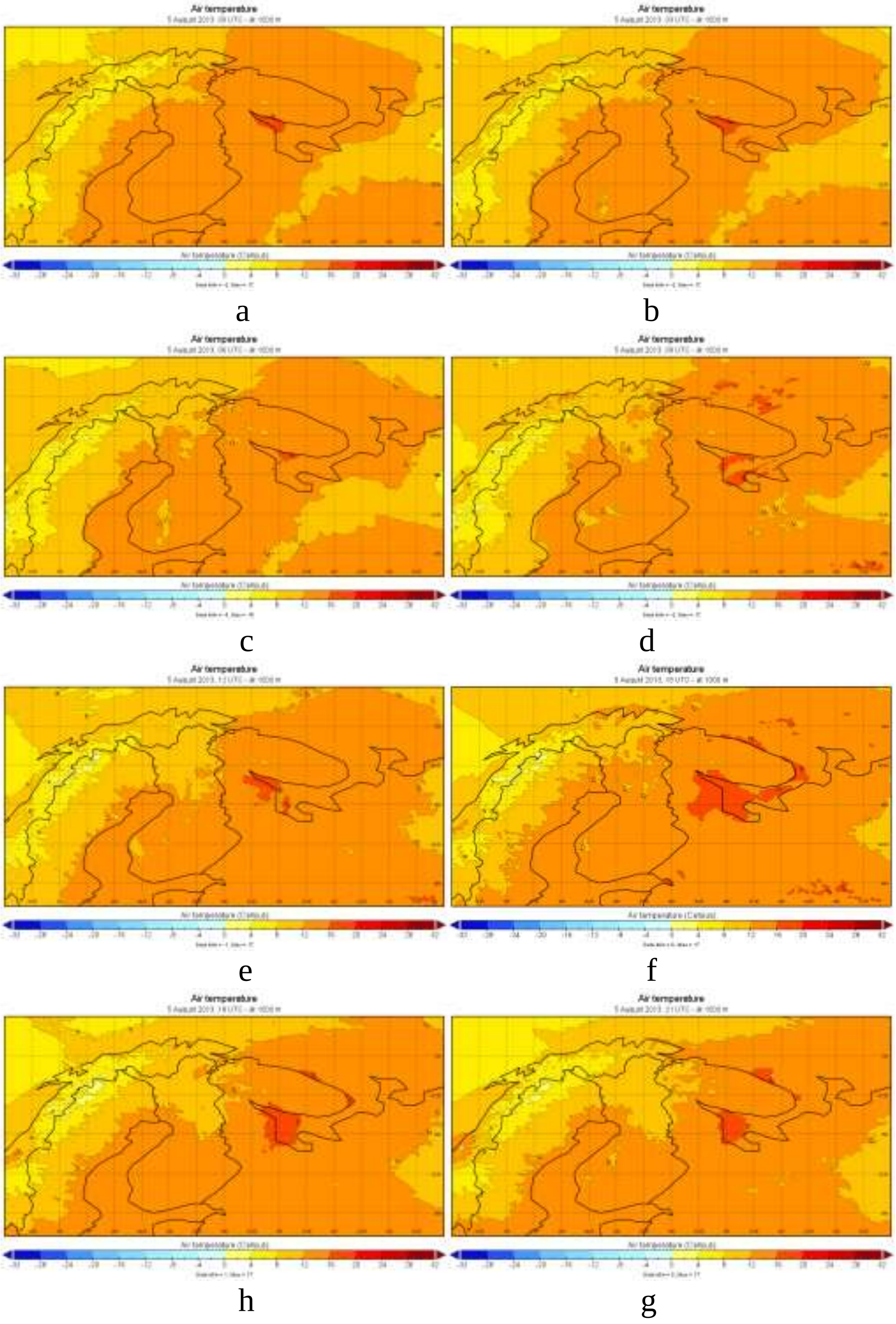

Diurnal cycle of air temperature 05.08.2013 at 1000 m: (a) 00 UTC, (b) 03 UTC, (c) 06 UTC, (d) 09 UTC, (e) 12 UTC, (f) 15 UTC, (h) 18 UTC, and (g) 21 UTC.

Appendix A4

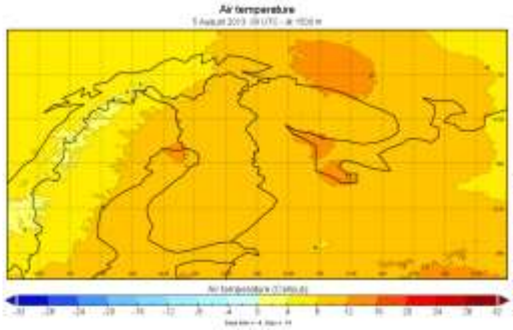
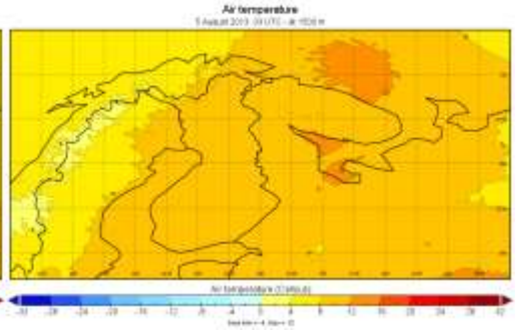

a b

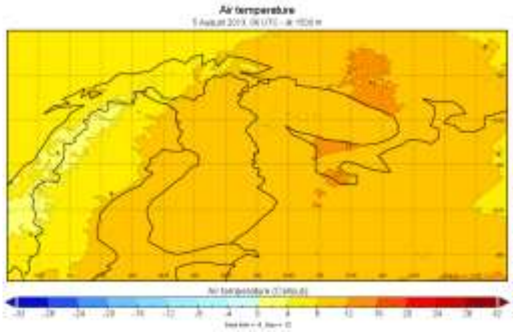
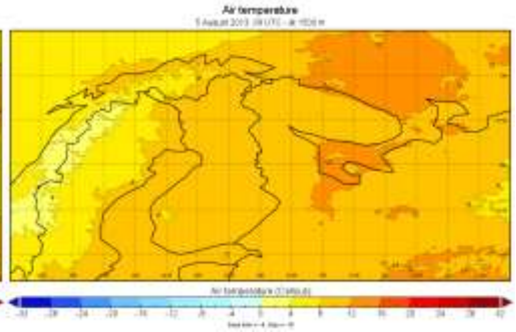

c d

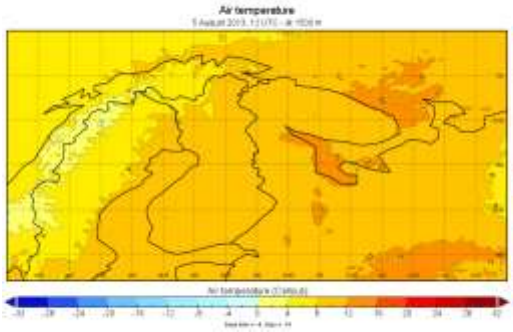
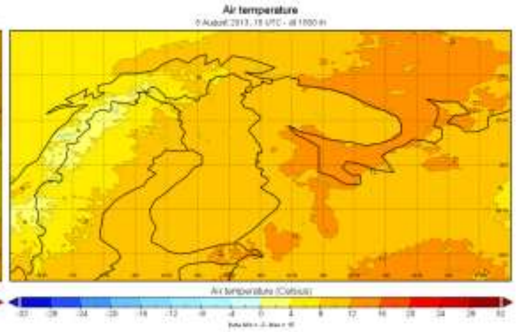

e f

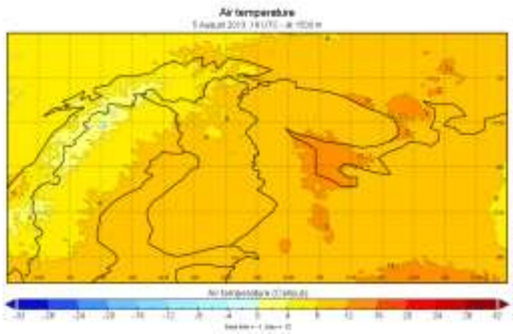
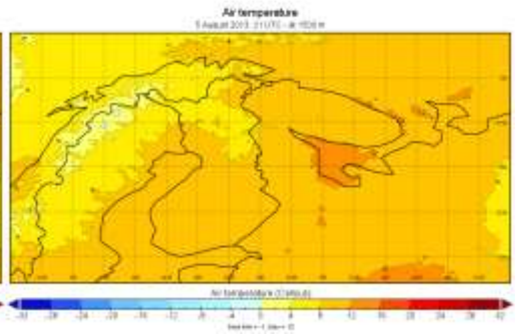

h g

Diurnal cycle of air temperature 05.08.2013 at 1000 m: (a) 00 UTC, (b) 03 UTC, (c) 06 UTC, (d) 09 UTC, (e) 12 UTC, (f) 15 UTC, (h) 18 UTC, and (g) 21 UTC.

Appendix A5

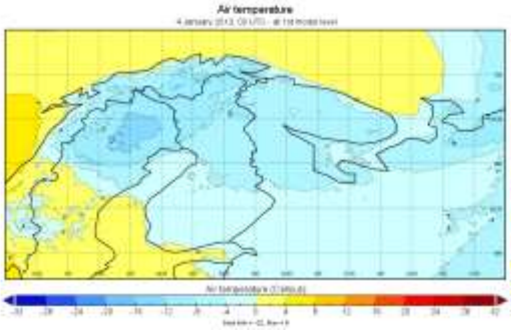

a

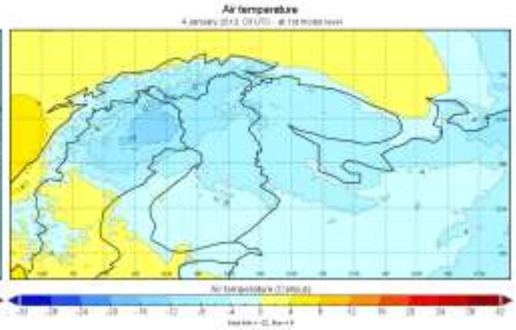

b

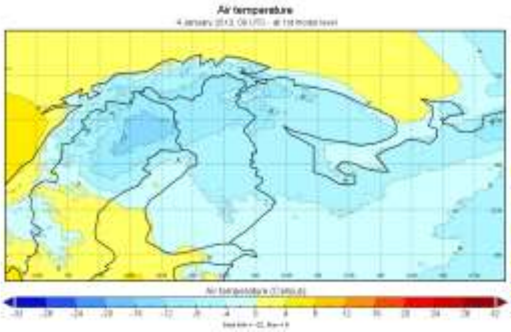

c

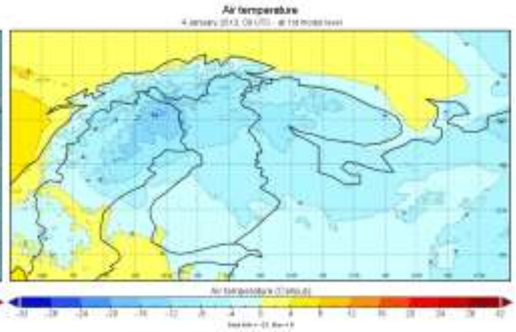

d

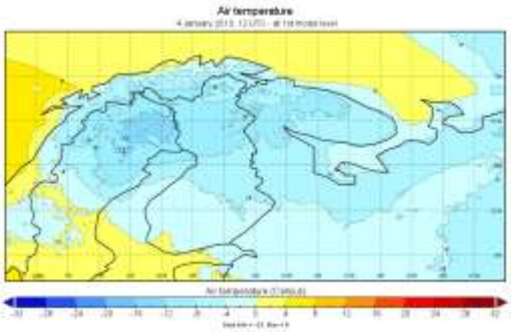

e

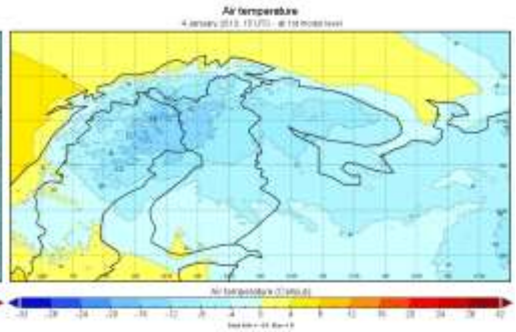

f

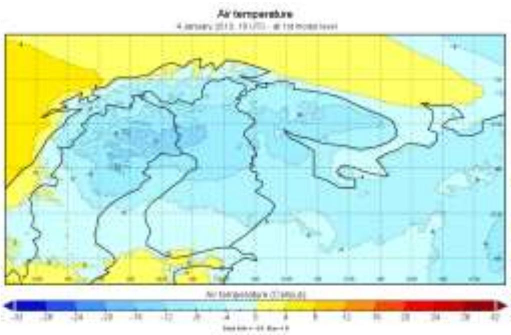

h

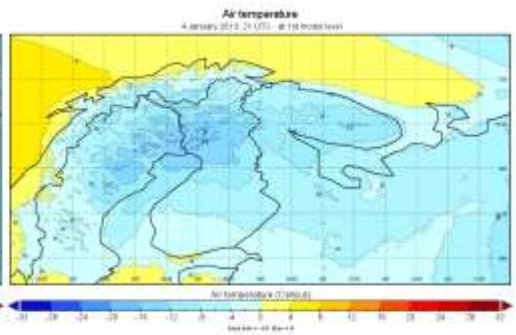

g

Diurnal cycle of air temperature 04.01.2013 at 1st model level: (a) 00 UTC, (b) 03 UTC, (c) 06 UTC, (d) 09 UTC, (e) 12 UTC, (f) 15 UTC, (h) 18 UTC, and (g) 21 UTC.

Appendix A6

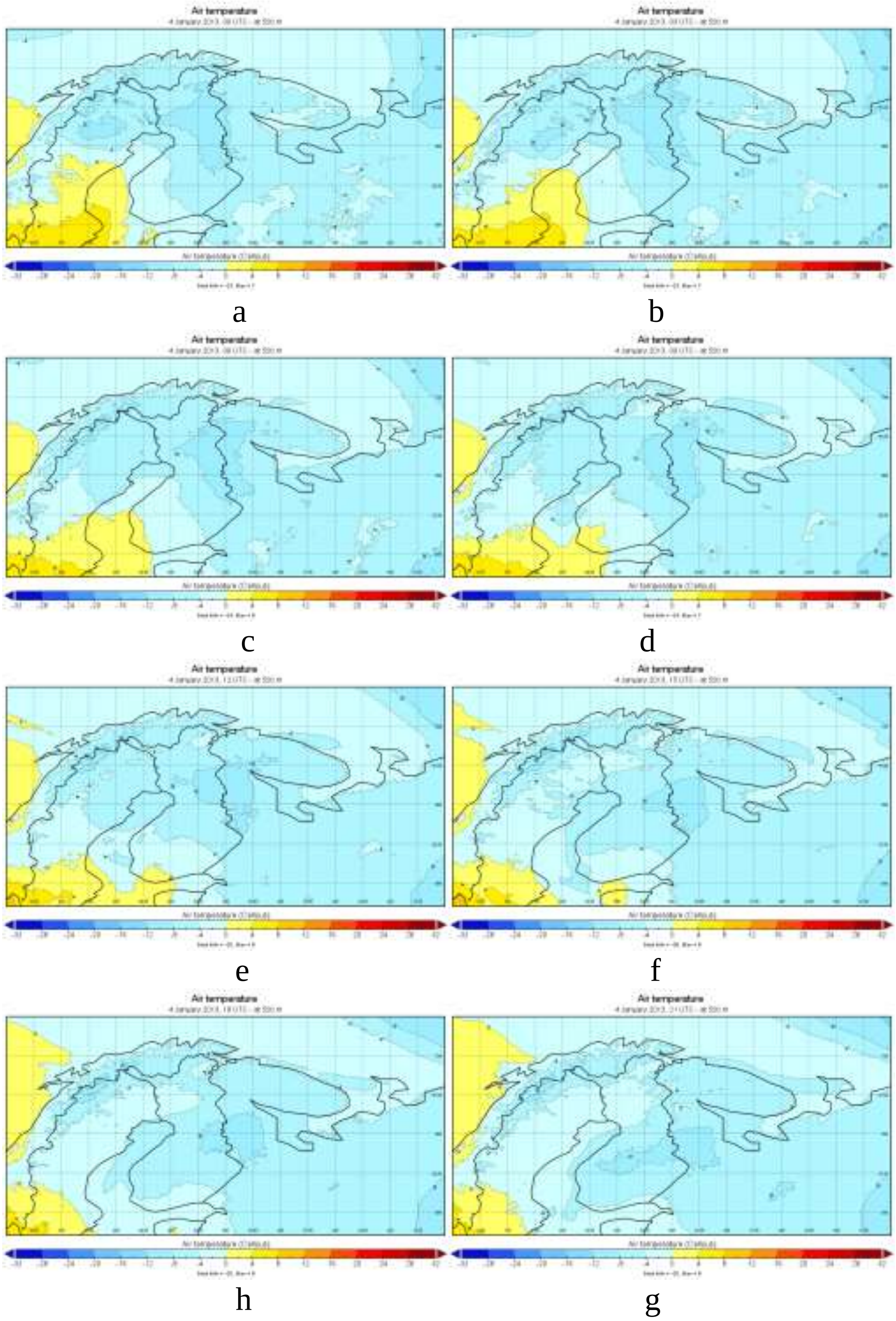

Diurnal cycle of air temperature 04.01.2013 at 500 m: (a) 00 UTC, (b) 03 UTC, (c) 06 UTC, (d) 09 UTC, (e) 12 UTC, (f) 15 UTC, (h) 18 UTC, and (g) 21 UTC.

Appendix A7

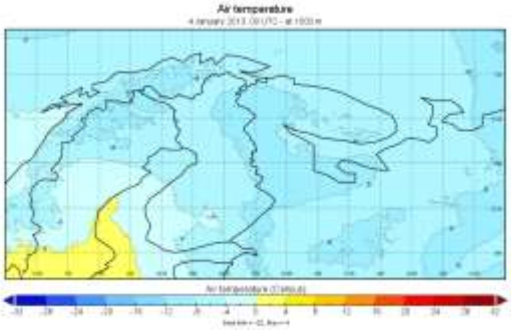

a

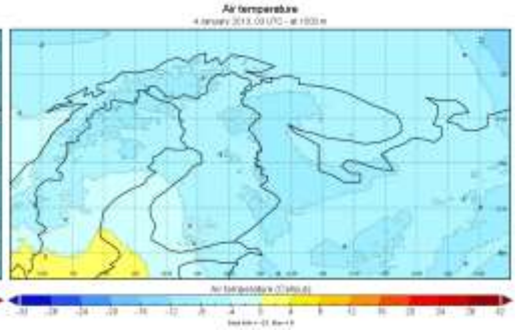

b

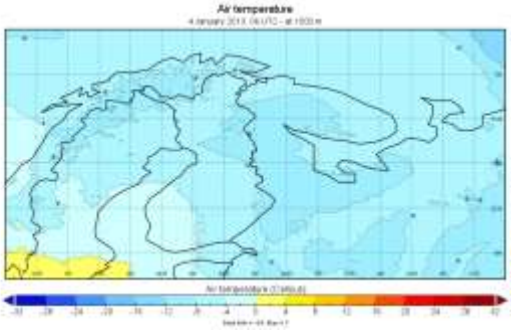

c

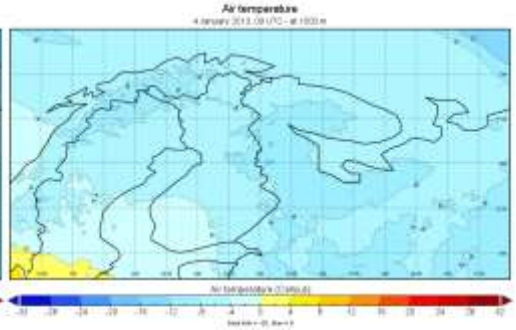

d

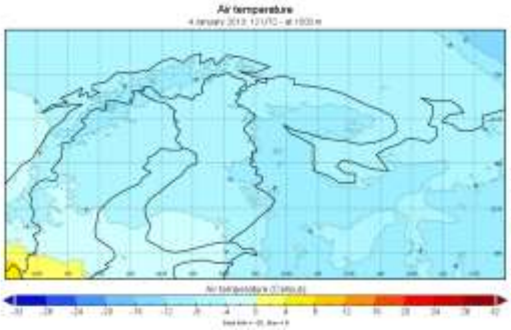

e

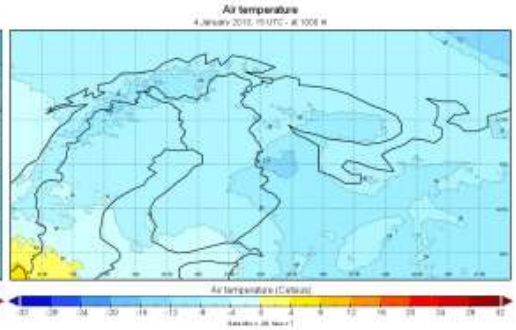

f

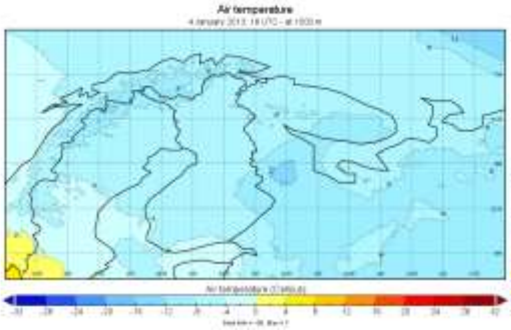

h

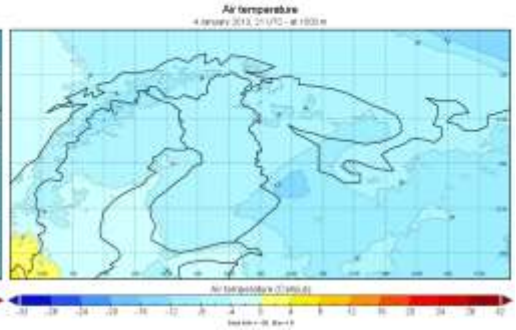

g

Diurnal cycle of air temperature 04.01.2013 at 1000 m: (a) 00 UTC, (b) 03 UTC, (c) 06 UTC, (d) 09 UTC, (e) 12 UTC, (f) 15 UTC, (h) 18 UTC, and (g) 21 UTC.

Appendix A8

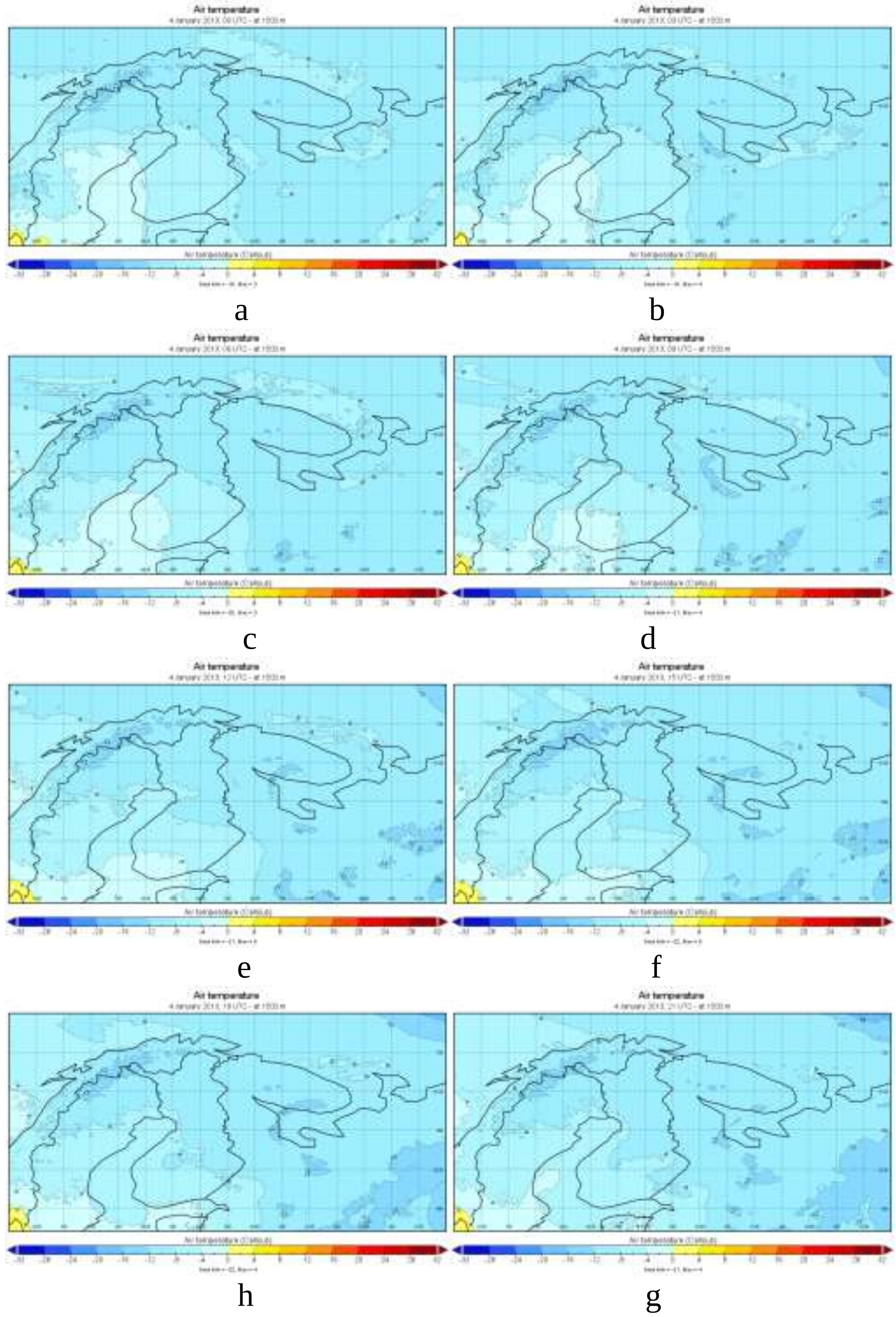

Diurnal cycle of air temperature 04.01.2013 at 1500 m: (a) 00 UTC, (b) 03 UTC, (c) 06 UTC, (d) 09 UTC, (e) 12 UTC, (f) 15 UTC, (h) 18 UTC, and (g) 21 UTC.

Appendix B1

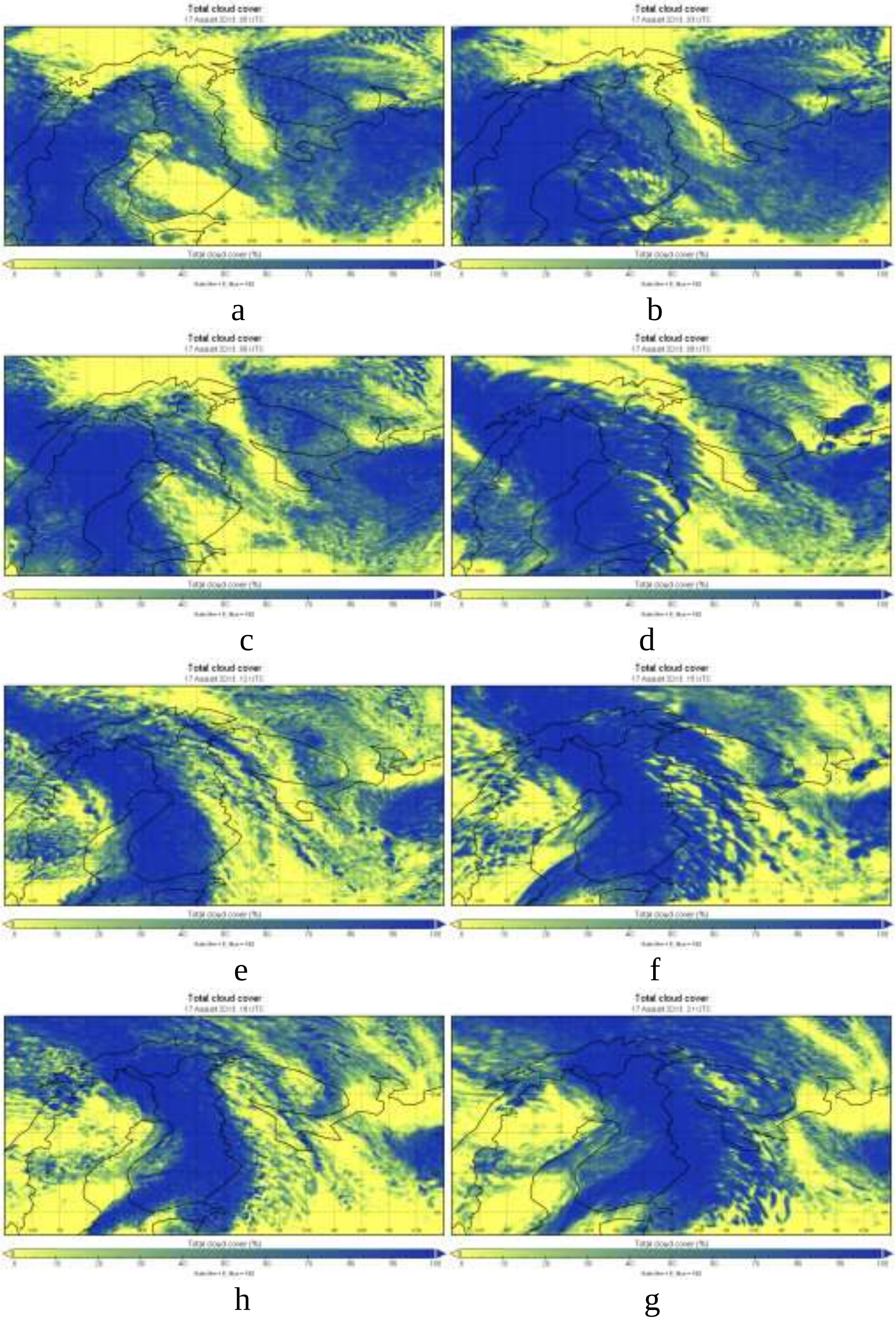

Diurnal cycle of total cloud cover 17.08.2013: (a) 00 UTC, (b) 03 UTC, (c) 06 UTC, (d) 09 UTC, (e) 12 UTC, (f) 15 UTC, (h) 18 UTC, and (g) 21 UTC.

Appendix B2

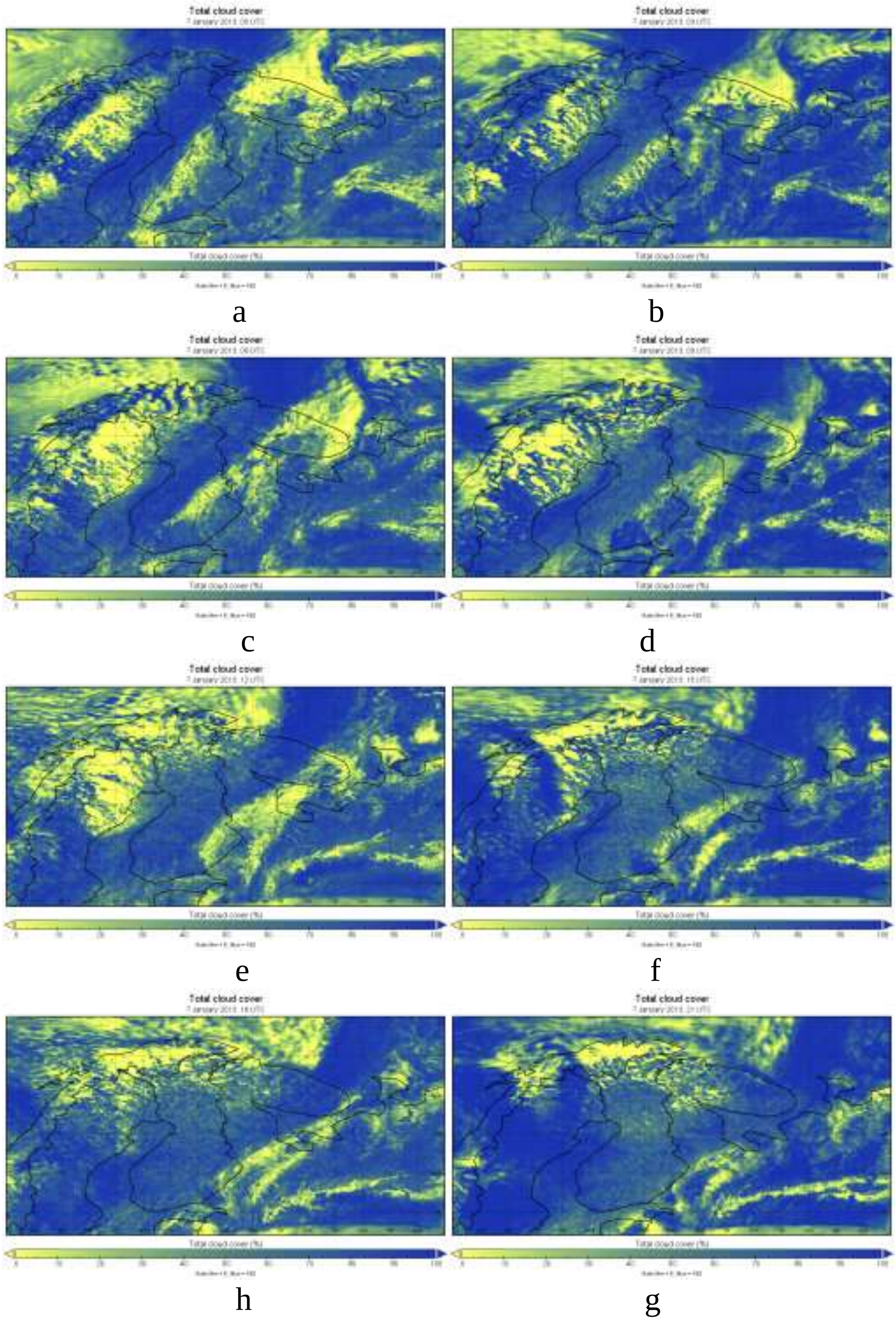

Diurnal cycle of total cloud cover 07.01.2013: (a) 00 UTC, (b) 03 UTC, (c) 06 UTC, (d) 09 UTC, (e) 12 UTC, (f) 15 UTC, (h) 18 UTC, and (g) 21 UTC.

Appendix C1

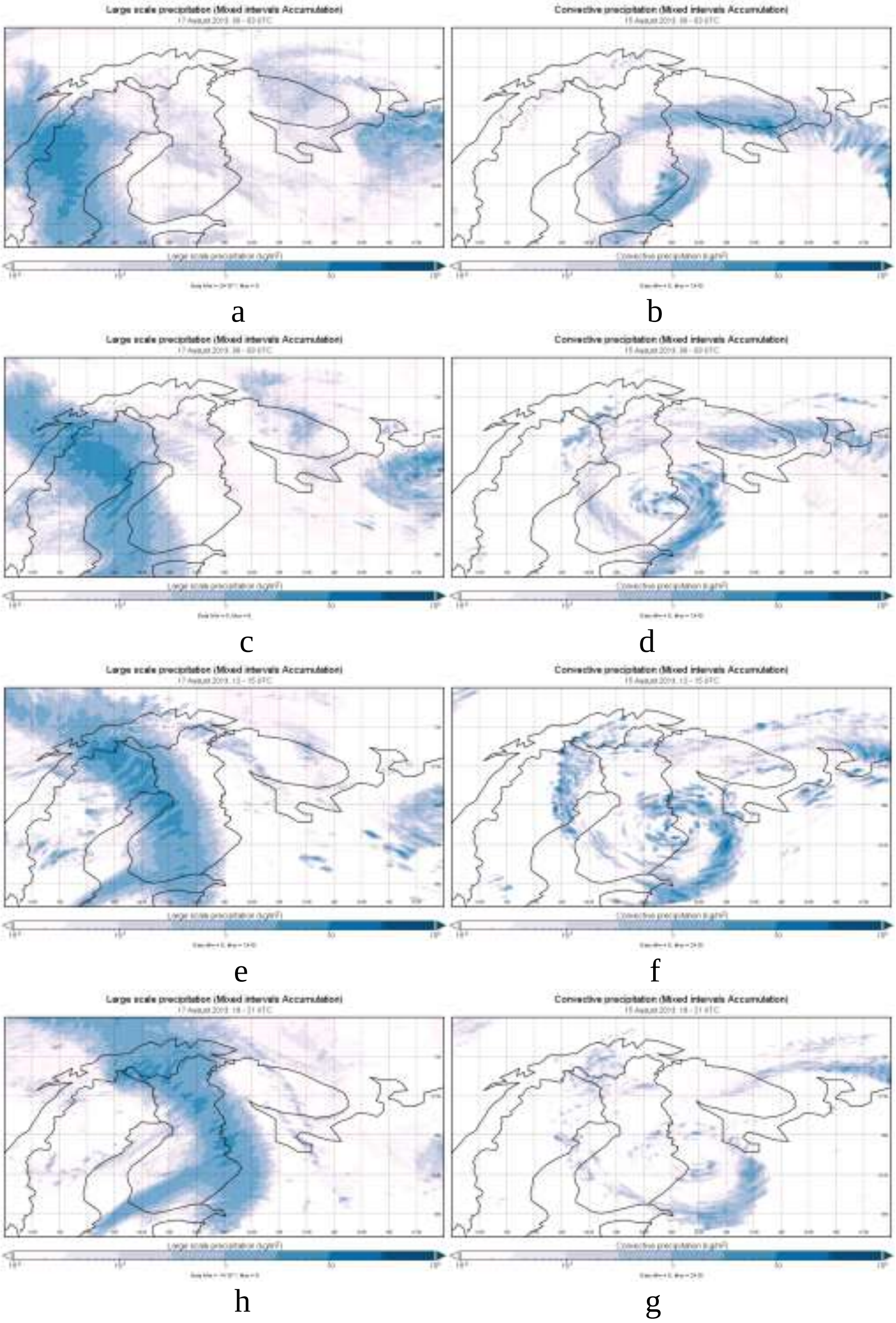

Diurnal cycle of large scale (left column, 17.08.2013) and convective (right column, 15.08.2013) precipitation: (a, b) 00-03 UTC, (c, d) 06-09 UTC, (e, f) 12-15 UTC, (h, g) 18-21 UTC.

Appendix C2

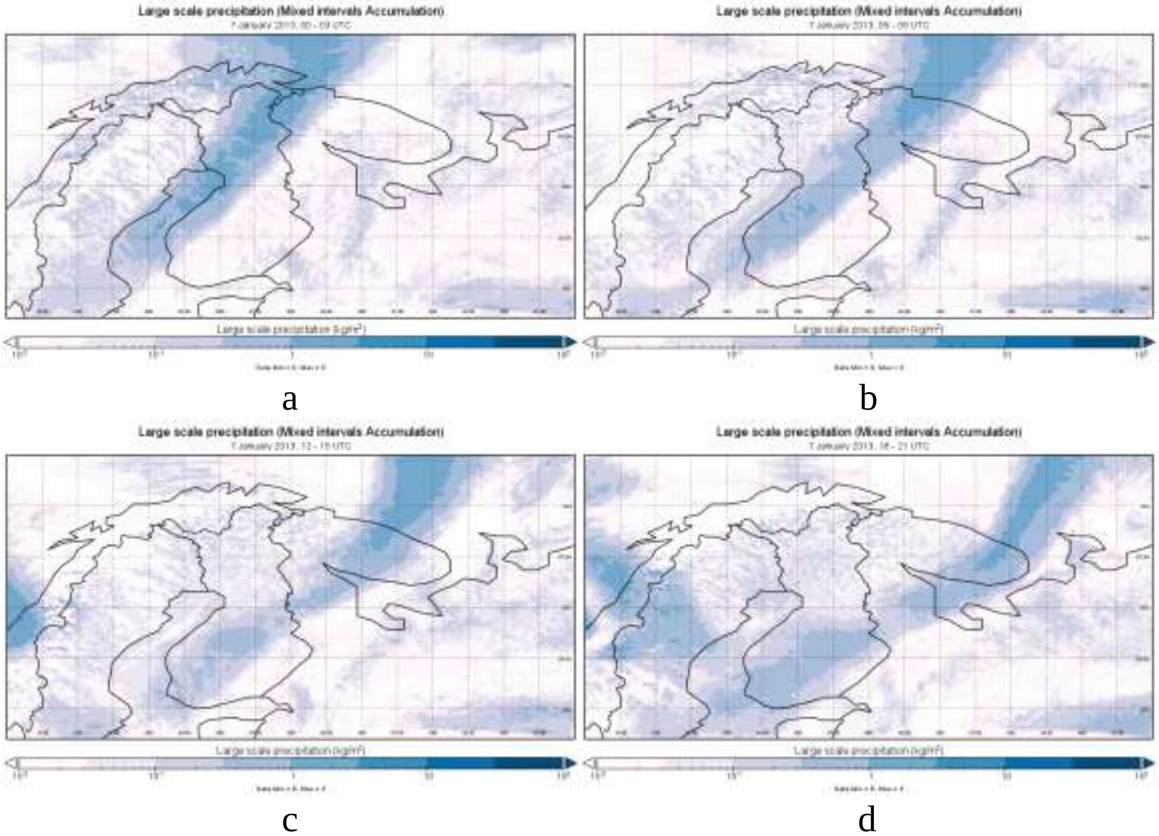

Diurnal cycle of large scale precipitation 07.01.2013: (a) 00-03 UTC, (b) 06-09 UTC, (c) 12-15 UTC, (d) 18-21 UTC.

Appendix D1

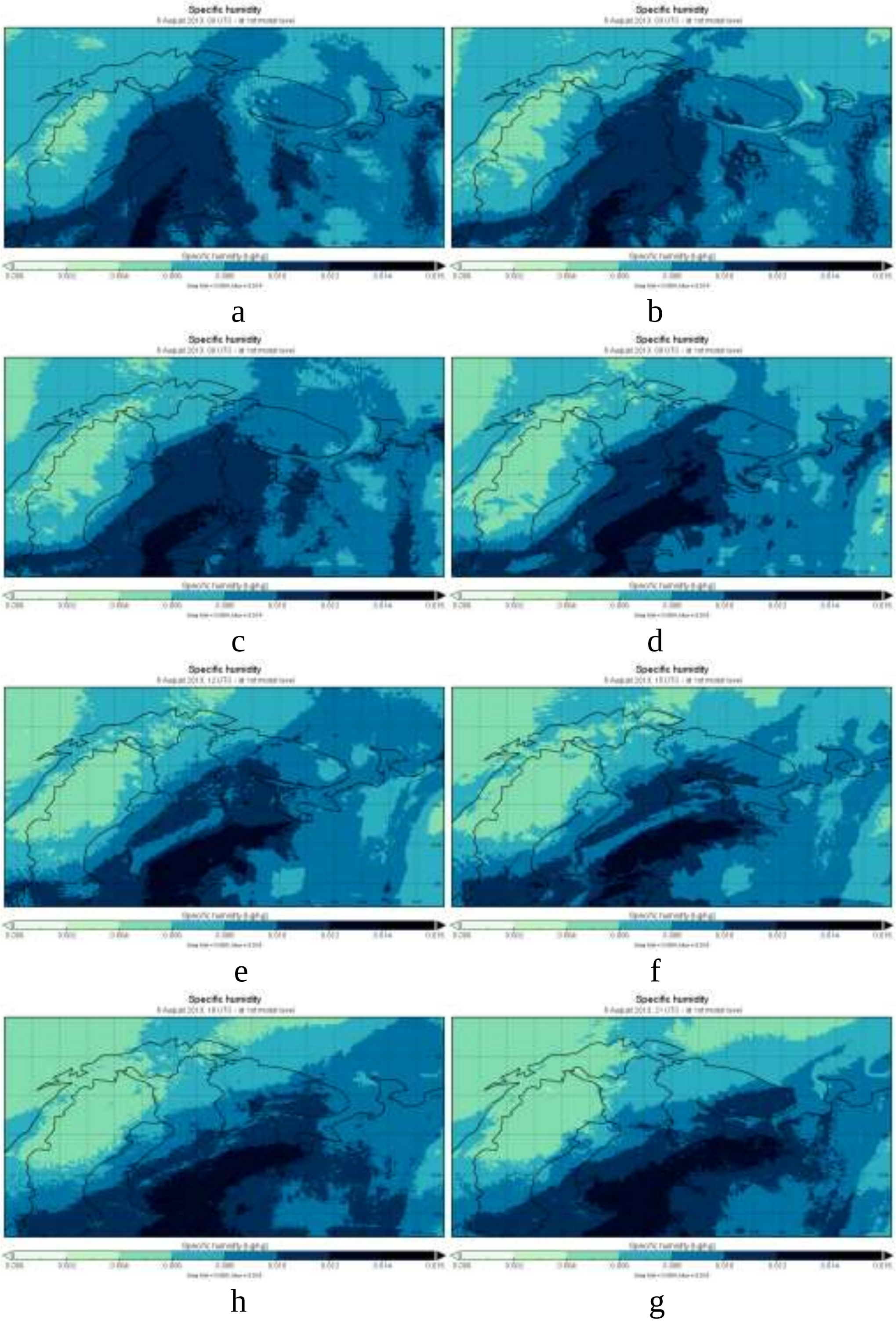

Diurnal cycle of specific humidity 08.08.2013 at 1st model level: (a) 00 UTC, (b) 03 UTC, (c) 06 UTC, (d) 09 UTC, (e) 12 UTC, (f) 15 UTC, (h) 18 UTC, and (g) 21 UTC.

Appendix D2

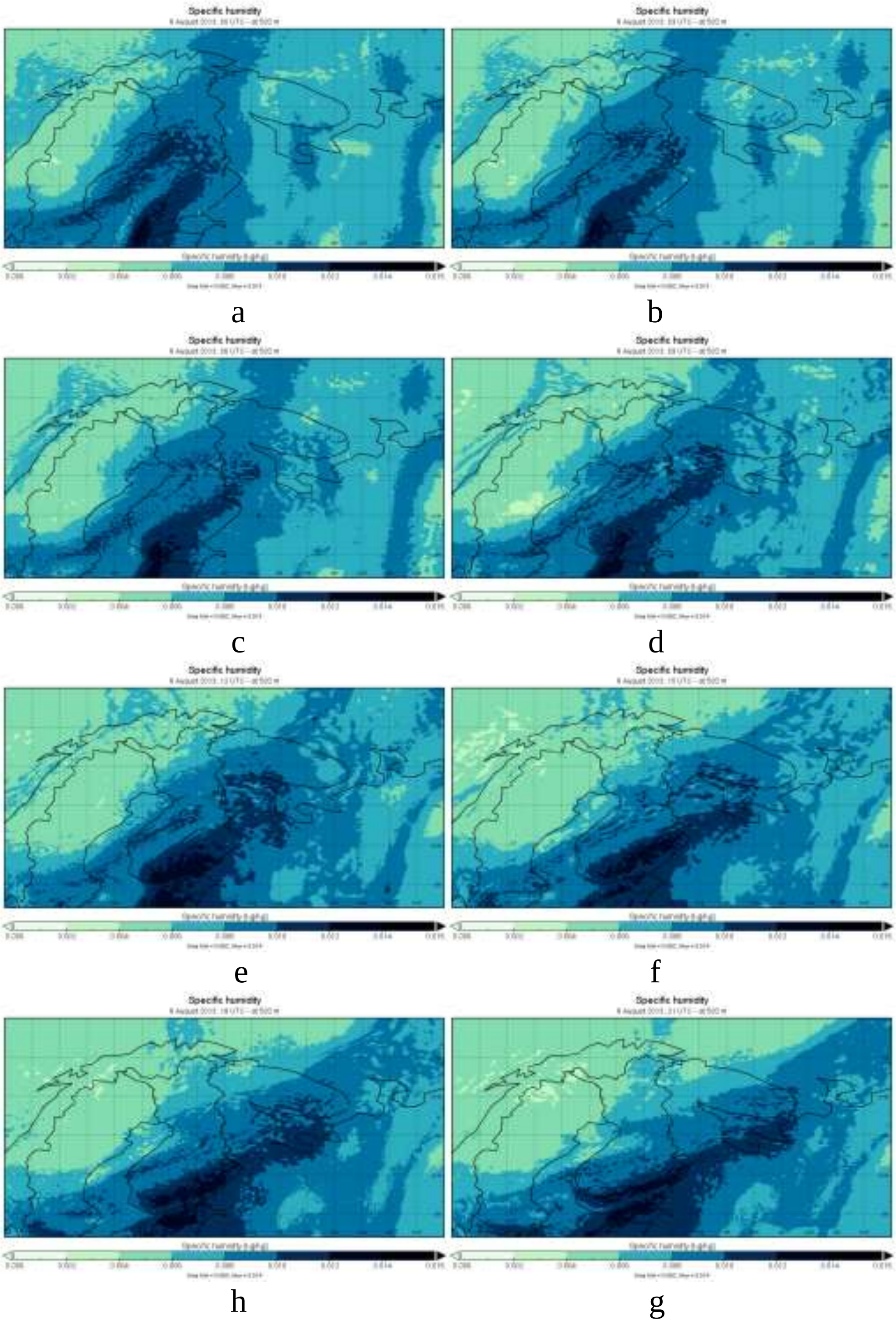

Diurnal cycle of specific humidity 08.08.2013 at 500 m: (a) 00 UTC, (b) 03 UTC, (c) 06 UTC, (d) 09 UTC, (e) 12 UTC, (f) 15 UTC, (h) 18 UTC, and (g) 21 UTC.

Appendix D3

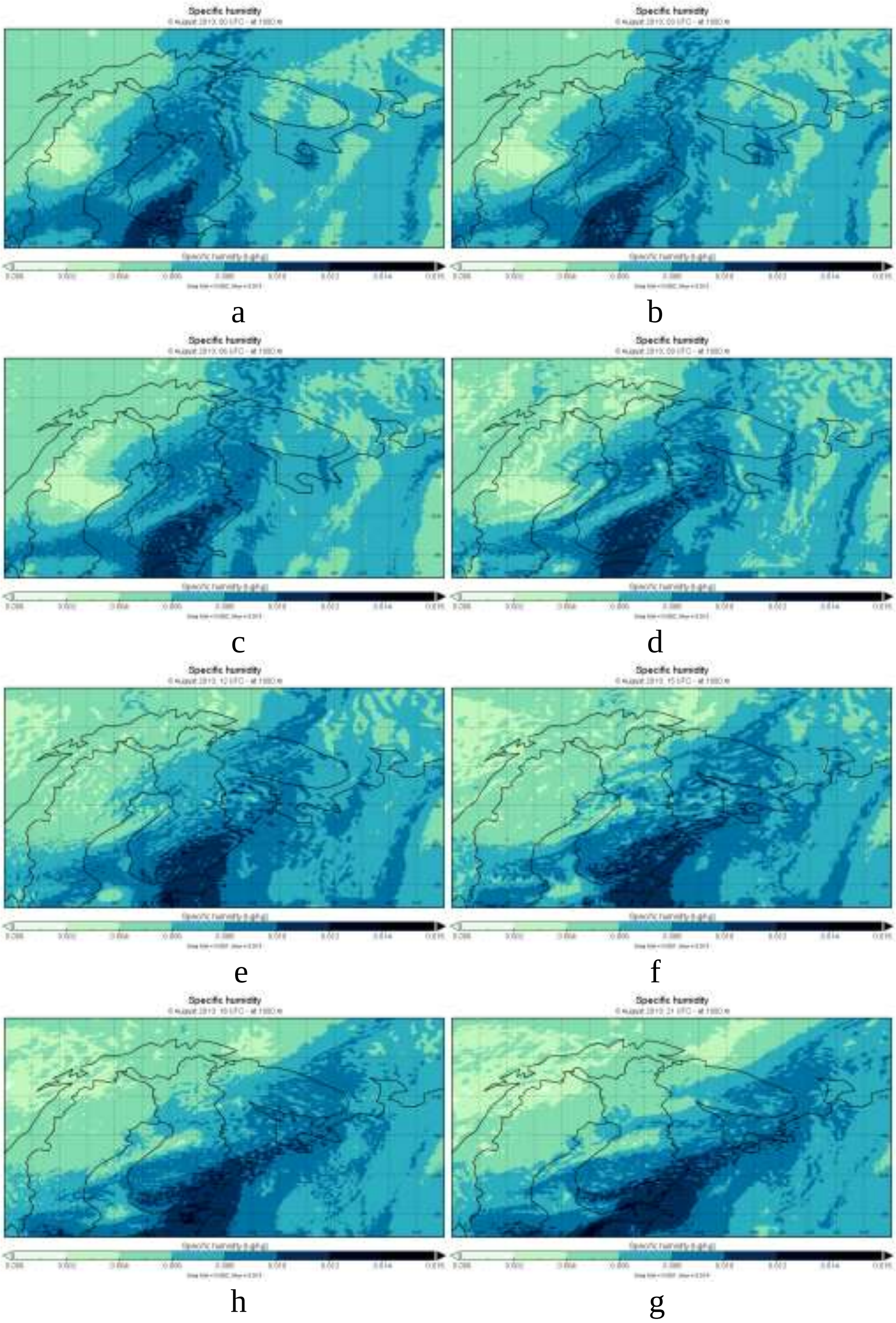

Diurnal cycle of specific humidity 08.08.2013 at 1000 m: (a) 00 UTC, (b) 03 UTC, (c) 06 UTC, (d) 09 UTC, (e) 12 UTC, (f) 15 UTC, (h) 18 UTC, and (g) 21 UTC.

Appendix D4

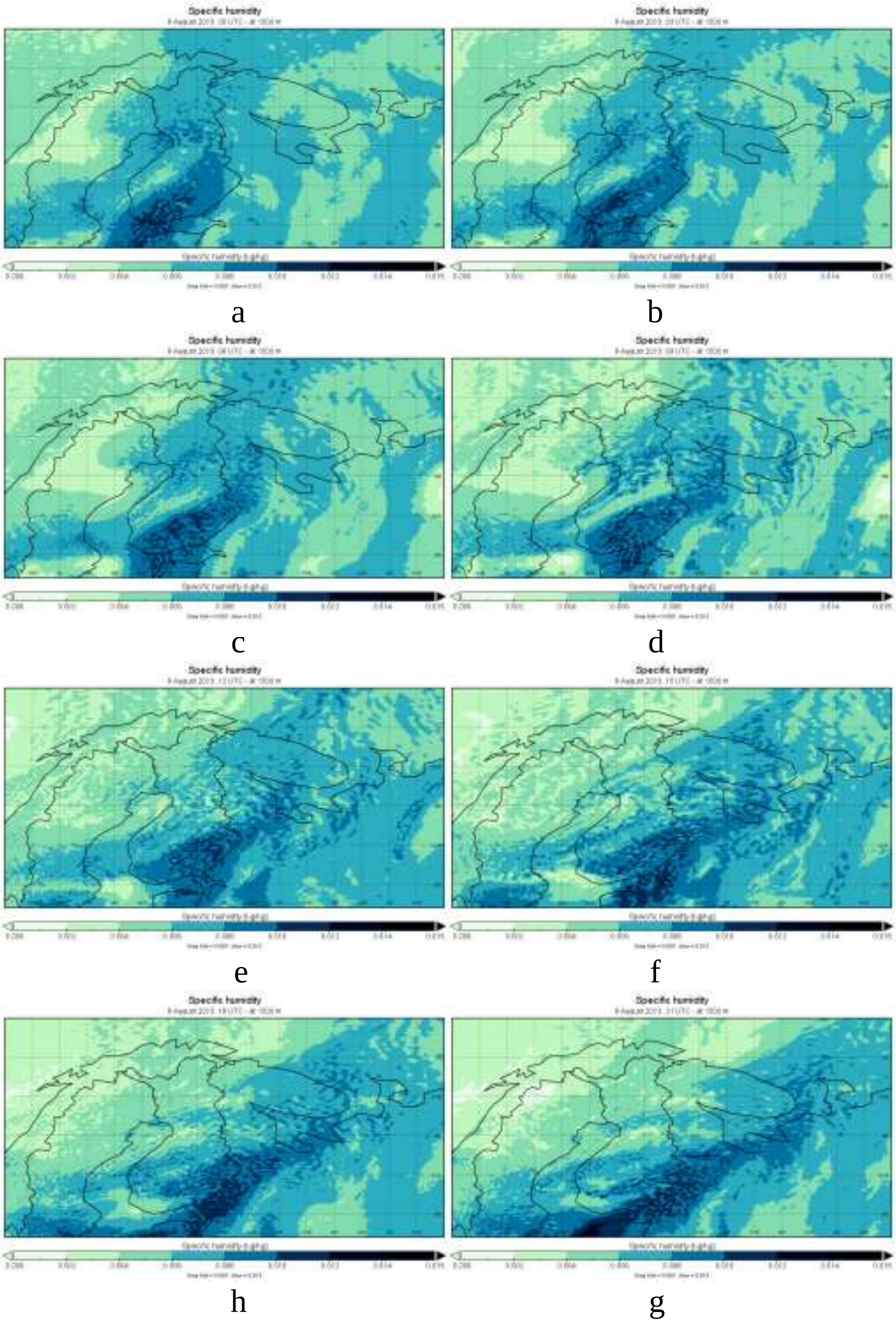

Diurnal cycle of specific humidity 08.08.2013 at 1500 m: (a) 00 UTC, (b) 03 UTC, (c) 06 UTC, (d) 09 UTC, (e) 12 UTC, (f) 15 UTC, (h) 18 UTC, and (g) 21 UTC.

Appendix D5

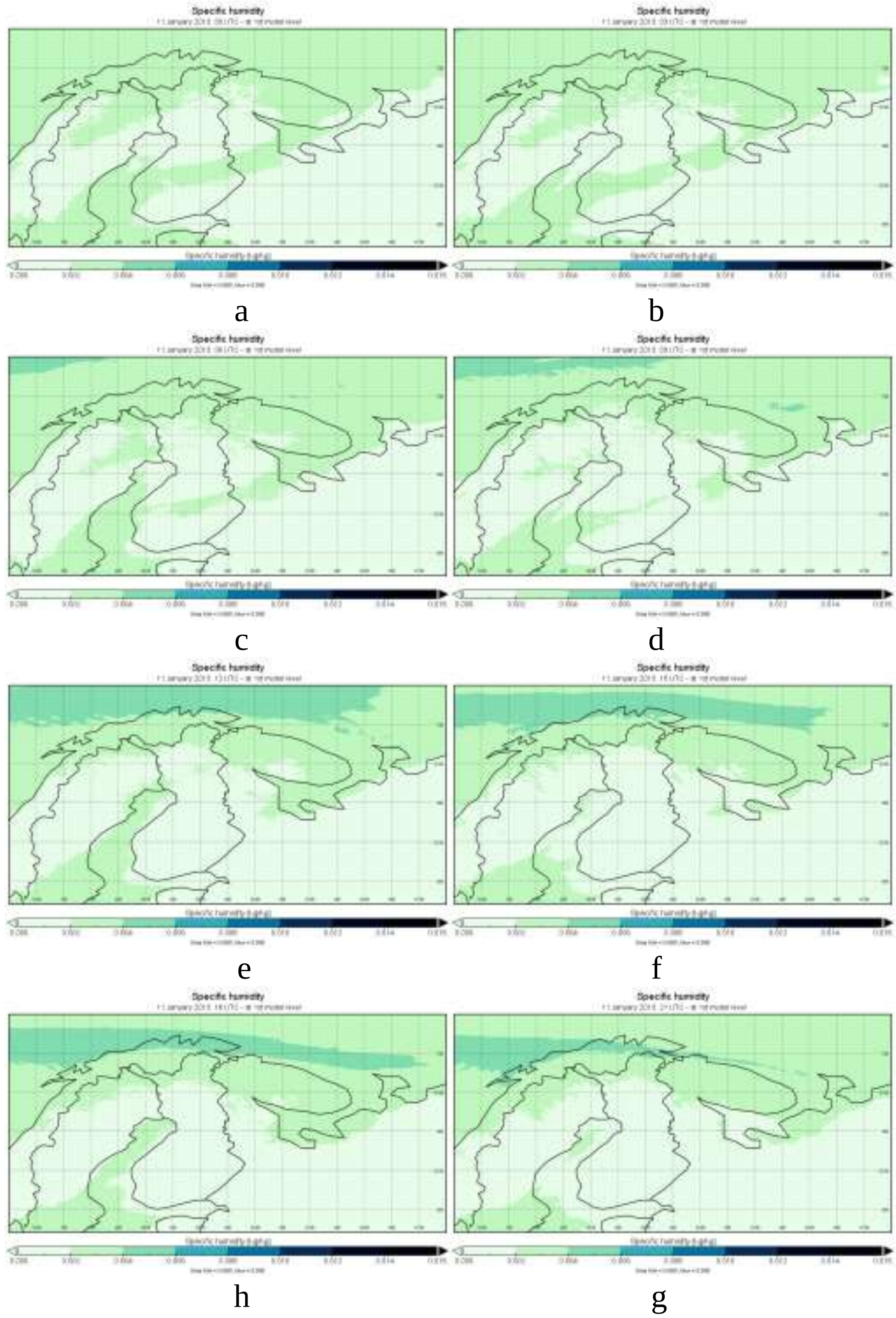

Diurnal cycle of specific humidity 11.01.2013 at 1st model level: (a) 00 UTC, (b) 03 UTC, (c) 06 UTC, (d) 09 UTC, (e) 12 UTC, (f) 15 UTC, (h) 18 UTC, and (g) 21 UTC.

Appendix D6

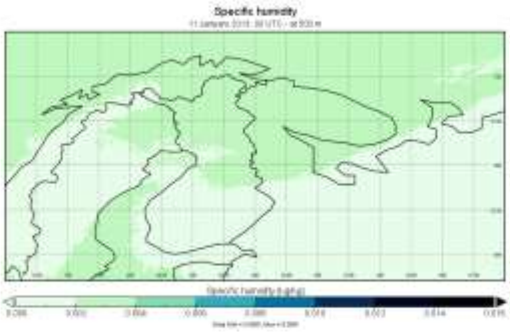

c

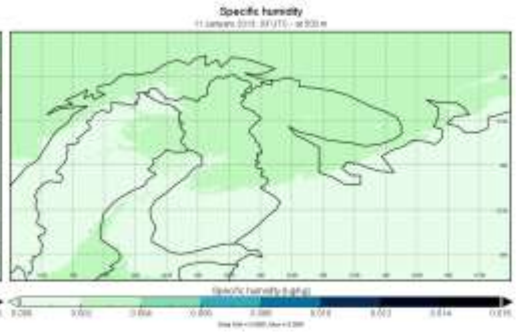

d

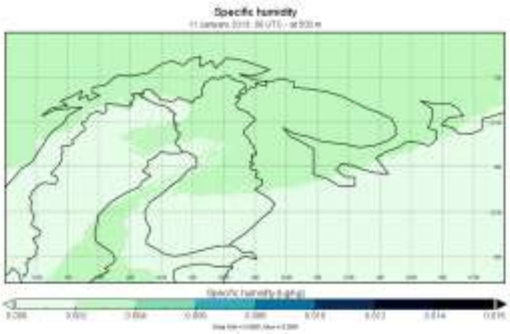

c

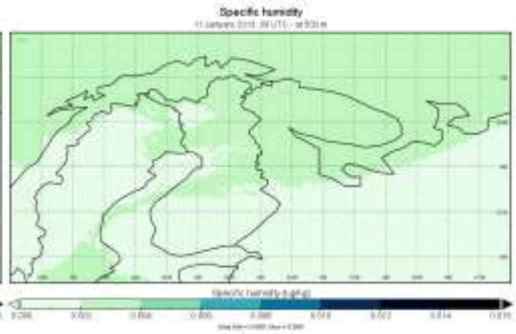

d

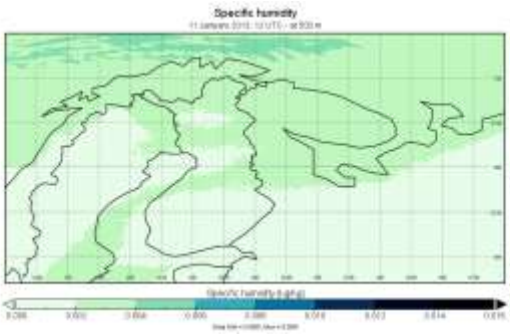

e

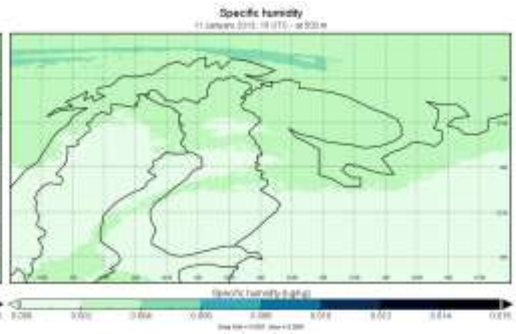

f

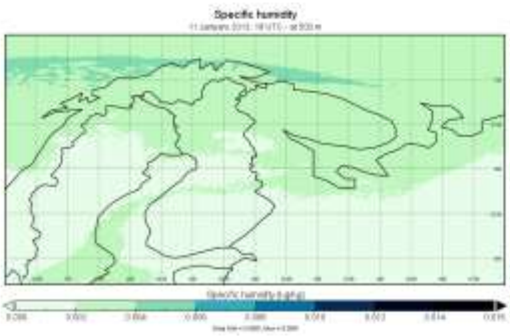

h

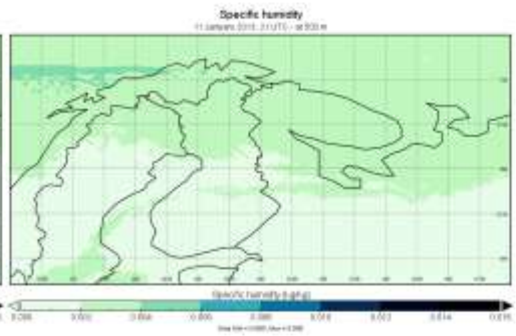

g

Diurnal cycle of specific humidity 11.01.2013 at 500 m: (a) 00 UTC, (b) 03 UTC, (c) 06 UTC, (d) 09 UTC, (e) 12 UTC, (f) 15 UTC, (h) 18 UTC, and (g) 21 UTC.

Appendix D7

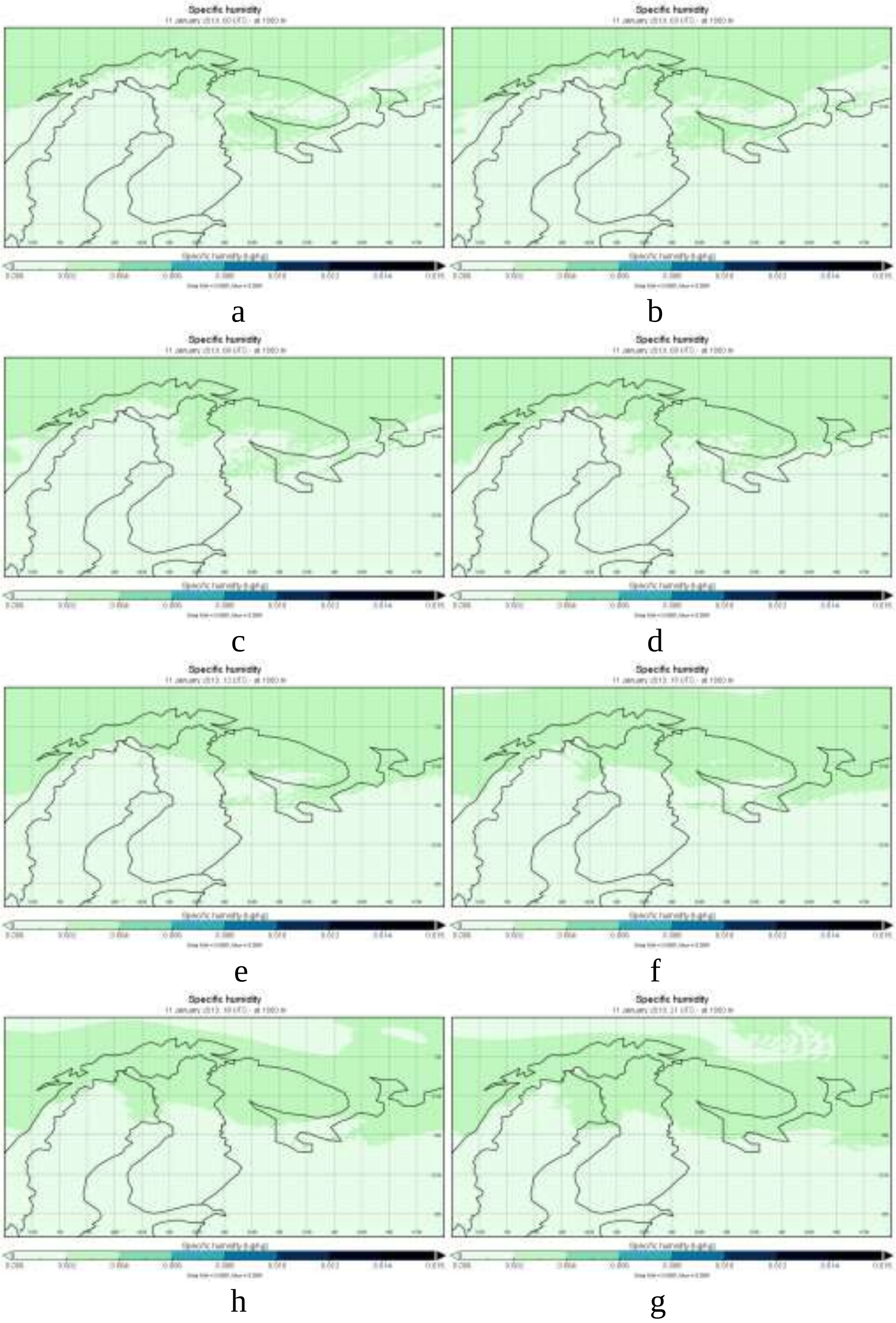

Diurnal cycle of specific humidity 11.01.2013 at 1000 m: (a) 00 UTC, (b) 03 UTC, (c) 06 UTC, (d) 09 UTC, (e) 12 UTC, (f) 15 UTC, (h) 18 UTC, and (g) 21 UTC.

Appendix D8

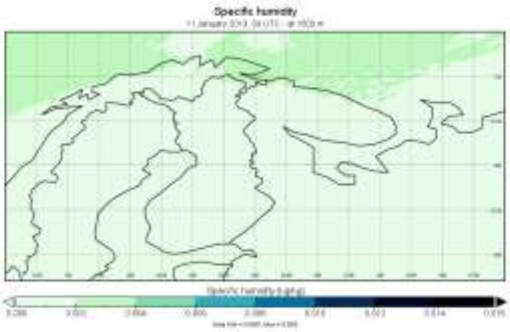

a

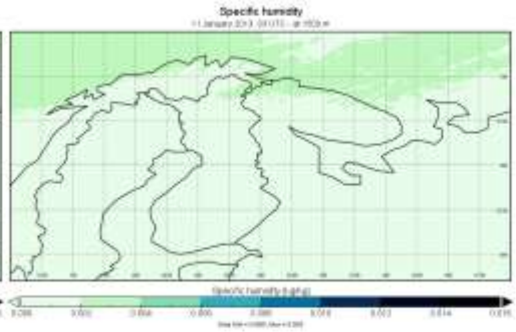

b

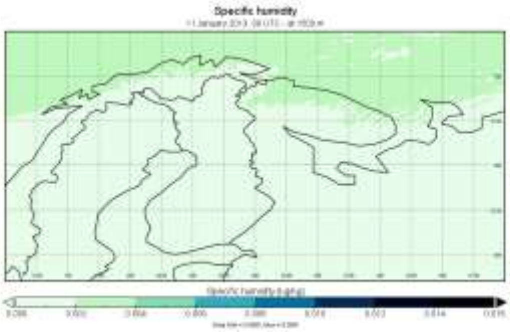

c

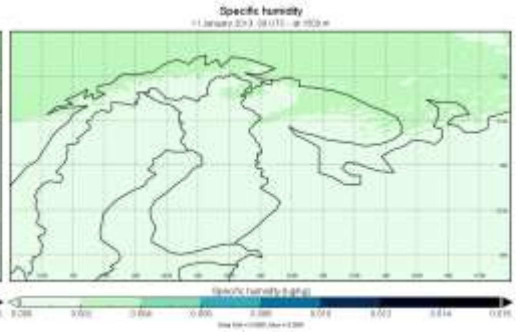

d

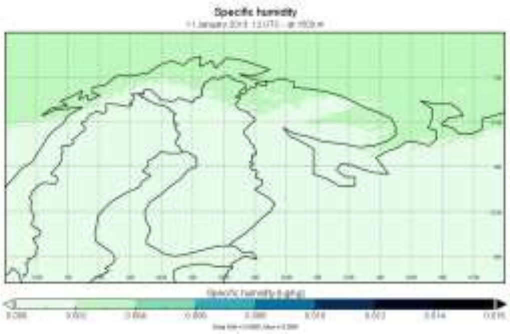

e

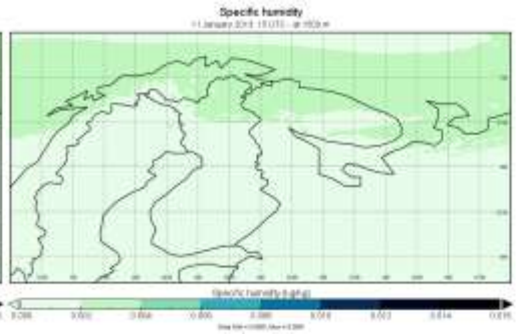

f

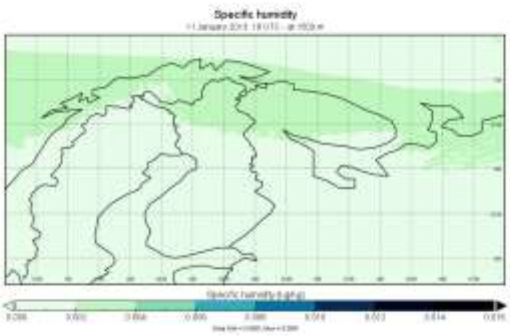

h

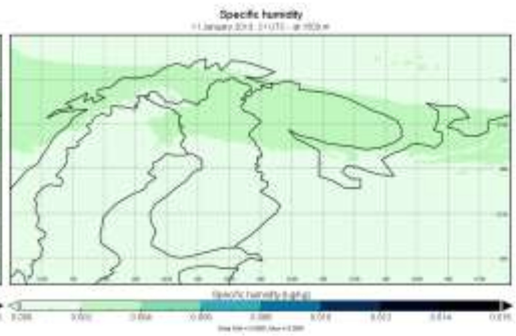

g

Diurnal cycle of specific humidity 11.01.2013 at 1500 m: (a) 00 UTC, (b) 03 UTC, (c) 06 UTC, (d) 09 UTC, (e) 12 UTC, (f) 15 UTC, (h) 18 UTC, and (g) 21 UTC.

Appendix E1

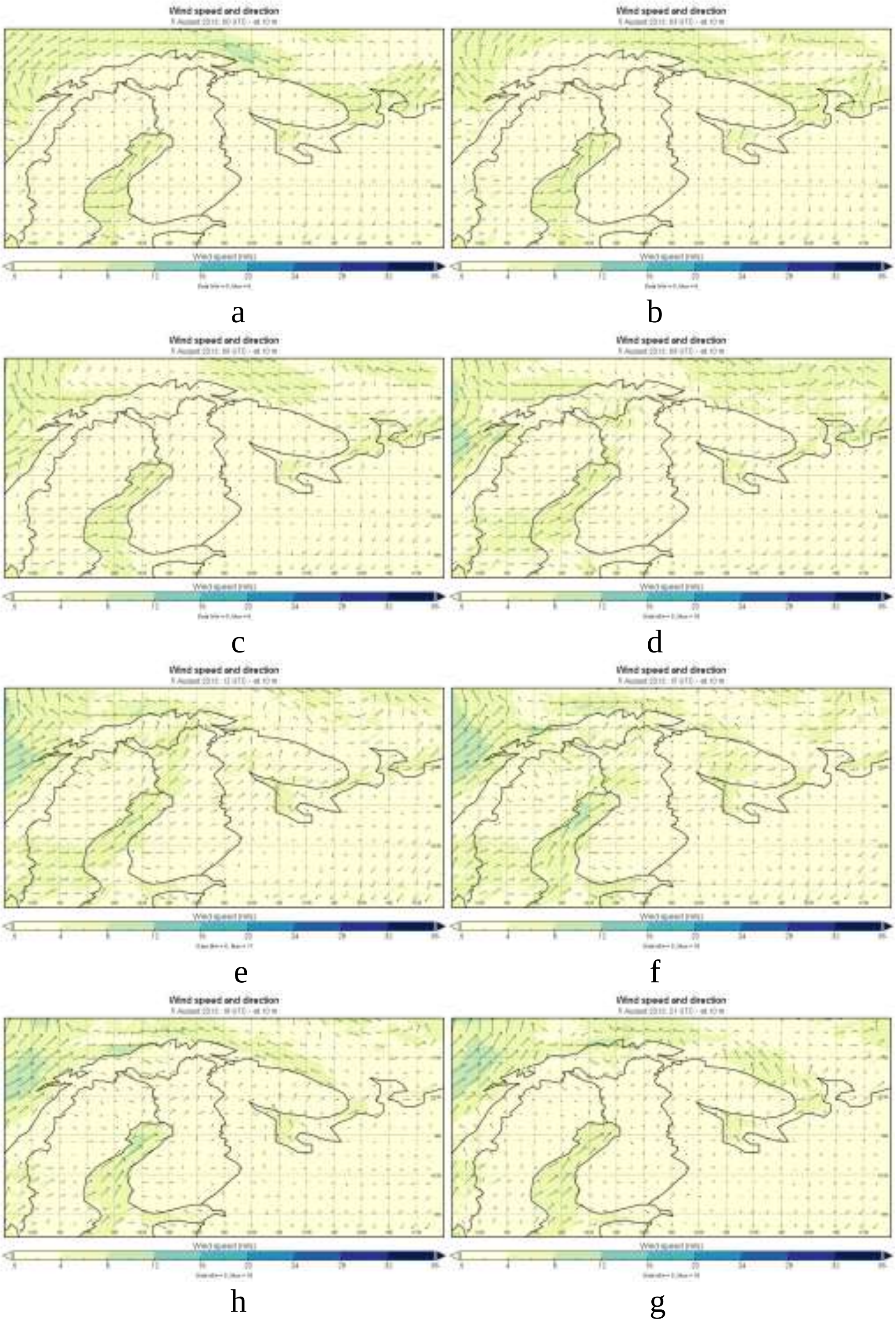

Diurnal cycle of wind speed and direction fields 05.08.2013 at 10m: (a) 00 UTC, (b) 03 UTC, (c) 06 UTC, (d) 09 UTC, (e) 12 UTC, (f) 15 UTC, (h) 18 UTC, and (g) 21 UTC.

Appendix E2

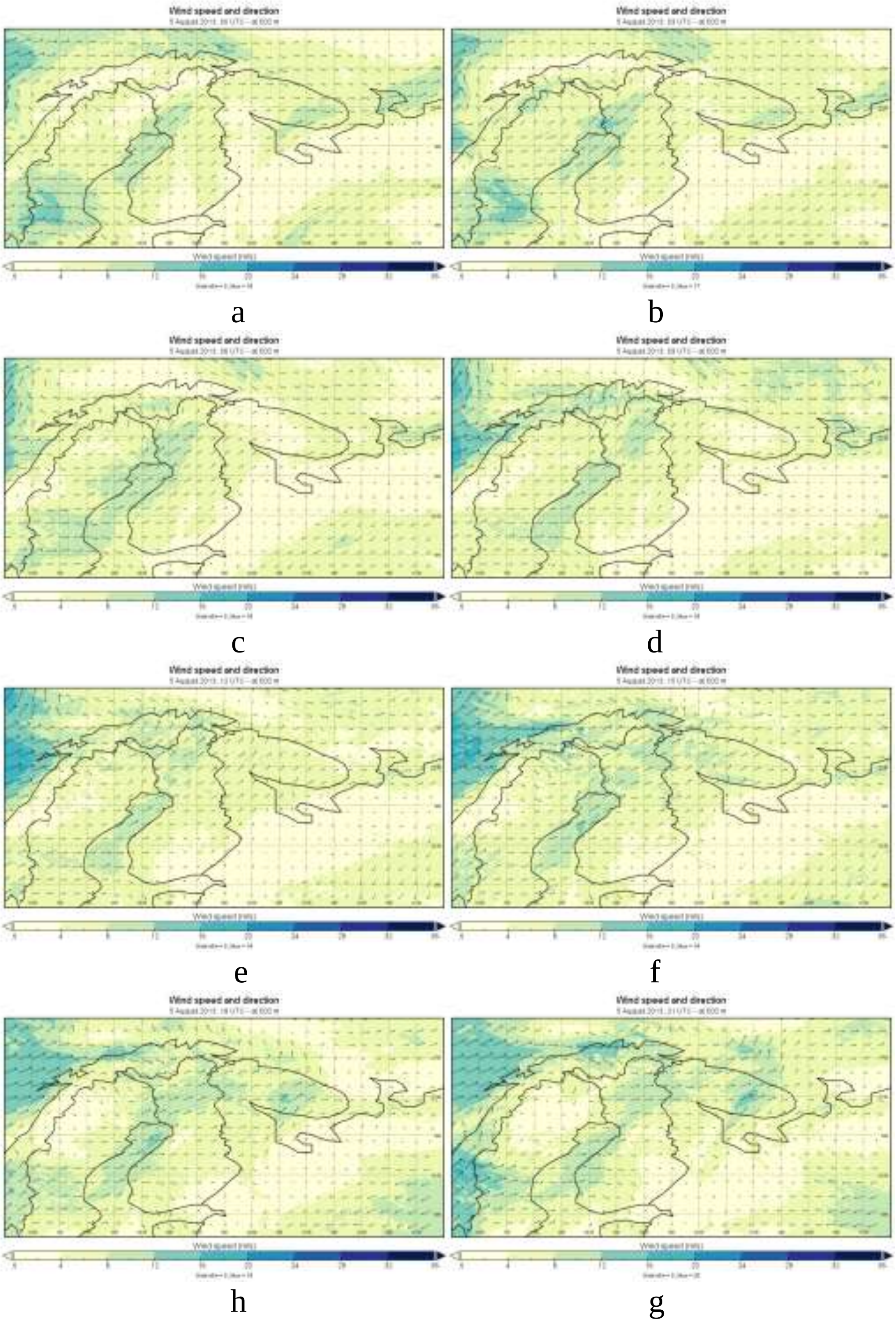

Diurnal cycle of wind speed and direction fields 05.08.2013 at 500 m: (a) 00 UTC, (b) 03 UTC, (c) 06 UTC, (d) 09 UTC, (e) 12 UTC, (f) 15 UTC, (h) 18 UTC, and (g) 21 UTC.

Appendix E3

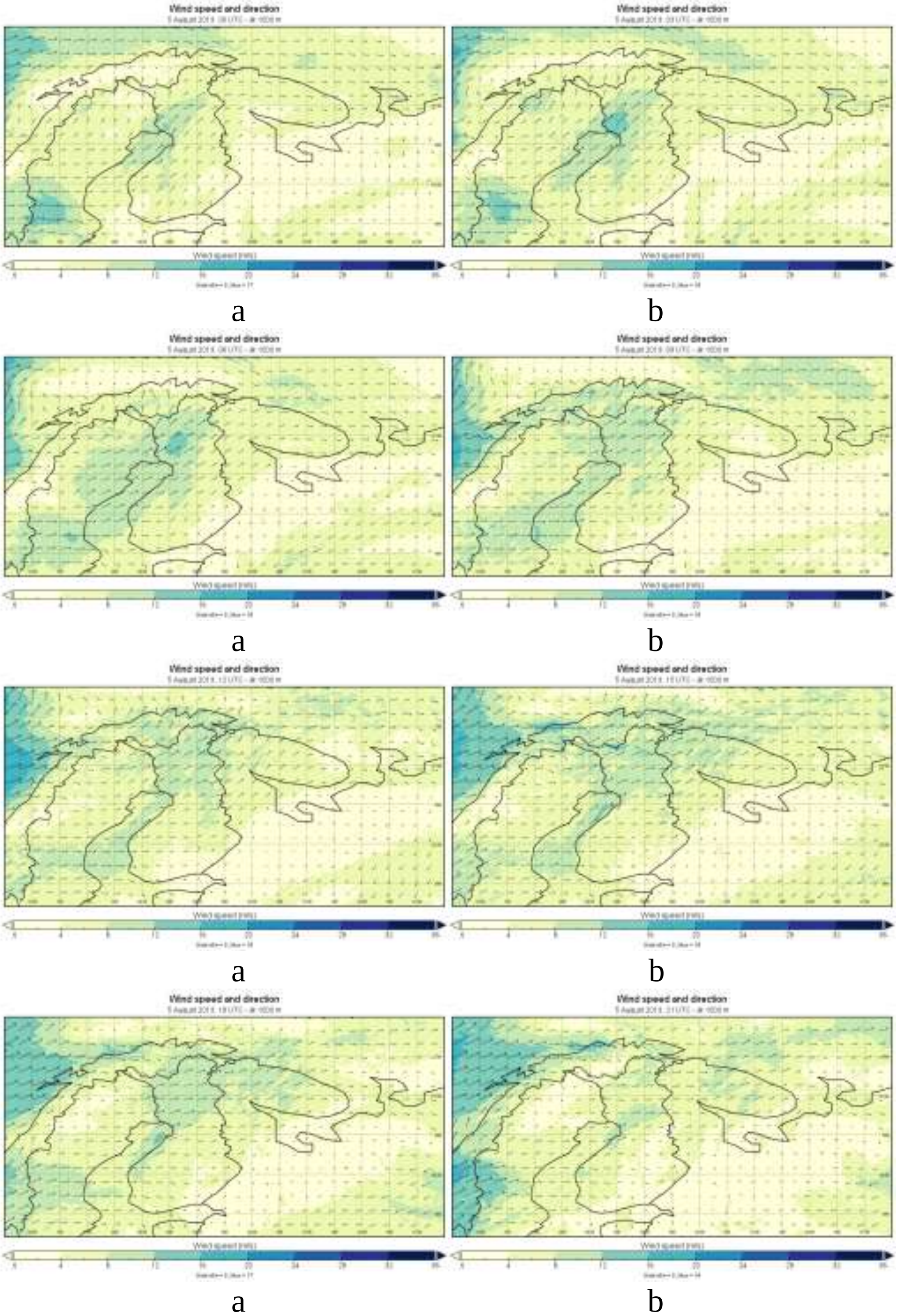

Diurnal cycle of wind speed and direction fields 05.08.2013 at 1000 m: (a) 00 UTC, (b) 03 UTC, (c) 06 UTC, (d) 09 UTC, (e) 12 UTC, (f) 15 UTC, (h) 18 UTC, and (g) 21 UTC.

Appendix E4

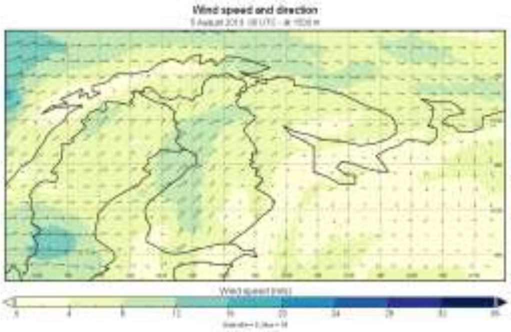

a

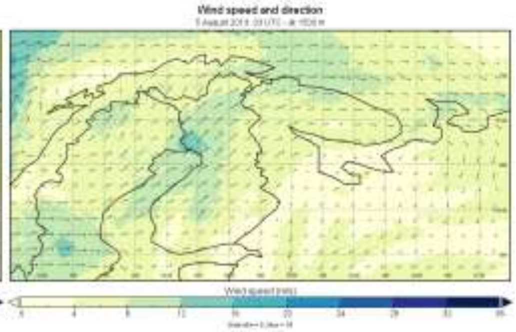

b

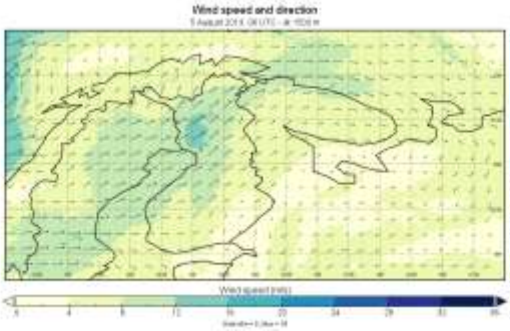

c

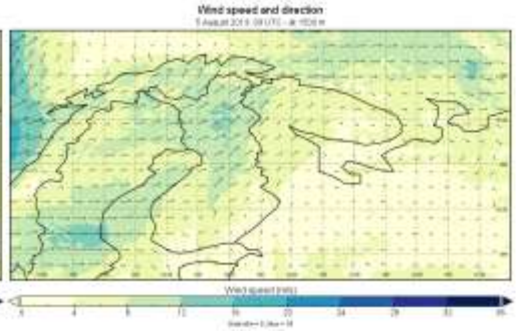

d

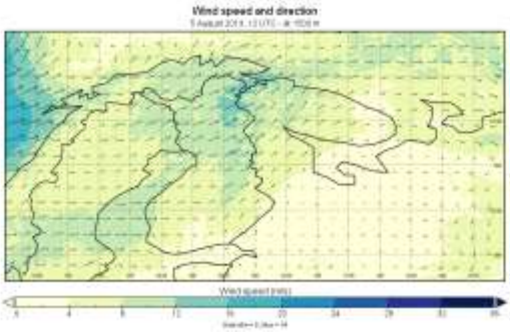

e

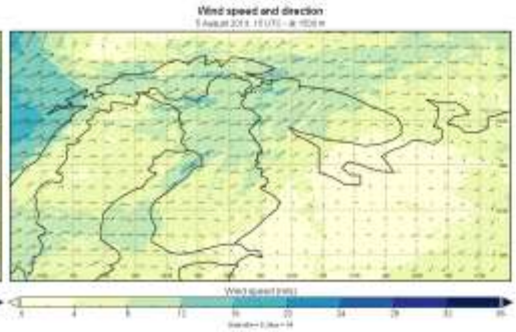

f

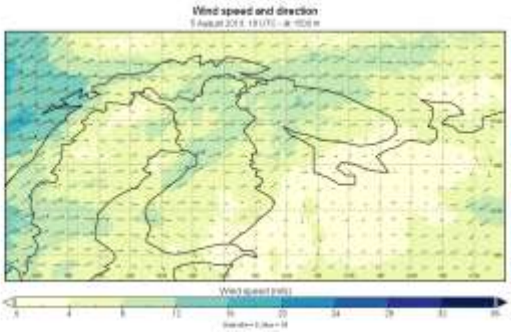

h

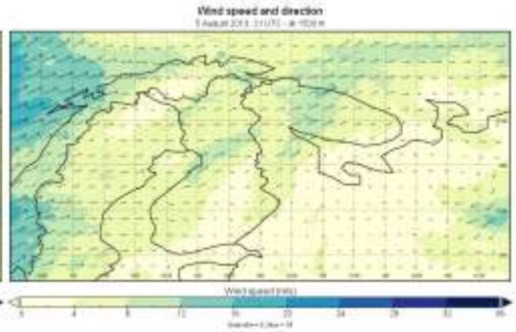

g

Diurnal cycle of wind speed and direction fields 05.08.2013 at 1500 m: (a) 00 UTC, (b) 03 UTC, (c) 06 UTC, (d) 09 UTC, (e) 12 UTC, (f) 15 UTC, (h) 18 UTC, and (g) 21 UTC.

Appendix E5

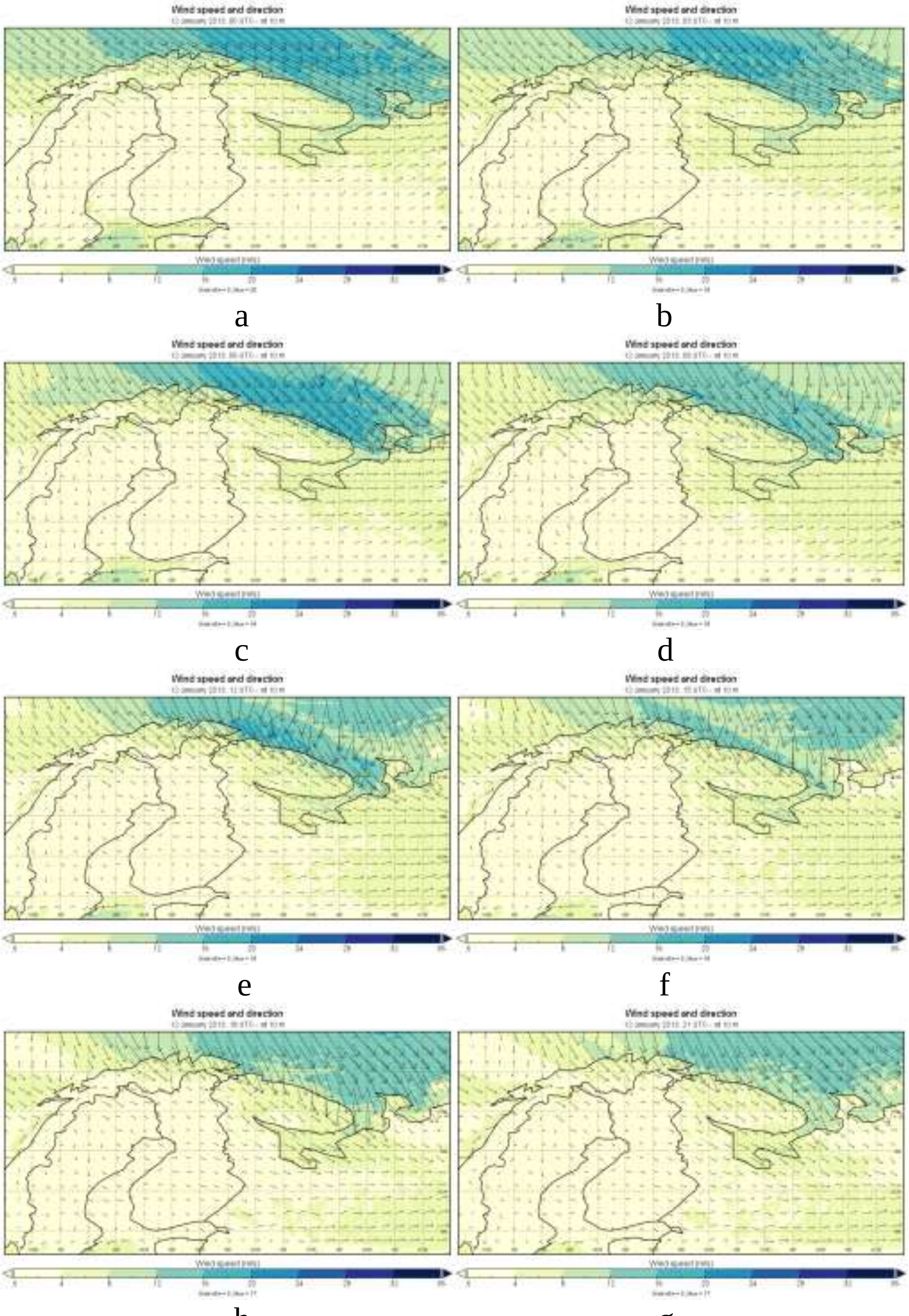

Diurnal cycle of wind speed and direction fields 12.01.2013 at 10 m: (a) 00 UTC, (b) 03 UTC, (c) 06 UTC, (d) 09 UTC, (e) 12 UTC, (f) 15 UTC, (h) 18 UTC, and (g) 21 UTC.

Appendix E6

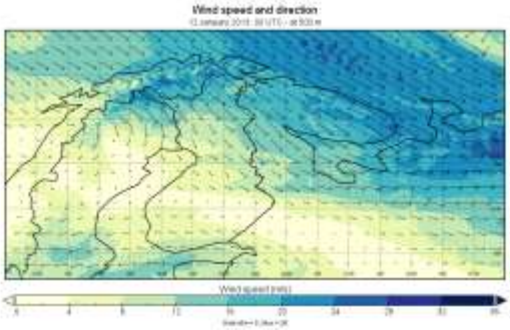

a

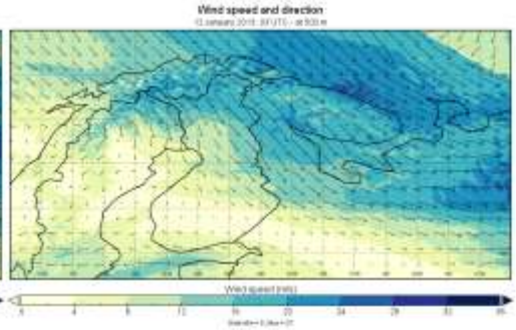

b

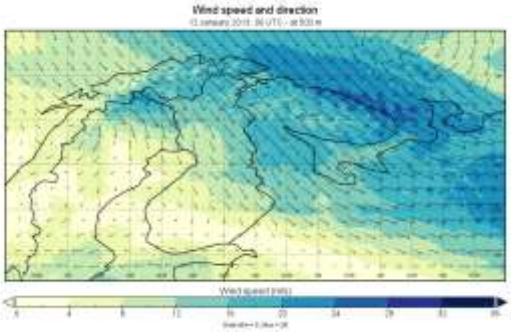

c

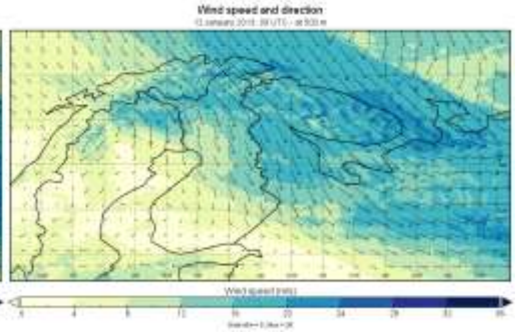

d

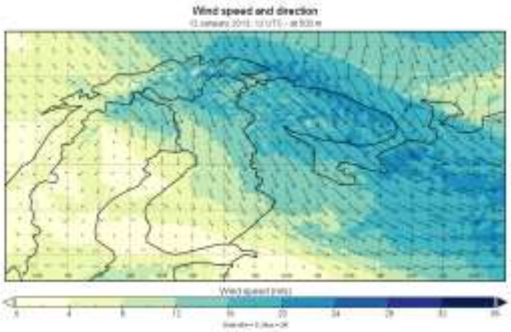

e

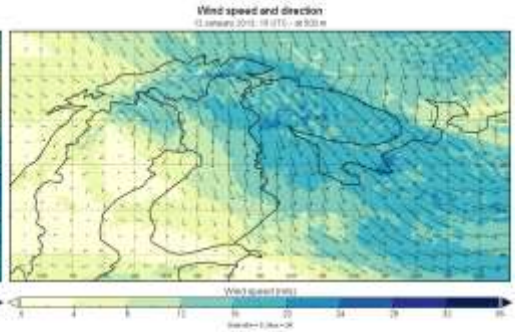

f

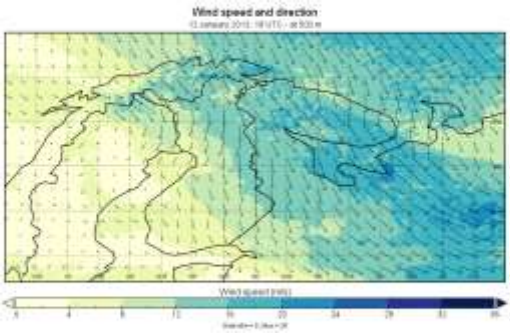

h

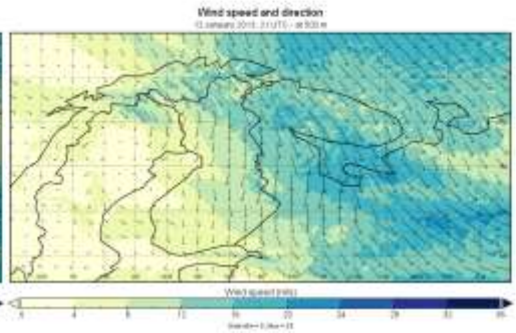

g

Diurnal cycle of wind speed and direction fields 12.01.2013 at 500 m: (a) 00 UTC, (b) 03 UTC, (c) 06 UTC, (d) 09 UTC, (e) 12 UTC, (f) 15 UTC, (h) 18 UTC, and (g) 21 UTC.

Appendix E7

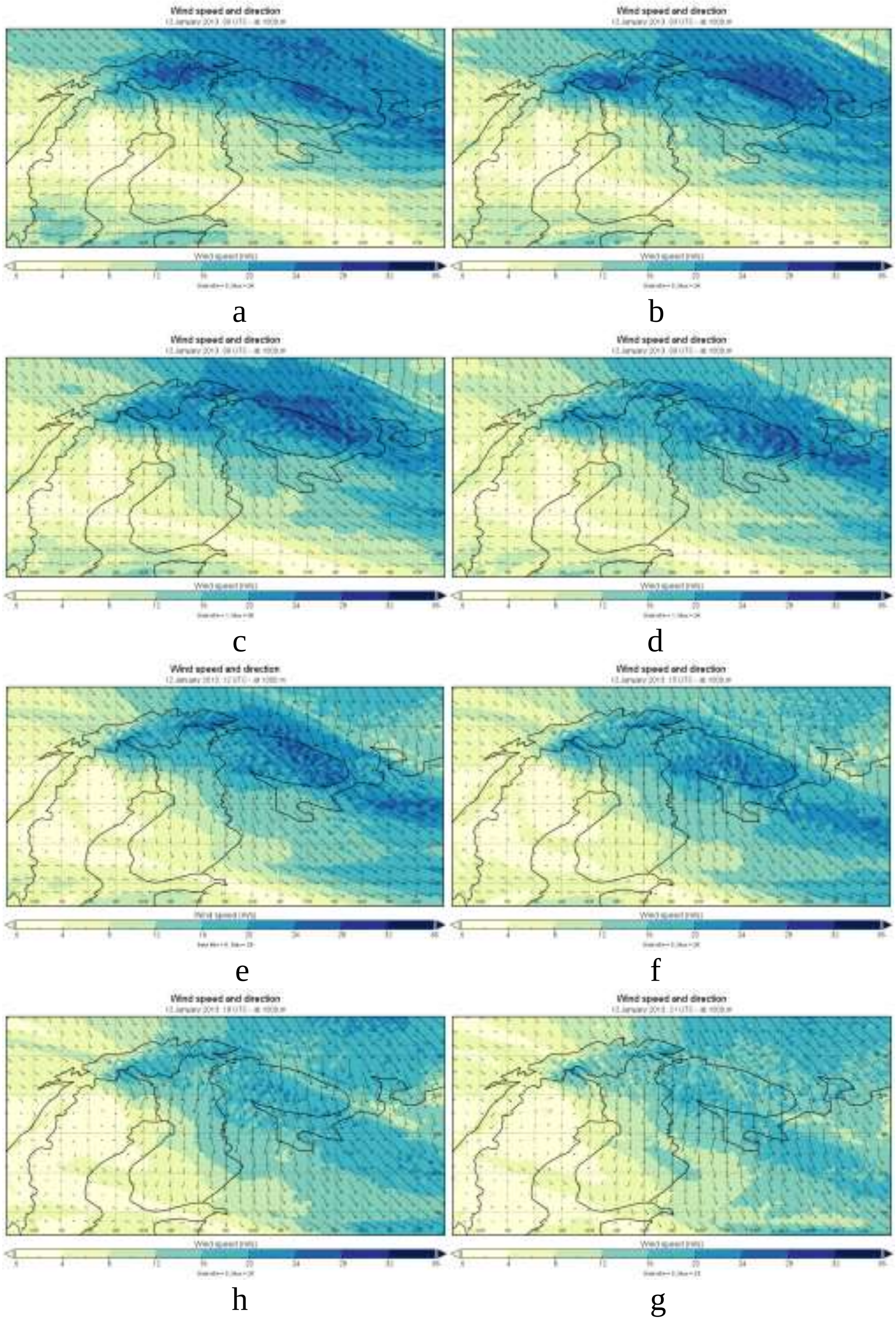

Diurnal cycle of wind speed and direction fields 12.01.2013 at 1000 m: (a) 00 UTC, (b) 03 UTC, (c) 06 UTC, (d) 09 UTC, (e) 12 UTC, (f) 15 UTC, (h) 18 UTC, and (g) 21 UTC.

Appendix E8

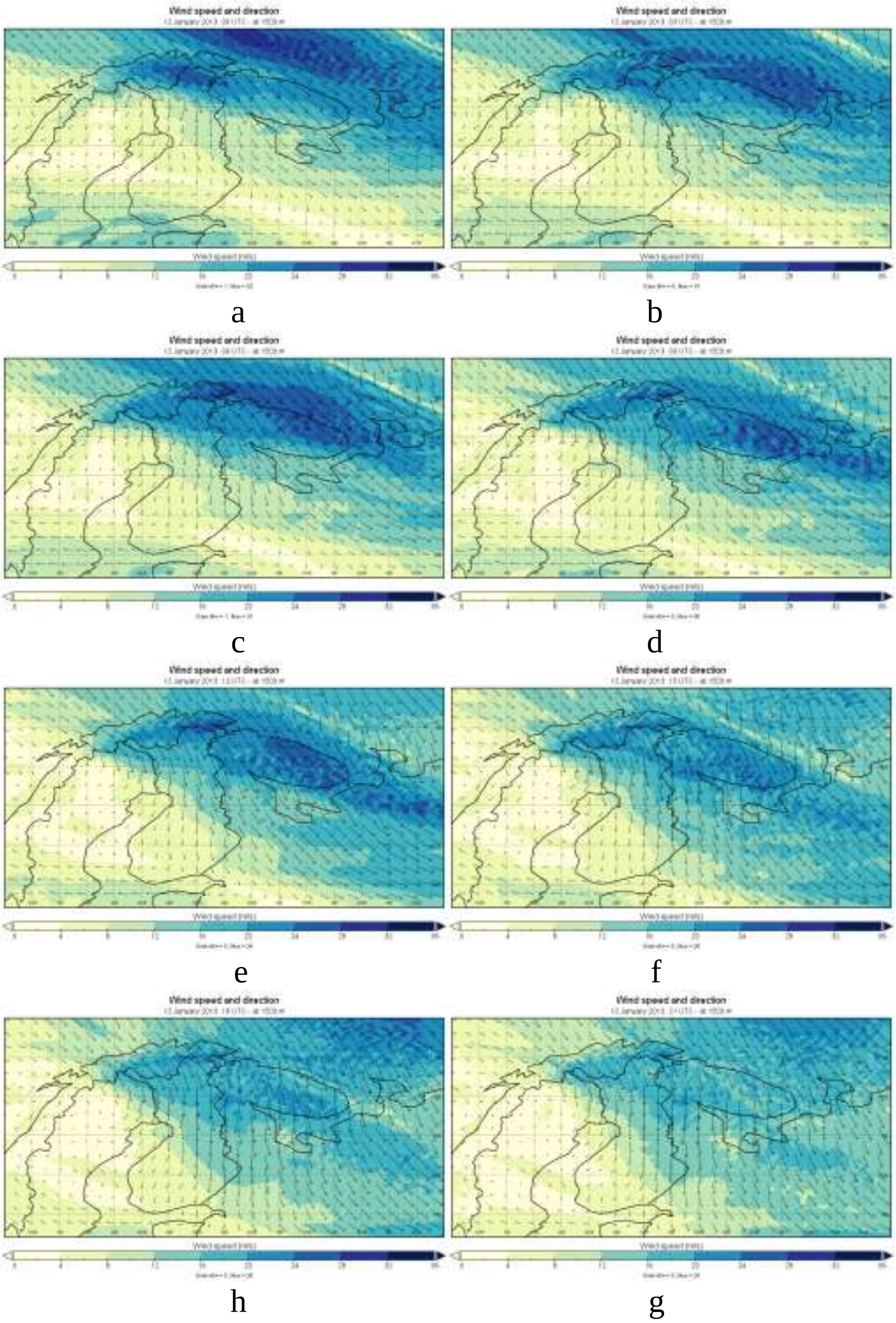

Diurnal cycle of wind speed and direction fields 12.01.2013 at 1500 m: (a) 00 UTC, (b) 03 UTC, (c) 06 UTC, (d) 09 UTC, (e) 12 UTC, (f) 15 UTC, (h) 18 UTC, and (g) 21 UTC.